

Politecnico di Torino



Corso di Laurea Magistrale in Ingegneria Energetica e Nucleare

**Texture analysis in metastases of patients affected by
metastatic differentiated thyroid carcinoma treated
with ^{131}I**

Supervisor:

Ing. Andrea Lavagno

Author:

Alessandra Pecora

Co-Supervisor:

Dott. Michele Stasi

Torino, 26 marzo 2019

A Mamma e Papà

Contents

<i>Introduction</i>	1
1. <i>State of the art</i>	3
1.1 The importance of lesion dosimetry	3
1.2 Texture Analysis	4
2. <i>Nuclear Medicine in metastatic thyroid carcinoma treatment</i>	7
2.1 Iodine and its radioactive isotopes	7
2.2 Radiometabolic therapy with ^{131}I	9
2.3 Diagnosis with SPECT-CT	10
3. <i>Lesion dosimetry</i>	18
3.1 MIRDO method	18
3.2 SPECT-CT Calibration	24
3.3 Dosimetric protocol on the patient	27
4. <i>Radiomics in SPECT-CT imaging of Iodine captants lesions</i>	29
4.1 Texture Analysis methodology: features used	32
4.2 LifeX software	37
5. <i>Validation of the method through phantom analysis</i>	42
5.1 Discretization analysis of the features	42
5.2 Features analysis	45
6. <i>Patients analysis</i>	53
6.1 Dataset	53
6.2 Features extraction	56
6.2.1 Shape feature analysis	56

6.3	Statistical Analysis	59
6.3.1	Wilcoxon-Mann-Whitney test and Box-and-whisker Plot	60
6.3.2	ROC curve analysis	61
7.	<i>Results</i>	64
7.1	Statistical analysis results: first approach	64
7.2	Statistical analysis results: second approach	69
7.3	Statistical analysis results: mean absorbed Dose	71
8.	<i>Conclusions</i>	74
A.	<i>Matlab script</i>	77
B.	<i>Wilcoxon-Mann-Whitney test: probability values</i>	79
B.1	p-values: first approach	79
B.2	p-values: second approach	80
C.	<i>Abstract presented at XIV Congresso Nazionale Associazione Italiana di Medicina Nucleare (AIMN) 2019</i>	81
D.	<i>ROC curve analysis</i>	83
D.1	ROC curve analysis: first approach	83
D.2	ROC curve analysis: second approach	83
E.	<i>Box and whisker plots</i>	102
E.1	Box plot: first approach	102
E.2	Box plot: second approach	102
	<i>Acknowledgements</i>	128

List of Figures

1.1	Simplified illustration of dosimetry approaches to determine the administered radionuclide activity	5
2.1	^{131}I production process	8
2.2	Nuclear decay scheme for I-131	8
2.3	All possible collimators which can be required and mounted on for any acquisition	11
2.4	Schematic of a gamma camera for detecting single photons	12
2.5	Inorganic scintillators mechanism	13
2.6	Photomultiplier tube scheme	13
2.7	HEAP collimators mounted up with detectors on gamma camera head . .	14
2.8	Gamma camera connection to gantry system	15
2.9	Circular SPECT acquisitions scheme	15
2.10	Energetic resolution in gamma spectrometry	16
3.1	MIRD Phamphlet No. 16	19
3.2	Thyroid as source and target organ	20
3.3	cumulated activity	20
3.4	Absorbed fraction	22
3.5	S factor values	23
3.6	NEMA PET-CT phantom	24
3.7	Dead time indices	25
3.8	SPECT reconstruction procedure	26
3.9	SPECT acquisition of the spheres	26
3.10	SPECT/CT system	28
4.1	Radiomics process	30
4.2	Feature extraction	30

4.3	Digital image. (a) Image with 5x5 pixels, with grey-level values in a range from 0 (white) and 7 (black). (b) Numerical representation of the image . . .	31
4.4	Histogram of the image	31
4.5	Example of texture	32
4.6	Co-occurrence within two-pixels distance in the horizontal direction computed for the image of Figure 4.3	34
4.7	Example of horizontal and diagonal run-length matrices for the image shown in Figure 4.3	36
4.8	LifeX icon	37
4.9	Starter window: 'texture' selection	38
4.10	Screenshot reporting the requiring inputs of the software LifeX	39
4.11	Workflow for exploiting radiomic biomarkers	40
4.12	LifeX screenshot	41
5.1	Volume values	43
5.2	Percentage difference between entropy values coming out from different discretizations	44
5.3	Percentage difference between entropy values coming out from different discretizations	44
5.4	Percentage difference between values coming out from different discretizations	45
5.5	Percentage variation of Sphericity and Compacity values	46
5.6	HISTO-Skewness, Kurtosis values	47
5.7	HISTO-Entropy and Energy values	48
5.8	GLCM-Homogeneity, Energy, Contrast values	48
5.9	GLCM-Entropy, Dissimilarity values	49
5.10	GLRLM-SRE, LRE values	49
5.11	GLRLM-LGRE, HGRE and RP values	50
5.12	GLZLM-SZE and LZE	50
5.13	GLZLM-LGZE, HGZE and ZP values	51
6.1	Gaussian Distribution	57
6.2	Lesion clinical response	60
6.3	Box Plot example	61
6.4	Distribution of the test results	62
6.5	Example of the perfect discrimination test ROC curve	63
7.1	Box Plot GLZLM-HGZE	65
7.2	Box Plots	66

7.3	HISTO Skewness, Kurtosis ROC curves	67
7.4	HGZE ROC curve	68
7.5	Box Plot HISTO Skewness	69
7.6	Contrast and Dissimilarity ROC curves	70
7.7	GLRLM HGRE ROC curves	71
7.8	Lesion absorbed Dose box plot	72
7.9	Lesion absorbed Dose ROC curve	73

List of Tables

4.1	Features used	33
5.1	Volumes inside the phantom and thresholds related to	43
5.2	Sphericity values	47
5.3	Features values related to the sphere phantom	52
6.1	Dataset	53
6.2	Sphericity values	58
6.3	Different fractions (TP, FP, TN, FN) representation	62

Introduction

The aim of this thesis is to investigate the feasibility of texture analysis on metastases of patients affected by metastatic differentiated thyroid carcinoma (MDTC). These patients are usually treated with surgery and since their metastases cells are still thyroid cells, their treatment usually involves high activity of radioiodine. The use of radioiodine (^{131}I) constitutes a consolidated therapeutic approach in Nuclear Medicine Department at A.O. Mauriziano Hospital in Turin, where the study was carried out in cooperation with the Medical Physics Department from April 2018 to March 2019.

Therefore the starting point of this thesis is to demonstrate the feasibility of the method on ^{131}I phantom SPECT images and to evaluate the prognostic impact of texture analysis on patients SPECT images.

Chapter 1 shows the State of the Art: a deep research analysis of the main studies which assert the importance of lesion dosimetry and publications of project works which managed with texture analysis in medical imaging.

Chapter 2 describes iodine and its radioactive isotopes, in particular ^{131}I and its radiometabolic therapy. In conclusion a brief description of SPECT/CT systems for diagnosis is shown.

Chapter 3 introduces lesion dosimetry: it explains the MIRD method used to compute the mean absorbed dose to lesions which are assumed spherical, describes the SPECT/CT calibration which is needed to compute the activity values starting from the amount of counts per seconds recorded by the system. Then, a dosimetric protocol applied to patients at A.O. Mauriziano Hospital is introduced.

Chapter 4 shows Radiomics recent developments in quantitative imaging and its capability of quantitative feature extraction from high-quality tomographic images useful in the decision support process. Texture analysis methodology is then illustrated and all features used are described. Features analysis is performed with a free software (LIFEx, CEA 2017) which is able to compute and extract first, second and higher-order features deeply described.

Chapter 5 describes a preliminary feasibility study which was performed using a NEMA PET IQ Phantom to validate a procedure which was following applied to patients and to understand features significance and behavior. First, a discretization analysis is performed on features computation, then, a features analysis is developed to understand the percentage variation of each feature during all the acquisition times.

Chapter 6 lists the patients lesions included in our dataset, on which features analysis was performed. Then, a statistical analysis is carried out through ROC curve analysis and box plot.

Chapter 7 summarises the most significant results obtained in this thesis work.

Chapter 8 expounds the main conclusions resulted from this study.

1

State of the art

1.1 *The importance of lesion dosimetry*

Many papers in literature deal with radioiodine therapy which constitutes the most common treatment of differentiated thyroid cancer following a total thyroidectomy. ^{131}I is a *beta*-particle emitter, but it also has penetrating *gamma* radiation, which makes it traceable in vivo through medical imaging. The amount of radiopharmaceutical to be administered to patients is a crucial topic and the activity can be established with two different approaches:

1. empirically fixed, based on disease characteristics and patient age;
2. dosimetry-based prescribed.

The first approach is characterized by a relatively lower cost and ease of administration; however, recent analyses have suggested that this method can lead to an over-treatment with the risk of exceeding maximum tolerable absorbed dose to blood [32].

Over the last decade, the use of the positron-emitting ^{124}I PET/CT imaging has become more frequent in pre-therapeutic dosimetry to predict the absorbed dose in iodine-positive lesions and organs at risk. This allows treatment personalization: optimal administered activity can be chosen to deliver the maximum dose to target while keeping organs at risks safe [48]. The pre-treatment administration involves significantly smaller activities than therapy and it is usually performed one week before the therapeutic treatment.

Since the American Thyroid Association guideline declared that there are not sufficient evidence in literature to recommend a preferred approach in activity definition, in 2016 a double experimentation was carried out at Goussave Roussy in Villejuif (France) and at Memorial Sloan Kettering Cancer Center (MSKCC) of New York (USA). The aim of the study was to compare the overall survival in the two groups of patients affected by a

differentiated thyroid cancer. The difference between the two procedures was the method to determine the administered activity: at Goussave Roussy an empirically fixed activity of 3.7 GBq was imposed, while the MSKCC of New York computed a personalized activity based on whole body/blood clearance dosimetry. All data were statistically analyzed with Chi-square and Mann-Whitney-Wilcoxon tests (t and U tests). Results recorded by MSKCC did not provide any significant advantages and clinical benefits with respect to the empirical approach, however, for what regard the amount of activity, higher values resulted to be more efficient comparing to lower fractionated activity. ^{124}I PET lesion 3D dosimetry can be suggested in order to predict the absorbed dose and compute the safest and most effective ^{131}I activity to be administered. A SPECT/CT procedure can allow to calculate the absorbed dose in other organs and in metastases, but a significant limit of the study was the not availability of safety data [17].

Many papers [32, 22, 7] suggested the importance of dosimetry in order to determine the optimal activity administration. Lesions were evaluated through a dosimetric study related to the therapy response. The European Association of Nuclear Medicine (EANM) Therapy Committee discussed the general issue of the usefulness of dosimetry in radionuclide treatment that is also part of patients' radiation protection. Moreover, pre-treatment dosimetry is the basis for a treatment planning, but also an important source of scientific information: the introduction of a dosimetry aided treatment planning can aim to increase the success rate and a consequent reduction of the number of repeated treatments in order to avoid useless treatments. Both these possibilities would improve the patient survival and its quality of life.

On the base of *Council Directive 2013/59/EURATOM* the treatment procedures to deal with the differentiated thyroid carcinoma were drawn up by AIFM (Associazione Italiana di Fisica Medica) and AIMN (Associazione Italiana di Medicina Nucleare). Patients with distant metastases are subjected to problems related to the therapeutic efficiency: they suggested that dosimetry can improve this aspect. The few published papers where dosimetry was applied agree with the fact that the evaluation of the absorbed dose to lesions improved the management of metastatic differentiated thyroid carcinoma treatments [5, 12].

1.2 Texture Analysis

Malignant tumors often show high intra-tumor heterogeneity on a microscopic level which can be quantified with texture analysis algorithms. Morphologic imaging has been recently used to evaluate tumor heterogeneity [9]. Several publications [26, 42, 38, 16] show the importance of texture analysis. The use of texture analysis has been widespread

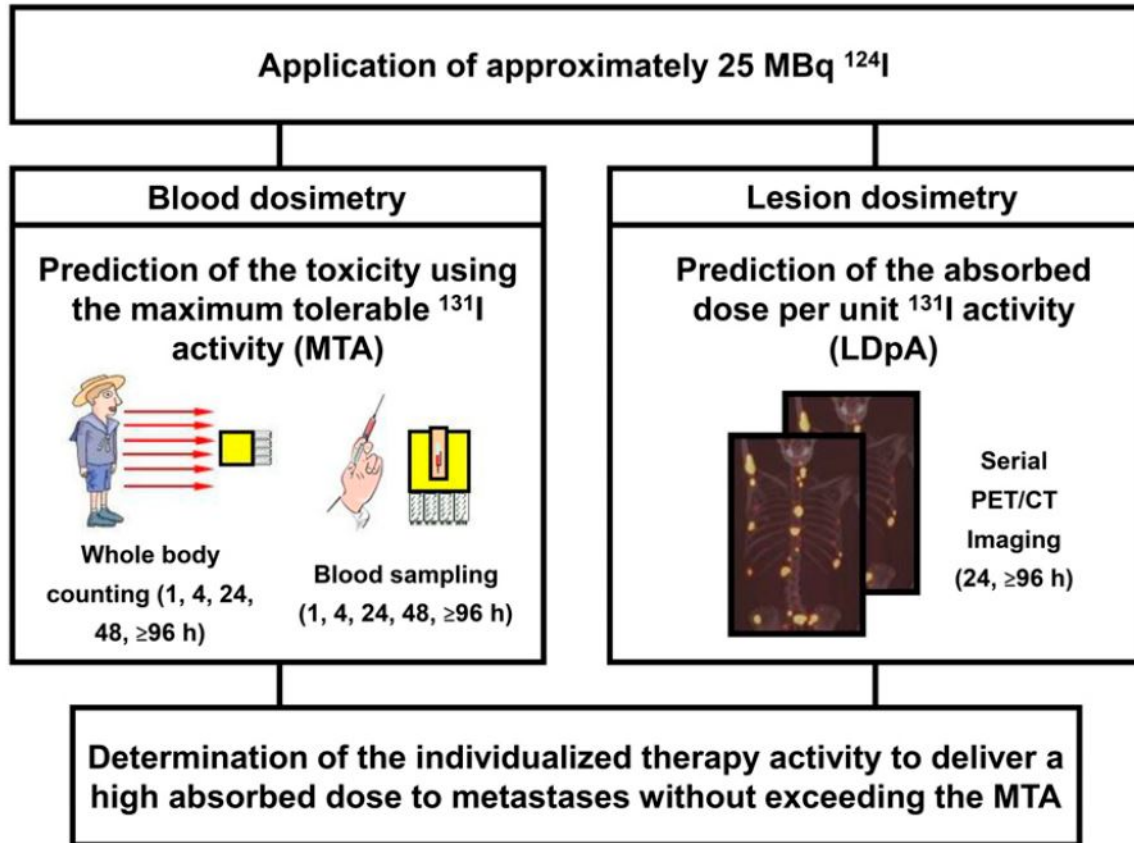


Fig. 1.1: Simplified illustration of dosimetry approaches to determine the administered radionuclide activity

[41]

in MR and CT imaging since the early 1990s [29]. In CT, imaging tumor heterogeneity results to be an important predictive factor of the metastatic renal cell cancer treatment response; in MR imaging heterogeneity of liver lesions was index of chemotherapy response and using this imaging technique, texture analysis was also used to distinguish tumor from non-tumor tissues in prostate.

In the end of 2000s [29], PET has been used to assess intra-tumor heterogeneity characterization which is referred to the radio-tracer uptake spatial distribution: it has the ability to directly visualize functional information and, depending on the radio-tracer used it can provide useful information about cell metabolism. Compared to CT or MR, PET images seemed not to be useful for texture analysis because of their relatively low spatial resolution, that represents its major drawback, but the development of PET/CT systems improved their accuracy.

Many recent publications [20, 55, 14] show that heterogeneity measurement on PET images provides important information on prognosis and therapy effects in oncologic patients and in addition, it has a potential use in tissue classification [62]. Texture analysis

is one of the approaches used to quantify the heterogeneity of image voxel intensities: it involves a complex work-flow with numerous steps and a very large number of parameters to be computed which make this process tricky and a comparison of results between studies difficult.

2

Nuclear Medicine in metastatic thyroid carcinoma treatment

2.1 Iodine and its radioactive isotopes

Iodine has been discovered in 1811 by Bernard Courtois. Its atomic number is 53 and it belongs to the halogen section of the periodic table. It is solid at room temperature and it is the least reactive element of its class. Iodine has more than 30 isotopes; among them only ^{127}I is stable and abundant in nature.

^{131}I is the most common artificial radioisotope which appears in two main processes [59]:

1. *Uranium-235 (n,f) fission reactions*: heavy nuclei absorb thermal neutrons and the fission process produces some radionuclides, including ^{131}I . Figure 2.1(a) shows U-235 fission yield fragments as a function of mass, the second peak represents the ^{131}I production;
2. *Tellurium-130 (n,γ) neutron irradiation* in a nuclear reactor: target nucleus captures one thermal neutron and it emits γ -rays producing an isotope of the same element, as shown in Figure 2.1(b).

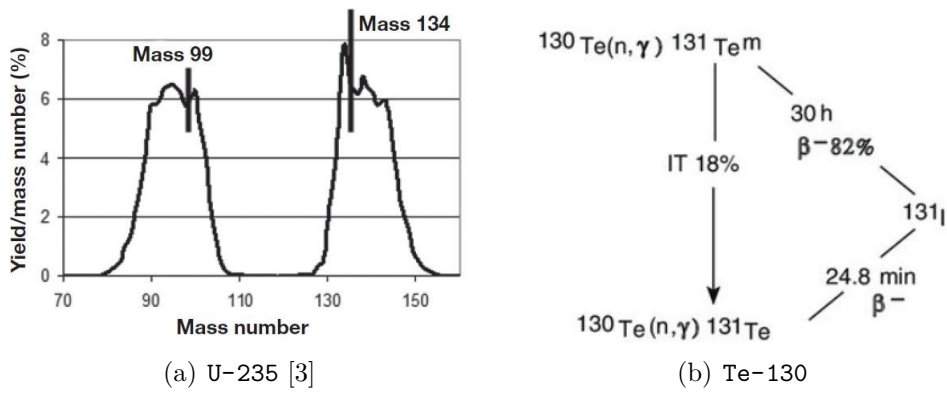


Fig. 2.1: ^{131}I production process

Radioiodine is mostly used in medical and pharmaceutical fields: it has an half-life of about 8 days and primary it is a β -emitting isotope as shown in Figure 2.2.

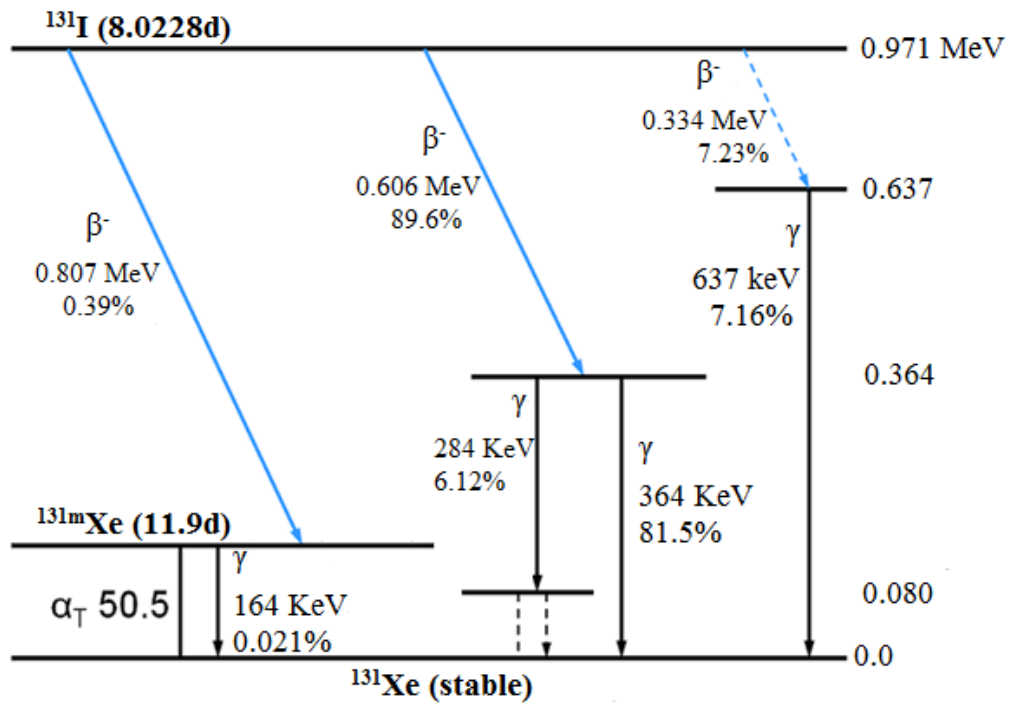


Fig. 2.2: Nuclear decay scheme for I-131 [59]

^{131}I nucleus decays emitting β particles which penetrate biological tissues for 0.6-2.0 mm. β particles medium energy is 192 keV [59] while an abundance of 89.6% is emitted at 606 keV, The β emission is also followed by energetic γ rays (mainly 364 keV) that can be used to image the biodistribution.

A.O. Mauriziano Hospital usually requires Sodium Iodide (^{131}I) in the form of capsules (THERACAP 37-5550 MBq) which are produced by GE HealthCare Buchler GmbH & Co. KG in Braunschweig (Germany) [*Agenzia Italiana del Farmaco*].

2.2 Radiometabolic therapy with ^{131}I

Cancer has been treated with radiopharmaceuticals since the 1940s [3]. The radionuclide originally used, including ^{131}I and ^{32}P , for thyroid and leukemia treatments are still in use. In particular, for both malign and benign thyroid diseases, the use of radionuclide therapy is one of the most common and consolidated therapeutic option.

During the last decades the occurrence of thyroid cancer has been steeply increasing [37]: the most prevalent kinds (90-95%) are originated from papillary and follicular cells [31] and they are distinguished as *differentiated thyroid cancers* (DTCs). This carcinoma typology is called *differentiated* because it is constituted by thyroid cells maintaining the *capacity of uptaking iodine*.

The DTC is the most common malignancy of the endocrine system: in the initial stage its treatment requires a total thyroidectomy which consists on the global eradication of the thyroid gland and, if necessary, lymph nodes dissection; and finally, a nuclear medicine therapy with ^{131}I in order to completely remove the residual thyroid tissues after surgery [39, 15].

Physiologically the thyroid cells accumulate the stable isotope ^{127}I . Since thyroid cells are not able to distinguish between stable and radioactive isotopes, the administration of ^{131}I to patients leads to an accumulation of the radionuclide in the thyroid gland, exactly where it is expected. The nuclear medicine therapy consists of either oral administration of ^{131}I carried out in gelatin capsules or intravenous injection.

This therapy with ^{131}I is quite empiric: it consists in the administration of fixed activities to patients within a range between 28-3700 MBq. For the ablation of post-operative residual thyroid tissues, the usually activity administration is 1850 MBq (50 mCi) [*Dosimetria durante terapia di carcinoma differenziato della tiroide metastatico - Protocollo dosimetrico*].

Local recurrence and distant metastases can occur approximately in 10-20% of cases in 10 years after the initial surgery [31]. The most frequent thyroid carcinoma metastases are bones, vertebral and cerebral ones. Since the metastases cells are still thyroid cells,

they are characterized by iodine avidity and their treatment usually involves further and higher administration of radioiodine.

Metastases therapy could be carried on with another *RAI* (Radioactive Iodine) therapy, a metastasectomy or an external beam radiotherapy [30]. The presence of metastases leads to an increase in terms of therapeutic administered activity that is usually in the range between 3700-5550 MBq (100-150 mCi) [24]. In only one-third of the patients a complete response is achieved [31]. The remaining patients usually become *radioiodine-refractory* (RR-DTC) and they require a change in the disease medical management since they lose the ability to be iodine-avid; hence, the probability to be cured by further ^{131}I therapies becomes very low and adverse effects may increase [8, 47].

As a matter of facts, the risk of cell *dedifferentiation* can occur in case of an under-treatment in further administration that can lead to a decrease in the iodine avidity of the tumor. In addition, patients may be considered radioiodine-refractory if they have already received a RAI activity of more than 600 mCi [51]; patients with local advanced or end-stage disease that are not manageable with surgery are considered as RR-DTCs since radioactive iodine activity, when thyroid is not removed, is not effective [31].

β and γ emissions generated from the administration of the radioactive isotope ^{131}I , that is absorbed by all the iodine-avid cells, are able to treat the thyroid diseases.

Hence, the radionuclide therapy has a double effect: the *diagnostic* and the *therapeutical* one. Radioiodine is rapidly absorbed and then distributed within the body extracellular fluid towards the thyroid tissues where it is accumulated. Beta emissions coming from the radioiodine can selectively harm or kill DTC cells; they can also be imaged in gamma cameras through the detection of γ -rays simultaneously emitted by ^{131}I , in order to visualize any residual thyroid tissues after the surgery or some possible metastatic lesions.

In this perspective, the beneficial effects of ^{131}I administration consist in the detection of thyroid cells metabolic activity of which suggests the localization of undiagnosed regional or distant metastatic lesions and then, in addition, the destruction of the thyroidal tissues through its beta emissions [36].

2.3 Diagnosis with SPECT-CT

Gamma camera is one of the main nuclear medicine imaging devices. It is a planar device which detects γ -rays emitted by the radiotracer distributed in the patient body and it consists of two main components:

1. the collimator;
2. the radiation detector.

The *collimator* is a critical component able to select the direction of the γ -rays entering the device. It is made of a highly absorbing material slab, ordinarily of lead, which is penetrated by many fine holes through which only the rays with a selected direction pass, while the others are absorbed. Each radionuclide requires a specific collimator as represented in Figure 2.3 and, since ^{131}I emits high energy γ -rays, the ones needed in our analysis are HEAP (High Energy All Purpose) or HEGP (High Energy General Purpose).



Fig. 2.3: All possible collimators which can be required and mounted on for any acquisition

Next to the collimator, the detector is placed. It is composed by a single large area ($50\text{ cm} \times 40\text{ cm}$) [3] and it involves the following components, as it is shown in Figure 2.4:

- the *scintillation counter*;
- *photomultiplier tubes*;
- *electronics and computer systems*.

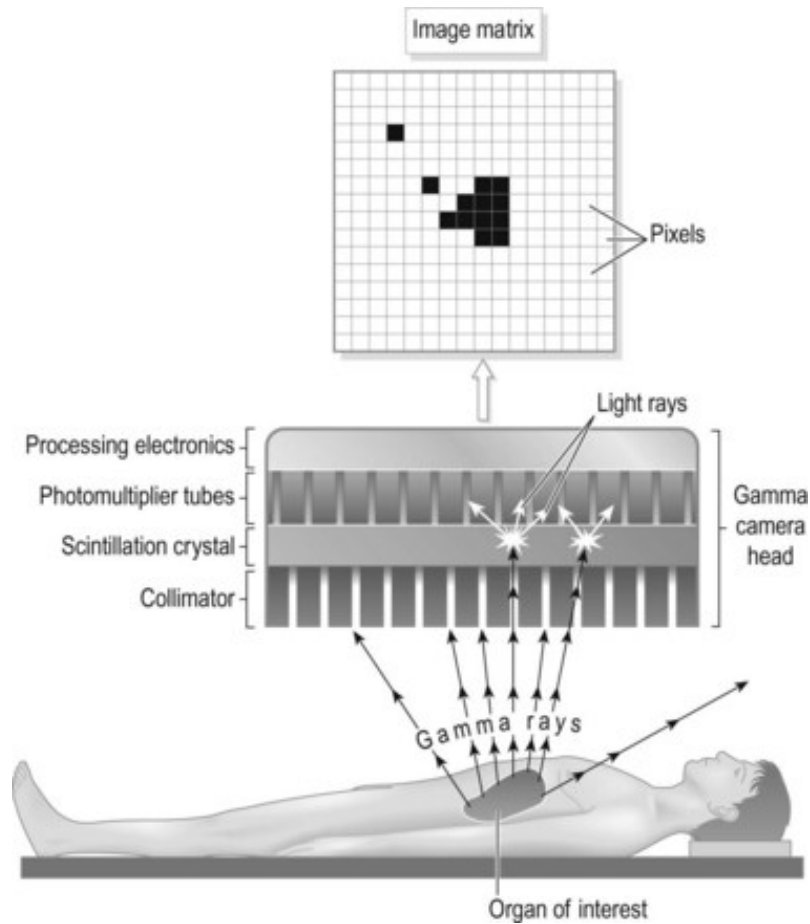


Fig. 2.4: Schematic of a gamma camera for detecting single protons

The *scintillation counter* is an inorganic crystal usually made of *Sodium Iodide doped with Tallium* NaI(Tl). The mechanism which allows the radiation detection is based on the electronic structure with bands of the NaI(Tl). The NaI has two electronic bands: the *valence* and the *conduction* one, separated by an energy gap. The doping with Tallium impurities leads to the generation of energetic levels between the two bands. This mechanism converts the ionizing radiation of incident rays into low intensity visible light: the incident γ -ray leads to an excitation of an electron of the crystal that moves to the conduction band and then, the de-excitation at ground state generates an about 3 eV photon emission which corresponds to the visible spectrum.

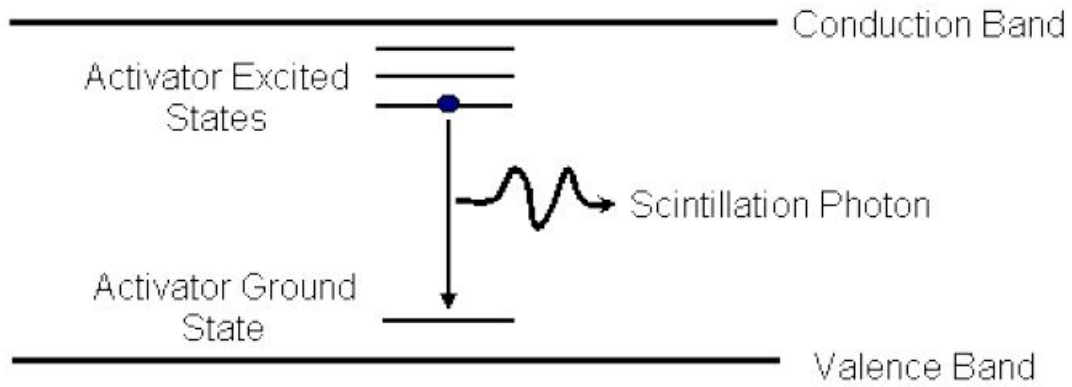


Fig. 2.5: Inorganic scintillators mechanism

The light signal coming out from the scintillator needs to be converted in electric signal and amplified. *Photomultiplier tubes* (PMTs) are constituted by vacuum tubes with a photo-cathode, releasing electrons by photoelectric effect, which is coupled with an electron multiplier producing an electric signal proportional to the photon energy incident on the scintillation crystals.

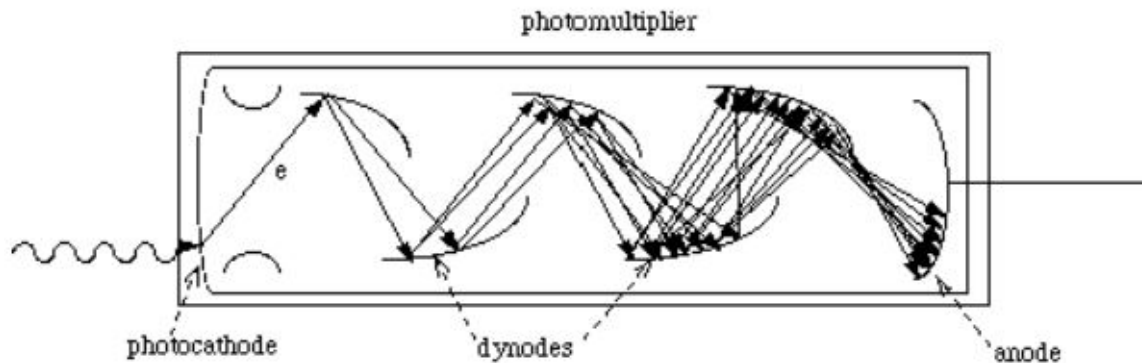


Fig. 2.6: Photomultiplier tube scheme

The energy determination during scintillation counting has associated an uncertainty according to the fact that photons generated in the scintillator eject electrons into photomultiplier tubes with a probability of success of $\frac{1}{5}$ [3].

The system efficiency can be defined in two different ways, in *absolute* or *intrinsic* term.

$$\epsilon_{\text{abs}} = \frac{\# \text{ pulses recorded}}{\# \text{ photons emitted by the source}}$$

that takes into account the source attenuation, while

$$\epsilon_{\text{int}} = \frac{\# \text{ pulses recorded}}{\# \text{ photons incident on the detector}}$$

considers the capability of the detector to interact with the radiation and it depends on its material and dimensions.



Fig. 2.7: HEAP collimators mounted up with detectors on gamma camera head

Complex *electronics and computers systems* handle with the estimation of energy and position of the received signal producing 2-D planar images from the acquired data in terms of number of counted photons.

The gamma camera head is connected to the *gantry system* that supports and moves the device around the patient bed as shown in Figure 2.8. In this way *single-photon emission computed tomography* (SPECT) performs a circular acquisition, providing a sequence of 2-D projections from multiple different angles around the object of interest.



Fig. 2.8: Gamma camera connection to gantry system

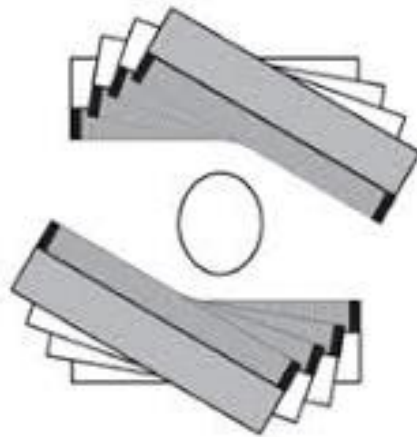


Fig. 2.9: Circular SPECT acquisitions scheme

The SPECT system has a radius of 33 cm and, moving around the patient, it records 64 views with a 20 s/view acquisition time. It provides very little anatomical information, making it difficult the localization of regions where an abnormal tracer accumulation occurs. In order to face up to this problem, an high resolution anatomic imaging (CT) is combined. The CT system has 130 kV voltage, 0.8 s rotation time and it acquires and reconstruct defines 3 mm thickness slices. A computed tomography is used for attenuation correction, it is necessary to obtain anatomical information and it affects SPECT quantification in order to develop a dosimetric analysis at voxel level.

Combined SPECT-CT systems provide combined anatomical and functional 3-D imaging data which have to be spatially co-registered, in order to provide information

about the disease localization and to improve diagnostic performance with respect to an analysis with separate procedures. In this perspective, this combined system provides an higher resolution with a more accurate quantification of all the lesions, especially for the very small ones.

The SPECT subsystem is located next to the CT one and acquisitions are realized sequentially. Usually, after the patient positioning on the couch, a SPECT acquisition is performed followed by a CT one. The total examination time depends on the number of different body regions to be examined and it ranges between 20 minutes and one hour.

Each kind of detector system, according to its physical properties and since it records discrete events, needs to take into account time, energy and position resolutions, strongly coupled with the statistics of phenomena in interest.

A critical issue is the *response time* of the detector which is the time, after the detection of one radiation quantum, during which the detector is not able to detect other radiations. This concept is better understood with the definition of a parameter called *dead time* τ which is the minimum time separating two pulses such that they are recorded separately.

This system does not consider radiation energies far from the one of interest: the ability to distinguish two peaks at different energies is the *energy resolution* R of the system. Assuming a Poissonian distribution of the counting of pulses, the energy resolution is defined as

$$R = \frac{FWHM}{E_0}$$

where FWHM is the *Full Width at Half Maximum* (Figure 2.10).

The energy resolution value is a dimensionless number and for scintillators it is in the interval range 5-10% of the energy considered.

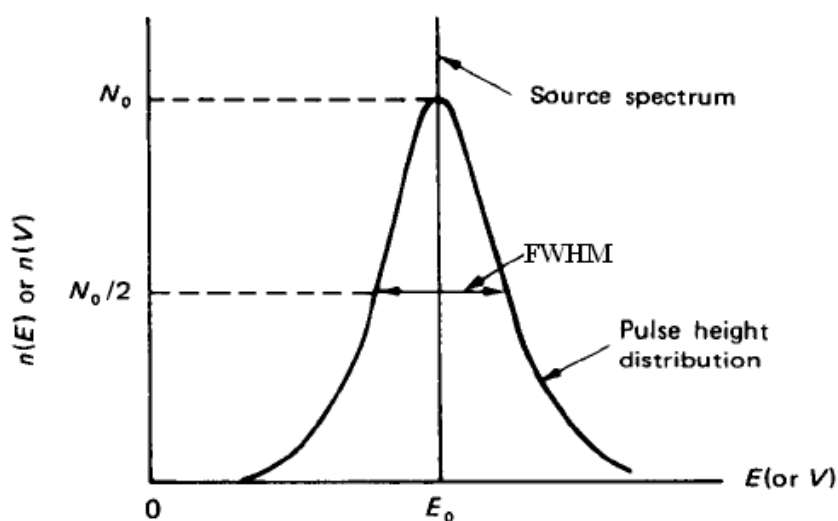


Fig. 2.10: Energetic resolution in gamma spectrometry

Spatial resolution is defined as the *Full Width at Half Maximum* of the response of the system at a point source. It defines the minimum distance at which the SPECT-CT is able to differentiate two different sources. In SPECT-CT systems it is on the order of 5-25 mm.

The final image will record all the counts describing a peak, whose rise value depends on photon energies, crystal width, number of photo-multipliers and electronic systems.

3

Lesion dosimetry

The activity used in radioiodine therapy still remains subject of discussion. As explained in Paragraph 1.1, usually patients are treated with standard empirically chosen activities. The decision depends on the physician's rating of the highest safe or *adequate* dosage or else it is determined by a pre-therapeutic dosimetry performed to estimate the absorbed dose in lesions and organs at risk in order to choose the optimal activity value.

The choice of empiric standard activity can lead to a risk of either under-dosing the patient or exceeding common safety limits, in addition not to consider the individuality of the patient [58, 57] because it is not able to determine the minimal radioiodine activity that will lead to the maximum allowable reasonably safe absorbed dose [34]. Therefore, it could be useful a dosimetry-based approach: it can contribute to an effective management of differentiated thyroid carcinoma and it is essential to optimize the administered activity. This approach takes into account the minimum effective absorbed dose and the maximum tolerated value, in order to replace the conventional fixed activity regimen by a modern setting, allowing the increase of the administered therapeutic activity avoiding undesired side effects. Furthermore, dosimetric analysis is helpful in developing a personalized diagnostic and a therapeutic plan: it is possible to predict the treatment response of each lesion, but some metastases might not respond completely to the therapy and then they may require an additional personalized treatment in order to eradicate them.

3.1 *MIRD method*

A standard regulation for internal dosimetry computation in nuclear medicine was developed in 1968 by the *Medical Internal Radiation Dosimetry Committee of the Society of Nuclear Medicine* in USA, generally known as the *MIRD System* of internal absorbed dose calculation.

MIRD Pamphlet No. 16: Techniques for Quantitative Radiopharmaceutical Biodistribution Data Acquisition and Analysis for Use in Human Radiation Dose Estimates

Jeffrey A. Siegel, Stephen R. Thomas, James B. Stubbs, Michael G. Stabin, Marguerite T. Hays, Kenneth F. Koral, James S. Robertson, Roger W. Howell, Barry W. Wessels, Darrell R. Fisher, David A. Weber and A. Bertrand Brill
Nuclear Physics Enterprises, Cherry Hill, New Jersey; University of Cincinnati, Division of Medical Physics, Cincinnati, Ohio; Radiation Dosimetry Systems of Oak Ridge, Inc., Knoxville, Tennessee; Oak Ridge Institute for Science and Education, Radiation Internal Dose Information Center, Oak Ridge, Tennessee; Veterans Affairs Medical Center 640/151, Palo Alto, California; Department of Nuclear Medicine, University of Michigan, Ann Arbor, Michigan; Gaithersburg, Maryland; Division of Radiation Research, Department of Radiology, University of Medicine and Dentistry of New Jersey, Newark, New Jersey; Department of Radiology, George Washington University Medical Center, Washington, DC; Pacific Northwest National Laboratory, Richland, Washington; Department of Radiation Research, University of California Davis Medical Center, Sacramento, California; Department of Radiology, Vanderbilt University School of Medicine, Nashville, Tennessee

This report describes recommended techniques for radiopharmaceutical biodistribution data acquisition and analysis in human subjects to estimate radiation absorbed dose using the Medical Internal Radiation Dose (MIRD) schema. The document has been prepared in a format to address two audiences: individuals with a primary interest in designing clinical trials who are not experts in

planning error analysis techniques and selected calculational examples. The utilization of the presented approach should aid in the standardization of protocol design for collecting kinetic data and in the calculation of absorbed dose estimates.

J Nucl Med 1999; 40:37S-61S

Fig. 3.1: MIRD Pamphlet No. 16

The aim of this formalism is to provide a standard calculation of the mean absorbed dose to internal organs due to nuclear radioactive sources.

After radionuclide introduction, the organs inside the body are defined into three main categories:

- *source organs*, which accumulate the amount of radionuclide;
- *target organs*, or organs object of the treatment, which receive the radiation;
- *organs at risk*, or the healthy organs, that may record an important leading to toxicity.

The MIRD method takes into account the geometries of source and target organs and the attenuation properties of the body tissues in order to estimate the radiation dose to targets due to source radioactivity.

Radiation originating from decays within one or more source organs is responsible for the energy deposition in a target organ. In case of ^{131}I treatment, for instance, the thyroid and the iodine-avid metastases are at the same time source and target organs.

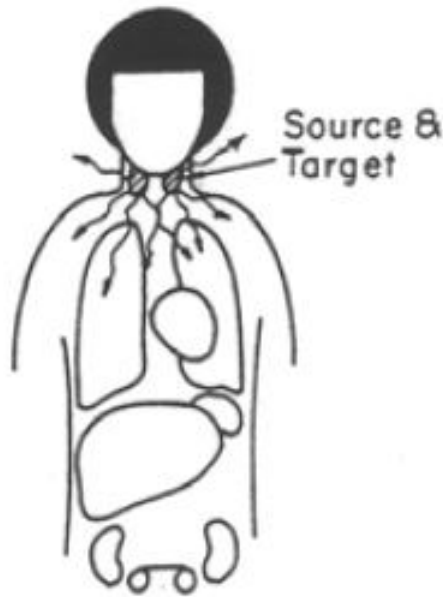


Fig. 3.2: Thyroid as source and target organ

The application of MIRDA method assumes that the radioactive concentration of the substance within source organs has an uniform distribution and the estimation of the mean absorbed dose can be predictive of biological effects [18].

The estimation of the mean absorbed dose to a target organ can be computed using the following quantities:

- *cumulated activity* \tilde{A} (Bq · s) of the administered radio-pharmaceutical, which represents the total number of nuclear transformations in the source organ;

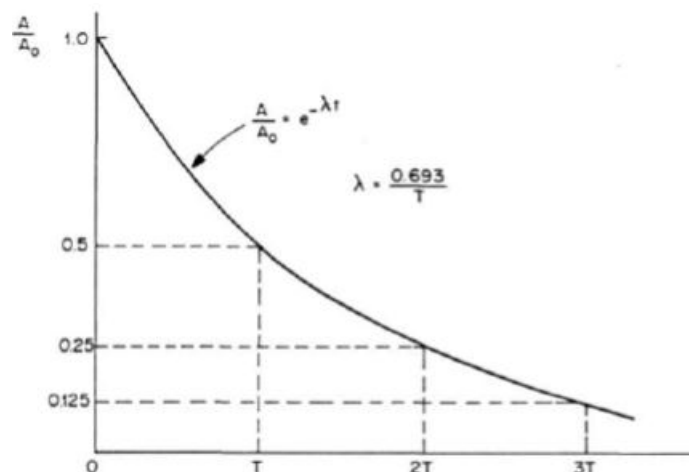


Fig. 3.3: cumulated activity

- *residence time* τ
- *fraction of energy released* from the source that is *absorbed* in the considered target organ, ϕ ;

The absorbed dose is computed as the product of the time-integrated activity and the S factor.

$$D = \tilde{A} \cdot S \quad [3]$$

D is defined as the quantity of radiation energy deposited in a target organ per unit tissue mass (J/kg)

$$D = \frac{dE}{dm}$$

and its unit is called Gray (Gy), while the S (Snyder) factor (or *Dose Factor*) shows the link between the activity and the absorbed dose rate and it is measured in $\frac{mGy}{MBq \cdot s}$ [53].

The source and the target organs have to be well defined in terms of volumes: the source region is denoted as r_S , while r_T identifies the target one.

$$D(r_T) = \tilde{A}(r_S) \cdot S(r_T \leftarrow r_S)$$

The S factor represents the mean dose per unit cumulated activity and it is equal to the product of the absorbed dose and the absorbed fraction. The *absorbed fraction* ϕ , as shown in Equation 3.4, is the ratio between the amount of energy emitted from the source and the one absorbed in the target organ.

$$\phi = \frac{E_{em}(S \rightarrow T)}{E_{ab}(T \leftarrow S)} \quad (3.1)$$

so that

$$S(r_T \leftarrow r_S) = \frac{E\phi}{M(r_T)}$$

The absorbed fraction values, that are in the range between 0 and 1, depend on:

- the type and energy of radiation;
- the medium between source and target;
- the size, shape, mass and composition of source and target organs.

$$\phi(r_T \leftarrow r_S, E_i)$$

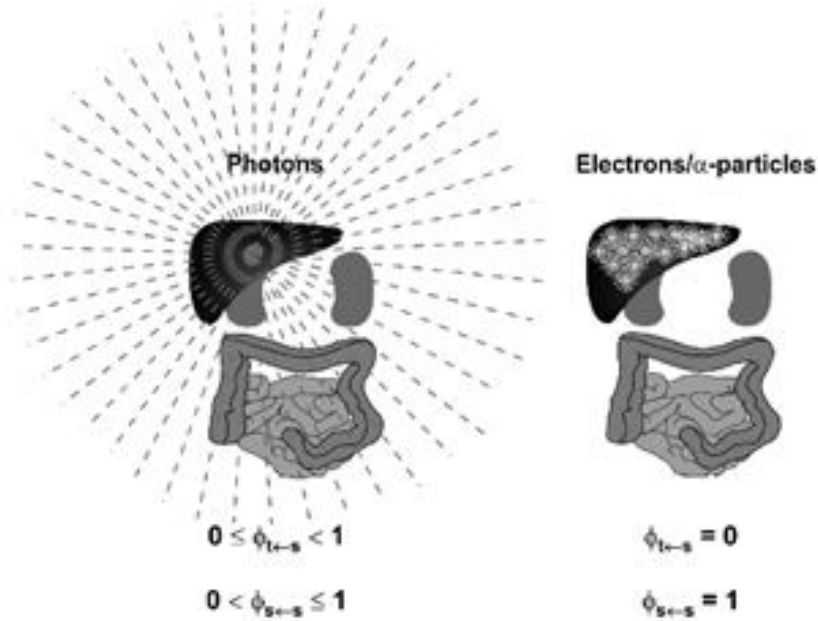


Fig. 3.4: Absorbed fraction

This factor can be defined as the absorbed dose in r_T per nuclear transformation that occurs in r_S .

For radionuclides that decay emitting β radiations, like ^{131}I , since they are non-penetrating, the absorbed fraction is assumed equal to 1 for self-irradiation and zero for other organs irradiation.

S values for human phantoms are built with OLINDA/EXM (Organ Level Internal Dose Assessment code with an EXponential Modeling function) software as a function of mass and they are listed in tables, as reported in Table 3.5. This software includes values for most radionuclides and computes the absorbed dose to different organs in the body. Human phantoms do not include tumors: a sphere model carries out values related to spheres with masses ranging from 0.01 to 6000 g [3]. For radionuclides with multiple radiation emissions, internal dose computation can be quite time-consuming and, to face up to this complication, the MIRDC Committee published tables reporting S factors that include combinations of more than 100 different radionuclides and 20 pairs of sources and target organs [13]: these computations are performed with standard Monte Carlo radiation transport simulations.

S, Absorbed Dose per Unit Cumulative Activity (rad/ $\mu\text{Ci} \cdot \text{hr}$) for ^{131}I

Target Organs	Source Organs									
	Intestinal Tract						Kidneys	Liver	Lungs	Other Tissue (Muscle)
	Adrenals	Bladder Contents	Stomach Contents	SI Contents	ULI Contents	LLI Contents				
Adrenals	3.1E-02	6.1E-07	6.3E-06	3.9E-06	2.7E-06	1.4E-06	3.2E-05	1.4E-05	6.9E-06	4.2E-06
Bladder wall	3.3E-07	1.2E-03	1.0E-06	8.5E-06	5.6E-06	1.7E-05	1.0E-06	7.4E-07	1.8E-07	5.0E-06
Bone (total)	4.1E-06	1.8E-06	1.8E-06	2.5E-06	2.2E-06	3.2E-06	3.0E-06	2.3E-06	3.0E-06	3.0E-06
GI (Stom. wall)	8.2E-06	8.8E-07	9.7E-04	9.9E-06	1.0E-05	5.0E-06	9.4E-06	5.4E-06	5.2E-06	3.9E-06
GI (SI)	2.6E-06	7.6E-06	7.3E-06	6.0E-04	4.6E-05	2.6E-05	7.8E-06	4.6E-06	6.9E-07	4.4E-06
GI (ULI wall)	2.8E-06	6.6E-06	9.5E-06	6.5E-05	1.1E-03	1.2E-05	8.1E-06	7.0E-06	9.1E-07	4.6E-06
GI (LLI wall)	8.4E-07	2.0E-05	3.6E-06	1.9E-05	8.4E-06	1.7E-03	2.4E-06	8.1E-07	2.6E-07	4.8E-06
Kidneys	3.2E-05	9.6E-07	9.5E-06	8.7E-06	7.7E-06	2.5E-06	1.5E-03	1.1E-05	2.7E-06	4.0E-06
Liver	1.4E-05	7.2E-07	5.6E-06	5.1E-06	7.1E-06	9.0E-07	1.1E-05	3.0E-04	6.8E-06	3.1E-06
Lungs	6.7E-06	1.1E-07	5.0E-06	8.5E-07	8.9E-07	2.8E-07	2.5E-06	6.8E-06	4.5E-04	3.7E-06
Marrow (red)	7.5E-06	4.1E-06	3.2E-06	7.9E-06	6.9E-06	9.7E-06	7.6E-06	3.3E-06	3.8E-06	4.1E-06
Other tissue (muscle)	4.2E-06	5.0E-06	3.9E-06	4.4E-06	4.1E-06	4.8E-06	4.0E-06	3.1E-06	3.7E-06	1.9E-05
Ovaries	1.6E-06	1.9E-05	1.4E-06	2.7E-05	3.4E-05	5.0E-05	3.4E-06	9.6E-07	4.0E-07	5.6E-06
Pancreas	2.4E-05	7.9E-07	5.0E-05	5.8E-06	5.8E-06	2.0E-06	1.8E-05	1.2E-05	7.5E-06	5.0E-06
Skin	1.8E-06	1.7E-06	1.5E-06	1.4E-06	1.4E-06	1.6E-06	1.8E-06	1.6E-06	1.8E-06	2.4E-06
Spleen	1.8E-05	5.6E-07	2.7E-05	4.4E-06	3.7E-06	2.5E-06	2.4E-05	2.7E-06	6.2E-06	4.1E-06
Testes	1.7E-07	1.4E-05	1.3E-07	1.0E-06	1.2E-06	5.7E-06	3.9E-07	3.0E-07	5.7E-08	3.4E-06
Thyroid	5.2E-07	2.1E-08	3.9E-07	9.5E-08	1.0E-07	4.1E-08	2.4E-07	5.7E-07	3.0E-06	3.8E-06
Uterus (nongravid)	3.4E-06	4.3E-05	2.4E-06	2.5E-05	1.3E-05	1.7E-05	2.6E-06	1.2E-06	2.7E-07	5.9E-06
Total body	1.1E-05	5.9E-06	6.7E-06	1.0E-05	8.2E-06	8.8E-06	1.1E-05	1.1E-05	9.9E-06	9.8E-06

Fig. 3.5: S factor values

The *cumulated activity* $\tilde{A}(r_S, T_D)$ stands for time-integrated activity in r_S over T_D and it is defined as the product of the number of decays (Bq) that take place in a certain source region and its residence time (s) in the source organ. It is a significant quantity because, in order to estimate the dose delivered to target organs, it is necessary to consider both the amount of radioactivity in the source organ and the time frame during which it is cumulated.

$$D(r_t, T_D) = \tilde{A}(r_S, T_D) \cdot S(r_T \leftarrow r_S) \quad [18]$$

where

$$\tilde{A} = A_0 \cdot \tau$$

with A_0 that corresponds to the administered activity.

3.2 SPECT-CT Calibration

As already explained, the MIRD method needs *cumulated activity* as input. Unfortunately, SPECT system does not provide any information about the activity within volume of interest, only a measure of how many *counts-per-second* (cps) are recorded by detectors. It is therefore necessary a calibration of the system in order to convert *cps* into *activity*. The calibration system has to be carried out for every radionuclide used.

The SPECT-CT used in this study is a Siemens Intevo installed with High Energy High Resolution (HEHR) collimators dedicated to ^{131}I imaging at A. O. Ordine Mauriziano Umberto I Hospital. The tomographic emission images are characterized by 256×256 matrices with $2.4 \times 2.4 \times 2.4 \text{ mm}^3$ voxel size, equivalent to a 61 cm Field Of View (FOV).

The SPECT system calibration is performed using a phantom filled with known activities: in order to standardize the procedure the international *NEMA PET-CT spheres phantom* is used. It is composed by a body phantom made of water, a cylindrical lung insert (volume of 130 cc) and an insert with six spheres of various sizes (inner diameter 10, 13, 17, 22, 28 and 37 mm, equivalent to 0.5, 1.1, 2.6, 5.6, 11.5, 26.5 cc) filled with a liquid homogeneous mixture of ^{131}I .



Fig. 3.6: NEMA PET-CT phantom

The spheres of 1.1, 5.6, 11.5 cc and the cylinder of 130 cc were filled with ^{131}I known activities, 13 MBq/cc, on the contrary the remaining spheres and the body phantom were filled with water. Several acquisition parameters affect the calibration, but the most important are:

- distance between gamma camera head and patient: this parameter depends mainly from the *radius of acquisition*. Changing in radius leads to changing in sensitivity,

resolution and cps. For this reason the SPECT system was calibrated at 3 different radius: 25 cm, 28 cm, 33 cm;

- *size of volume*: the partial volume effect recovery coefficient needs to be evaluated. It is defined as the ratio between the measured activity and its real value measured in the same region of interest $PVERC = \frac{A_{measured}}{A_{true}}$;
- the *dead time* index

	Dead Time (%)
Detector 1	0.50
Detector 2	0.25

Fig. 3.7: Dead time indices

whose values are computed by the medical device and, since it can be relevant, it is important to take it into account in order to obtain the real value of counts-per-second:

$$cps_{true} = cps_{measured} \frac{100}{100 - \%deadtime}$$

The *calibration factor* CF is calculated as the ratio between the known activity, corrected for decay, and the cps_{true} . The CF obtained is $4.0 \cdot 10^{-5} \frac{MBq}{cts}$: it defines a relation between the number of counts recorded and the activity, in order to obtain the amount of MBq delivered to each lesion starting from the counts collected into them. Finally, the activity value can be reached through the correction for the dead time, the partial volume effect and the calibration factor.

$$Activity = cps_{true} \cdot \frac{CF}{PVE \cdot RC}$$

The protocol was validated, but lesions with volume smaller than 2.6 cc are not adequate for dosimetry with SPECT-CT system.

In Figure 3.8 the SPECT reconstruction procedure is represented.

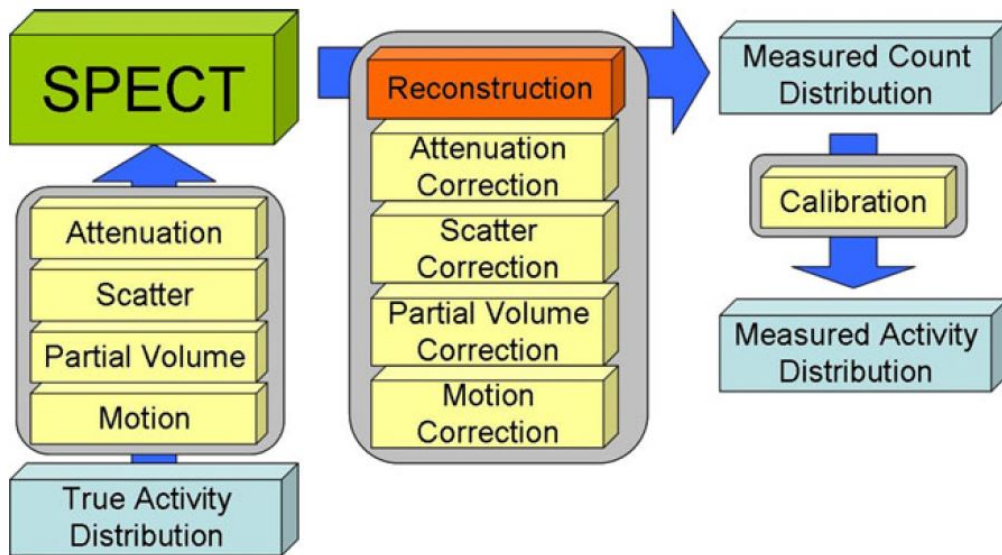


Fig. 3.8: SPECT reconstruction procedure

Figure 3.9 shows how the sphere phantom appears in SPECT acquisition.

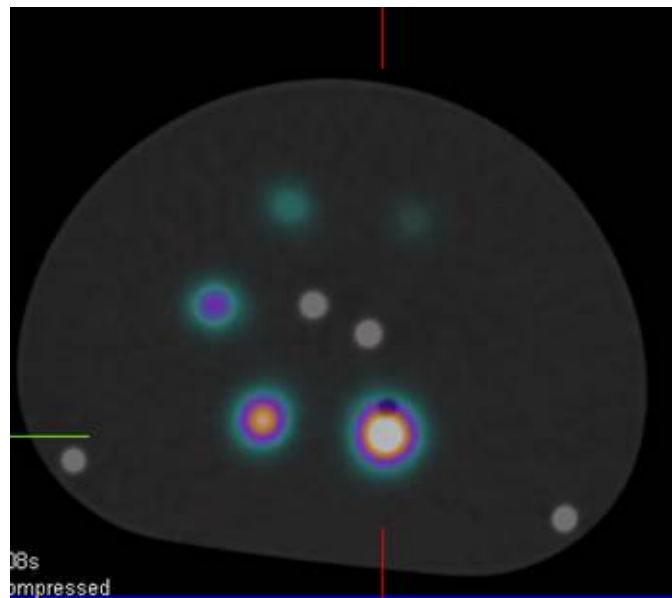


Fig. 3.9: SPECT acquisition of the spheres

3.3 Dosimetric protocol on the patient

The administered therapeutic activity is defined according to an *optimization criterion* that requires a minimization of the radiation dose to not-target organs respecting the toxicity limits and the maximization of the administered activity to the lesions.

According to these assumptions the internal dosimetry protocol limits the absorbed dose to blood as a surrogate for red marrow at 2 Gy maximum value [*Dosimetria durante terapia di carcinoma differenziato della tiroide metastatico - Protocollo dosimetrico*]. For what regards metastases, the absorbed dose value to reach a complete remission probability of 53% must be greater than 100 Gy [19].

One of the purposes of the dosimetry analysis is the estimation of the dose delivered to each metastases and the evaluation of their therapeutic response. In order to evaluate the individual biokinetics parameters, before treatment, a dosimetric study is performed; a small tracer amount of radio-pharmaceutical is injected and biokinetics parameters are derived from the activity-time curves built starting from activity measurements at different times.

The dosimetric protocol adopted at Mauriziano Hospital provides a pre-treatment radio-pharmaceutical administration of about 15 MBq one week before the hospitalization. The patient affected by metastatic thyroid carcinoma is usually hospitalized on Monday: late in the morning a therapeutic activity of 3.7-11.2 GBq, higher with respect to the previsional one to be effective for tumor treatment, is orally administered through capsule containing ^{131}I .

In nuclear medicine, many processes involve a changing in the radiopharmaceutical distribution within the patient body. In order to determine the proceeding of the radiation concentration, the iodine collimators are installed and then, four SPECT acquisitions are performed.

The uptake of Iodine in the thyroid tissues reaches its maximum in 24-48h, counting the 50% of its maximum peak after 5h. This value is affected by several factors such as patient age and thyroid volume [24]. After four hours, the patient whole body measurement is performed with a gamma camera which detects the γ -rays emitted from the body itself: the activity remains in the patient after the radio-pharmaceutical administration, hence to understand the location of the metastases. The patient on the couch is located between detectors horizontally orientated in order to obtain a two-dimensional screen of the body.



Fig. 3.10: SPECT/CT system

The location of the couch must be specified in order to maintain the same patient positioning during all the following acquisitions. Once physicists and radiologist technicians observe the location of the most captant regions in the patient body, the first SPECT and CT scans are performed. In the case of sparse lesions, different scans are required because of the limited dimensions of the detectors. The following SPECT acquisitions are performed on Tuesday, Thursday and Friday respectively.

4

Radiomics in SPECT-CT imaging of Iodine captants lesions

In the past decade, the medical image analysis field has been developed exponentially [25]. The term *radiomics* describes a practice consisting in the extraction of quantitative features from high-quality medical tomographic image into exploitable high-dimensional data, useful in the decision support process.

Radiomics is an emerging discipline in quantitative imaging and it offers a wide potential to develop precision medicine approaches: it involves statistical data combined with patient characteristics in order to develop models which may potentially improve diagnostic and predictive accuracy.

At the beginning radiomics has been developed in oncological fields, but it is potentially applicable to a wide number of conditions.

The process involves six main steps:

1. acquisition of high-quality medical images;
2. identification of the volume of interest (VOI);
3. segmentation of the volume;
4. extraction and qualification of the evaluated features;
5. implementation of a database;
6. development of a model in order to predict outcomes.

The following figure shows the use of radiomics in decision support.

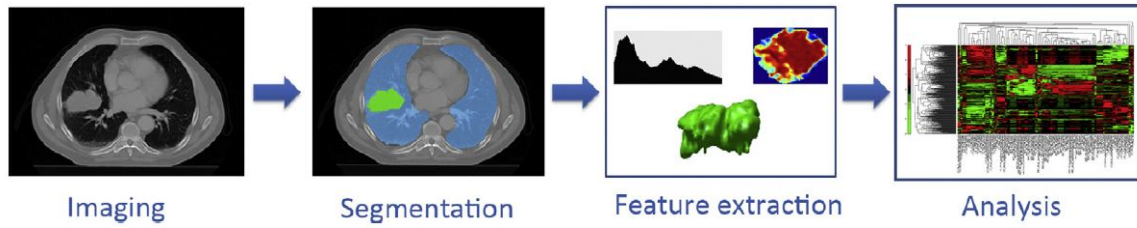


Fig. 4.1: Radiomics process [33]

The use of coupling of non-invasive medical images such that a *single photon emission computed tomography* with a *computed tomography* (SPECT-CT), is frequently used to evaluate tumor and anatomical tissue properties in high resolution.

Following the acquisition of high-quality tomographic images, the identification of the volume of interest, where the tumor or a suspected entity should be, is the *core* of the procedure. The *segmentation* represents the most critical step since all the feature data are generated from the segmented volumes and many tumors have not clearly defined borders. The quantitative image features extracted using advanced mathematical algorithms are defined into two categories:

1. *semantic* features;
2. *agnostic* features.

The first category includes the shape-based features that are focused on location, volume and size of the tumor and they offer information on the phenotype and micro-environment of the tumor. The agnostic features aim instead, to understand the lesion heterogeneity through quantitative descriptors and they are divided into first-, second- and higher order statistical outputs.

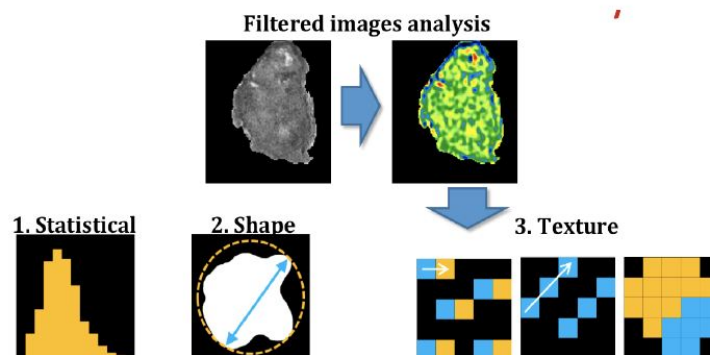


Fig. 4.2: Feature extraction

First-order statistical features are based on the histogram of global-scale radio-tracer uptake intensity distribution. These features reduce the volume of interest to single voxels scale in order to study the asymmetry and flatness of the histogram values, since each medical image is recognized as a gray-scale array. The histogram of an image is the count of how many pixels are characterized by the same gray-level value. These features can be used to quantify phenotypic characters such as tumor density or intensity.

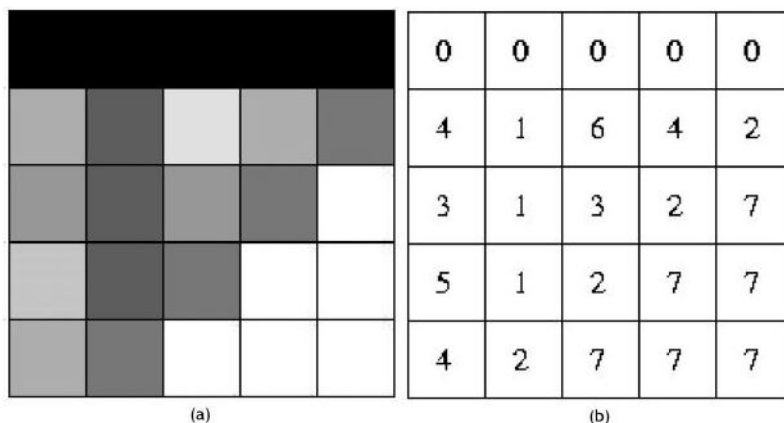


Fig. 4.3: Digital image. (a) Image with 5x5 pixels, with grey-level values in a range from 0 (white) and 7 (black). (b) Numerical representation of the image.

[10]

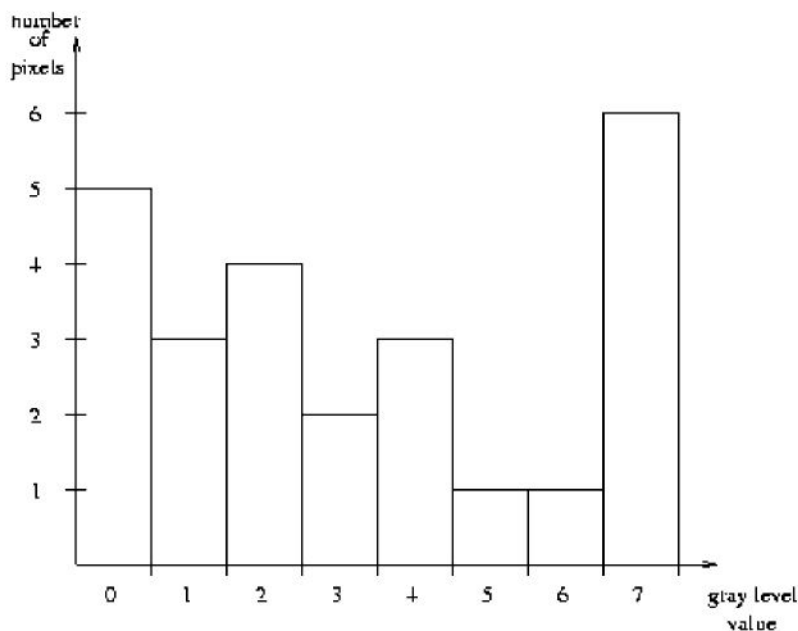


Fig. 4.4: Histogram of the image

[10]

The second order statistical descriptors are also called *texture features*, they are based on grey-tone spatial dependencies, paying attention on the similarity or dissimilarity in terms of contrast between voxels. The concept of *tone* is based on the varying shades of gray of resolution cells in an image, while *texture* is concerned with the spatial distribution of grey tones [27]. This concept is crucial since radiomics has the potential to allow quantitative measurement of intra- and inter-tumoral heterogeneity.

The higher-order statistical methods apply filter grids on the image in order to extract patterns that appear to be repetitive or not.

These features, in conjunction with other information, can be correlated with clinical outcomes data and used for evidence-based clinical decision support process; as a matter of facts this procedure can potentially aid to cancer detection and diagnosis, predict the treatment response and differentiate benign and malignant tumors.

4.1 Texture Analysis methodology: features used

The term *texture* defines the visible quality of an object and it looks at a single element that can be reproduced several times within the object surface.

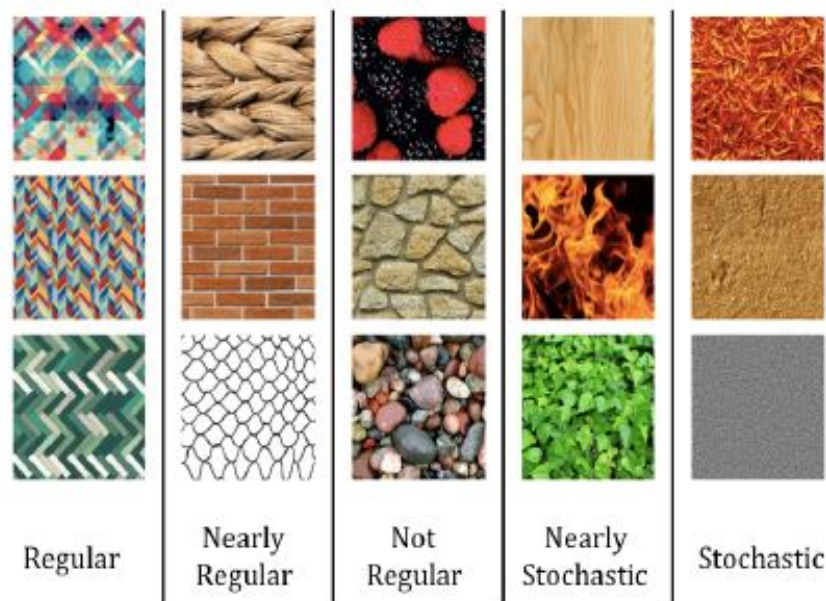


Fig. 4.5: Example of texture

The texture analysis in medical imaging refers to the appearance, structure and arrangement of pixels if the medical image is two-dimensional, or voxels whether it is three-dimensional. It is focused on elements that provide a representative pattern in tumor morphology. The texture analysis is a technique for evaluating the pixels position

and intensity of signal feature such as their gray-level intensity. Texture features involve mathematical parameters computed from pixel distributions which reflect the structure and texture of the image.

The texture analysis methods are categorized as:

- *model-based methods*: they involve sophisticated mathematical models for the estimation of the parameters;
- *statistical approaches* that focus on the relationship between grey-levels of the image: they reach an higher discrimination of the indices with respect to the following two methods;
- *structural methods* that provide a good symbolic description of the image since it is focused on the structure and the border of the object;
- *transform methods* that analyze the texture properties of the image in different frequency or scale space.

In the following table, all feature classes are listed:

Tab. 4.1: Features used

	Features
1st order	Shape Histogram
2nd order	GLCM
higher order	GLRLM GLZLM

The first-order features are divided into two different groups: indices from shape and indices from histogram. As the name suggest the **shape features** describe the shape and size of the volume of interest and they are here listed:

- *sphericity*;
- *compactness*;
- *volume*;

while the **histogram features** indices are connected to the bin size:

- *skewness*, that describes the asymmetry of the gray-level distribution;
- *kurtosis*, that reflects the shape of the gray level distribution, describing how it is peaked or flatted;

- *entropy*, that reflects the randomness of the distribution;
- *energy*, that describes the uniformity of the distribution.

Three main categories of matrices reveal the spatial distribution of the radionuclide uptake computed in a single ROI for each layer of image series and for all the voxels involved and they are used to compute texture features.

The second-order **Gray-level co-occurrence matrix** (GLCM) values take into account the distribution of pairs of pixels to extract textural indices. This matrix is of size $N \times N$, where N is the number of gray levels, is constructed along 13 different directions in a 3-D space. A count of number of pixel pairs that have a given distribution of gray-level values is then carried out. Defining a certain distance x between pixels, the element (0, 10) for instance, corresponds to a number of pixel pairs in the image that have intensity values 0 and 10 respectively and that are separated by a x -pixel distance in a chosen direction. There are many co-occurrence matrices for a single image, one for each distance and direction. Since this matrix reflects the gray-level distribution of pairs of pixels, it is also known as the second-order histogram.

	0	1	2	3	4	5	6	7
0	6	0	0	0	0	0	0	0
1	0	0	1	0	1	0	0	1
2	0	1	0	0	0	1	1	2
3	0	0	0	2	0	0	0	1
4	0	1	0	0	0	0	1	1
5	0	0	1	0	0	0	0	0
6	0	0	1	0	1	0	0	0
7	0	1	2	1	1	0	0	2

Fig. 4.6: Co-occurrence within two-pixels distance in the horizontal direction computed for the image of Figure 4.3

[10]

Using **GLCM** values these following features are extracted:

- *homogeneity*, that is inversely proportional to contrast and energy [45];
- *energy*, that expresses the repetition of pixel pairs of an image;
- *contrast*, that refers to how much difference there is between grey-level values of different objects in the image: higher values indicate large local variations. The image is well contrasted if different areas are clearly visible. [45];
- *entropy*, that is a measure the disorder or randomness of the image, reflecting the complexity within a medical image;
- *dissimilarity*.

The higher-order **Grey-level run length matrix** (GLRLM) values are focused on the spatial distribution of voxel intensities. This is a way of looking at the image across different directions: each element of the matrix represents the size of homogeneous runs of pixels for each gray-level. The matrix has a fixed number of lines corresponding to the number of gray levels and a dynamic number of columns, determined by the size of the largest area. In this sense the matrix counts for each gray-level value, how many times there are two, three, four consecutive pixels with the same value, and so on. Different run-length matrices are calculated along 13 different directions in 3-D.

The **GLRLM** values involves many indices:

- *short-run emphasis* (SRE);
- *long-run emphasis* (LRE);
- *low gray level run emphasis* (LGRE);
- *high gray level run emphasis* (HGRE);
- *run percentage* (RP).

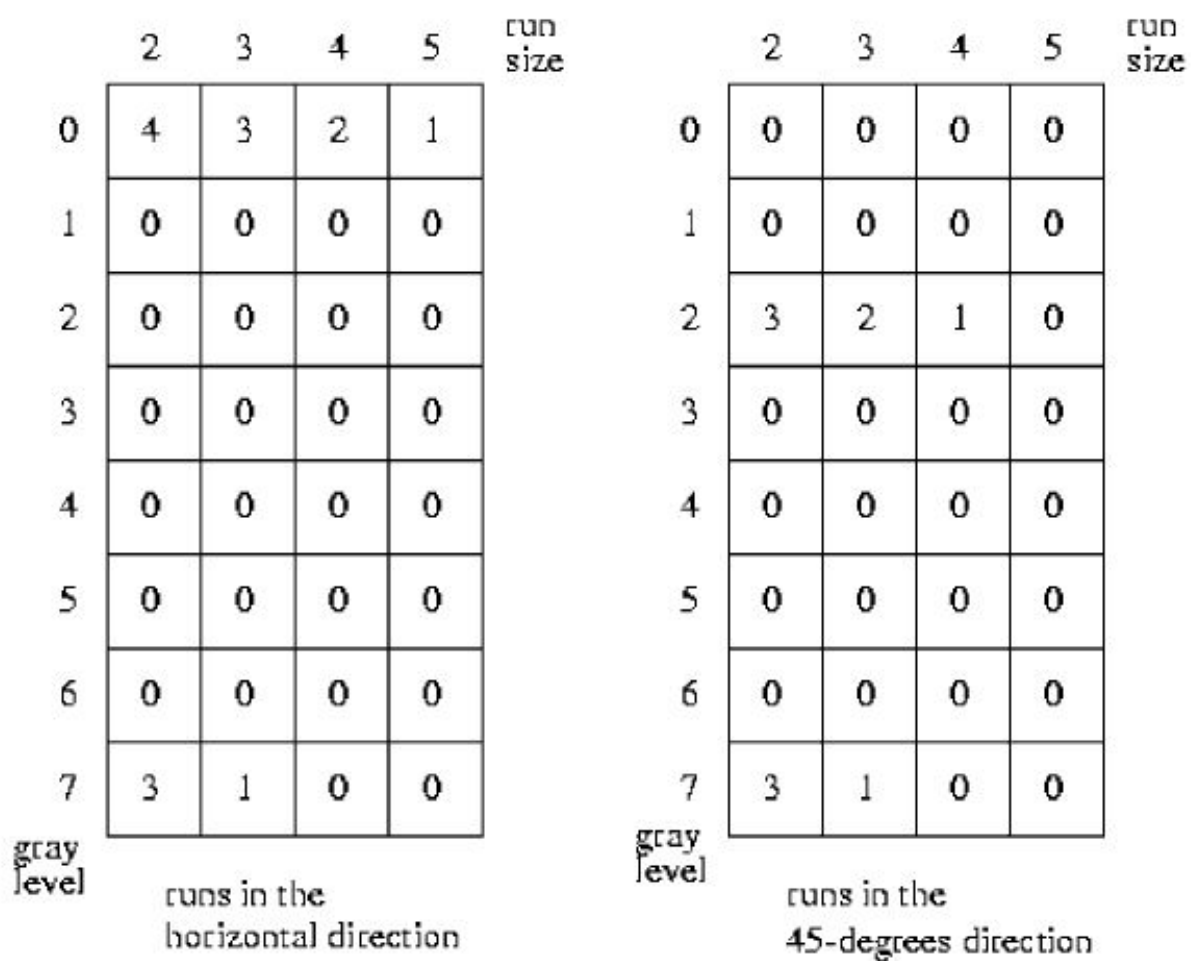


Fig. 4.7: Example of horizontal and diagonal run-length matrices for the image shown in Figure 4.3

[10]

The **Grey-level zone length matrix** (GLZLM) values provide information on the size of homogeneous zones for each gray level in three dimensions.

GLZLM values involves many indices:

- *short-zone emphasis* (SZE);
- *long-zone emphasis* (LZE);
- *low gray level zone emphasis* (LGZE);
- *high gray level zone emphasis* (HGZE);
- *zone percentage* (ZP).

High gray level zone emphasis and low gray level zone emphasis are mostly sensitive to the average uptake rather than to the uptake local heterogeneity [43].

4.2 LifeX software

The identification of volume of interests, the segmentation and the features extraction are carried out with a free software called LifeX.



Fig. 4.8: LifeX icon

Many protocols are implemented in this software: in this thesis study the *Texture* one is selected as shown in Figure 4.9.

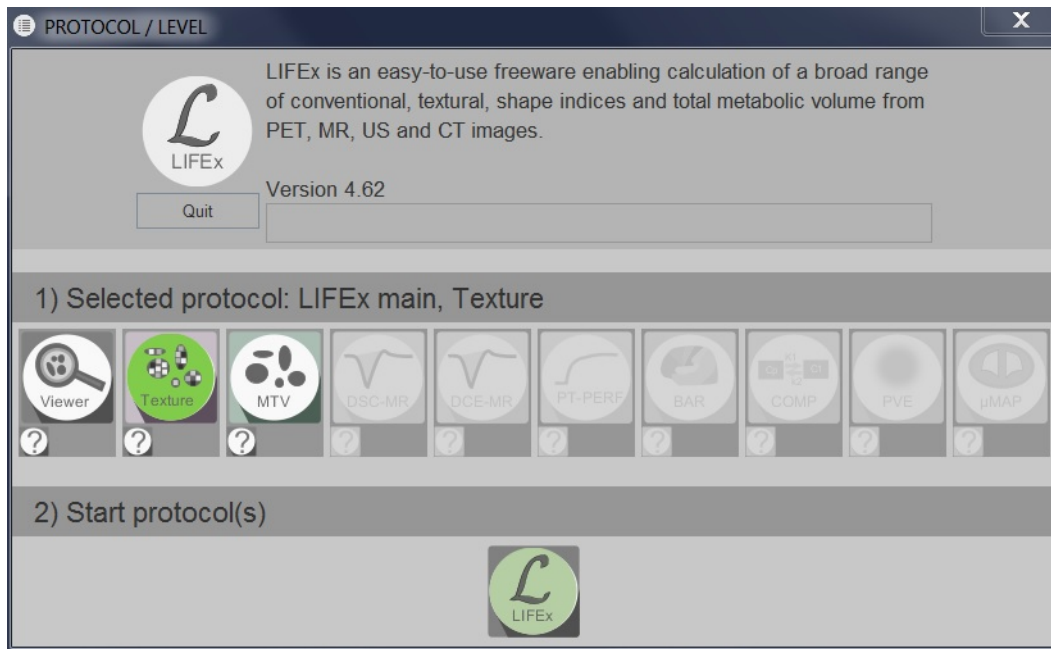


Fig. 4.9: Starter window: 'texture' selection

LifeX user interface software is organized into three sub-parts that require all the following inputs:

- the *spatial resampling* that are set with the dimension (x, y, z) of voxels composing the image, since all the texture index values are sensitive to voxel size [43];
- the *intensity resampling* absolute or relative, providing the minimum and the maximum values inside the region of interest;
- the *intensity discretization* that consists in the number of grey levels used to resample the region of interest (ROI) content, that can typically be 2^n with n in the range from 1 to 7 (suggested to 64 by default) and the width of the bin, that is computed starting from the number of grey levels.

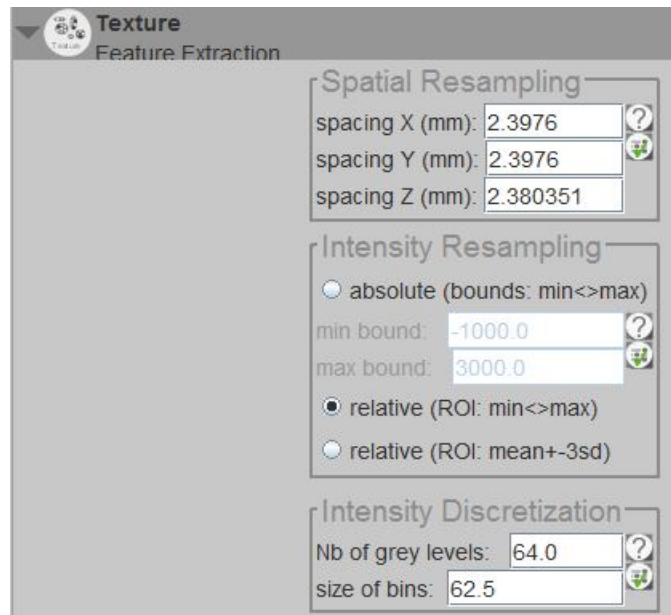


Fig. 4.10: Screenshot reporting the requiring inputs of the software LifeX

The textural indices and conventional parameters computation procedure is described by the following steps:

- reading of the DICOM image for which the indices need to be computed;
- definition of the input parameters;
- drawing the region of interest;
- running the software;
- analyzing the Excel file in which all the resulting parameters are saved and listed.

LifeX software usually works on PET images and it is not designed to SPECT acquisitions. We wrote and tested a Matlab code, reported in Appendix A, in order to use LifeX on SPECT images too.

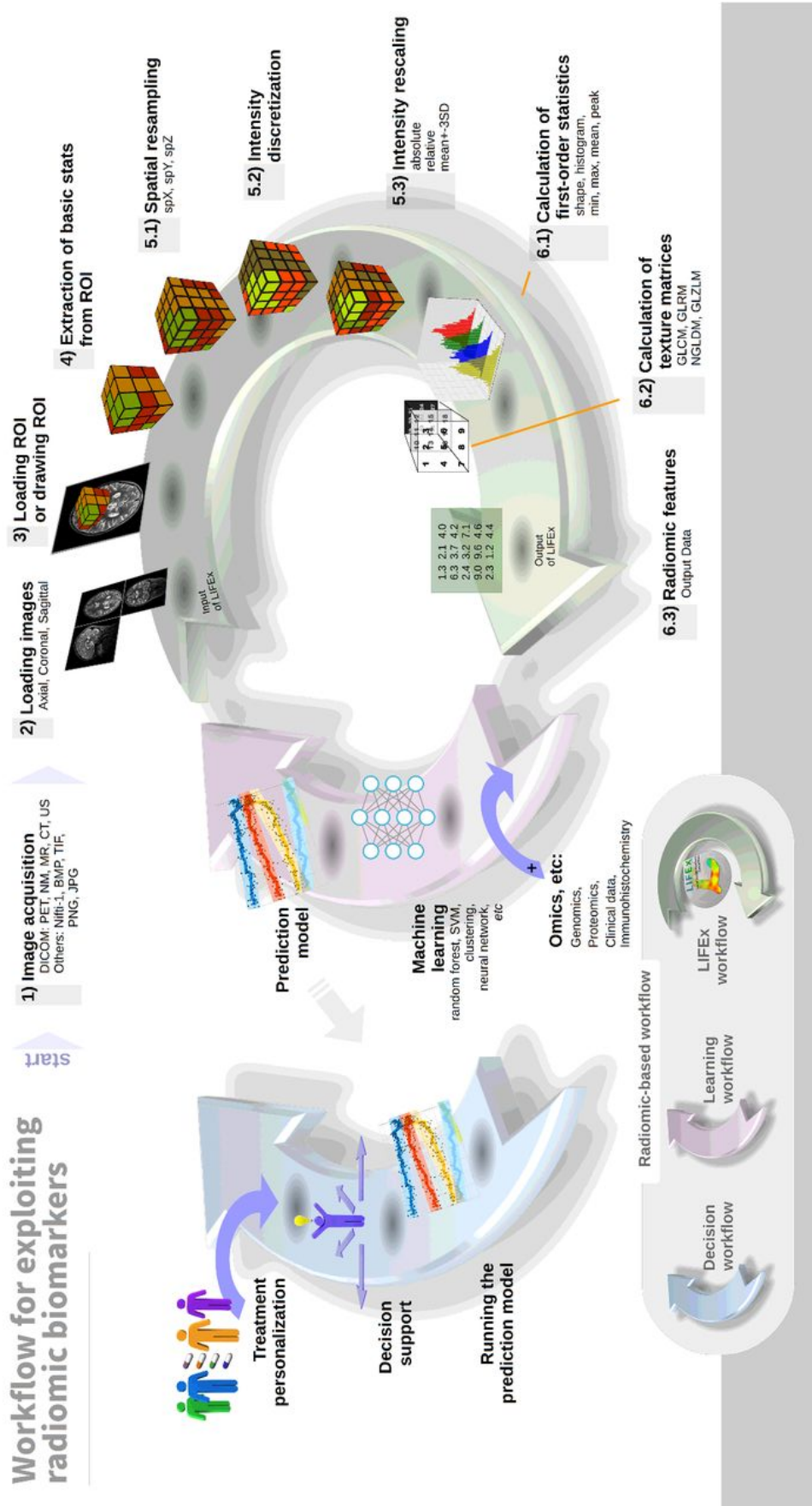


Fig. 4.11: Workflow for exploiting radiomic biomarkers

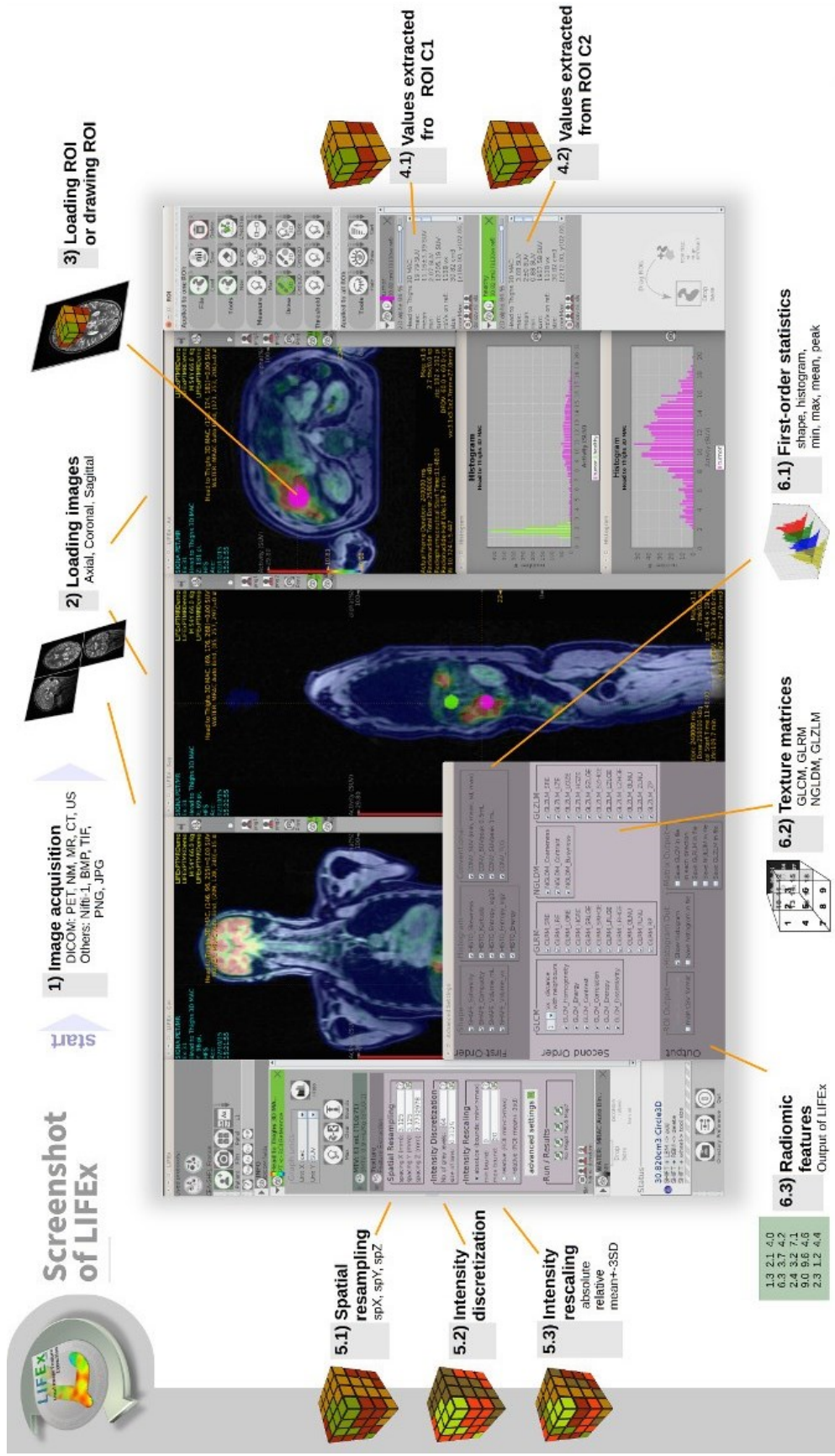


Fig. 4.12: LifeX screenshot

5

Validation of the method through phantom analysis

The analysis procedure developed in this study is first validated on the sphere phantom presented in Paragraph 3.2 in order to understand the significance and the behavior of the feature. First, a discretization analysis is necessary in order to set all the input parameter of the software.

5.1 Discretization analysis of the features

The first analysis is focused on the evaluation of the dependence on discretization (i.e. resampling image intensity values) of the features extracted from digital medical images with LifeX software. The discretization step is necessary to generate occurrence/probability matrices, whose sizes highly impact a computation process. The discretization indices choice affects the quality of the image (e.g. the image noise) and it generates a constant intensity resolution, so that textural features from different patients could be comparable.

Texture features computation is clearly affected by the bin size of the image: using a small bin size (i.e. greater discretization), results tend to be more accurate [55]. Then, the voxel size modification and the intensity discretization, influence the feature reproducibility. Discretization reduces the infinite possible number of intensity values into a finite set and it effectively decreases the image noise [35]. According to this, the range of intensity values of an image needs to be reduced and limited for an efficient radiomic features computation.

Based on cylinder and spheres real volumes, through the software, a 3D segmentation of the volume of interests, based on thresholds, is realized.

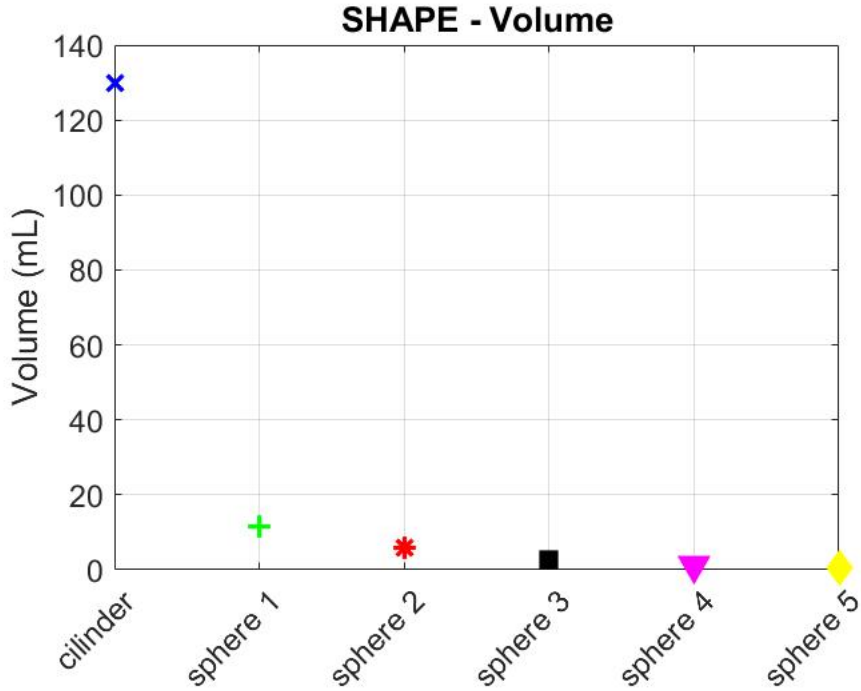


Fig. 5.1: Volume values

First, a wide region of interest which has to include the real volume is defined. Then, for each volume, a certain threshold is selected in order to find the one that is nearer the real volume value. This procedure is the same adopted in patient lesions analysis.

Tab. 5.1: Volumes inside the phantom and thresholds related to

	Volume (cc)	Threshold
Cilinder	130.0	35 %
Sphere #1	11.5	36 %
Sphere #2	5.6	42 %
Sphere #3	2.6	55 %
Sphere #4	1.1	70 %
Sphere #5	0.5	85 %

The software *intensity discretization* input that is computed as 2^n (i.e. 2^n number of bins), is considered varying n in the range from 1 to 7. The data given in output computed at the defined thresholds are analyzed in order to understand how features varies in relation to discretization values.

Shape features (Sphericity, Compacity and Volume) do not show any variation depending on discretization and the same behavior occurs in the Skewness and Kurtosis *Histogram features*.

The Histogram Entropy feature values strongly increase for low values of discretization: a percentage variation is computed in order to show the convergence of values increasing

the discretization, as reported in Figure 5.2.

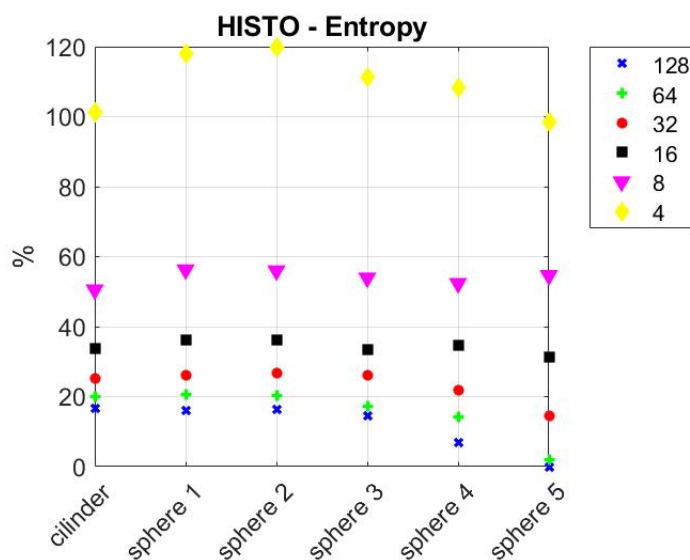


Fig. 5.2: Percentage difference between entropy values coming out from different discretizations

Second and higher order statistical features are not defined for the smallest sphere. Sphere 5, because of its small volume, results to be not valid for the parameters computation through LifeX software. It is possible to assert that volumes smaller than 1.1 are not valid for features evaluation.

GLCM Entropy values, as reported in the following graph, are strongly influenced by the number of discrete values imposed: a convergence is reached increasing the discretization adopted.

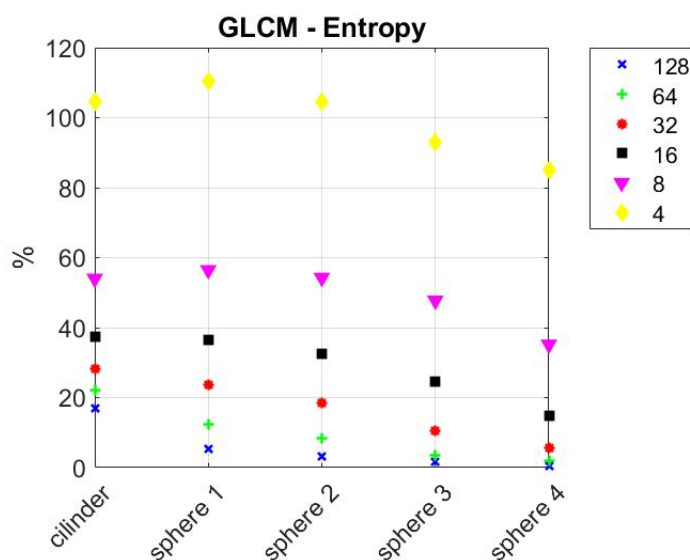


Fig. 5.3: Percentage difference between entropy values coming out from different discretizations

The same convergence trend is reached and shown as follows, for GLRLM SRE, LRE and RP features.

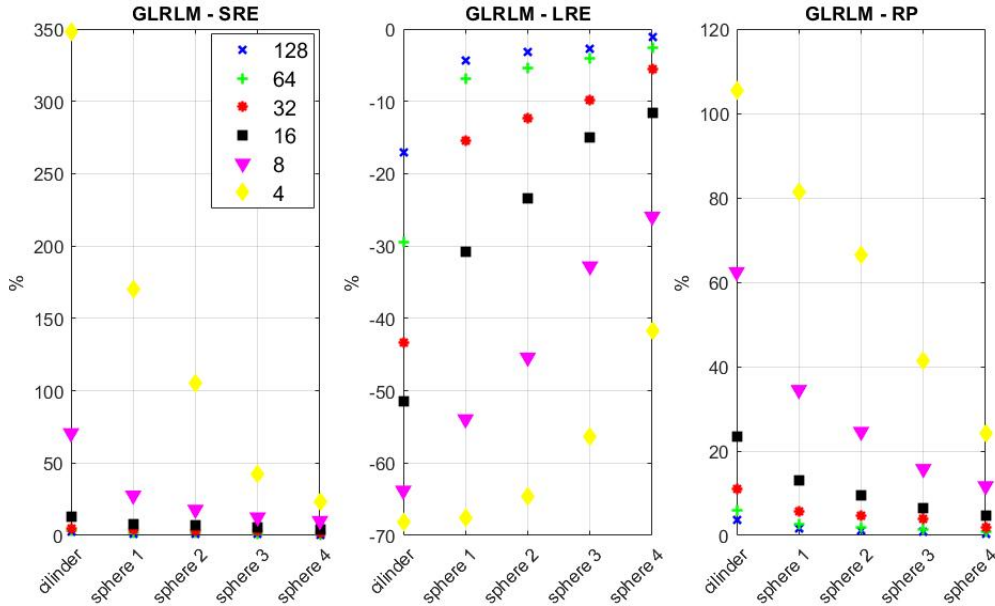


Fig. 5.4: Percentage difference between values coming out from different discretizations

At least $n=5$ (i.e. $2^5 = 32$ discrete values) is required to properly quantify tumor heterogeneity with radiomic features [44]. In addition, resampling values over 64 ($n > 6$), does not provide any additional prognostic information [28]: the discretization analysis consolidates literature data, so that the minimum resampling value for features computation is set to 64. Then, the voxel intensity range is defined starting from the discretization index, into equally spaced bins with a fixed bin width: this strategy is more appropriate for clinical case studies [35].

5.2 Features analysis

Since patients lesions are analyzed through MIRD sphere model, only the spheres are considered and their features computed: the cylinder in this section is not taken into account.

Features analysis is developed computing for each volume of interest, the percentage variation of feature values with respect to the second acquisition according to the procedure adopted for patients. The reason of this procedure will be better explained later.

All volumes considered inside the phantom are guaranteed to be perfectly spherical, so that shape feature Sphericity is expected to be constant. The sphere number 5, the smallest one, does not appear in the following diagrams because the software is not able to compute Shape features in VOIs smaller than a certain value. According to this, it is

possible to understand, looking at values relating to sphere 4, how features computed on small volumes are affected to high variations.

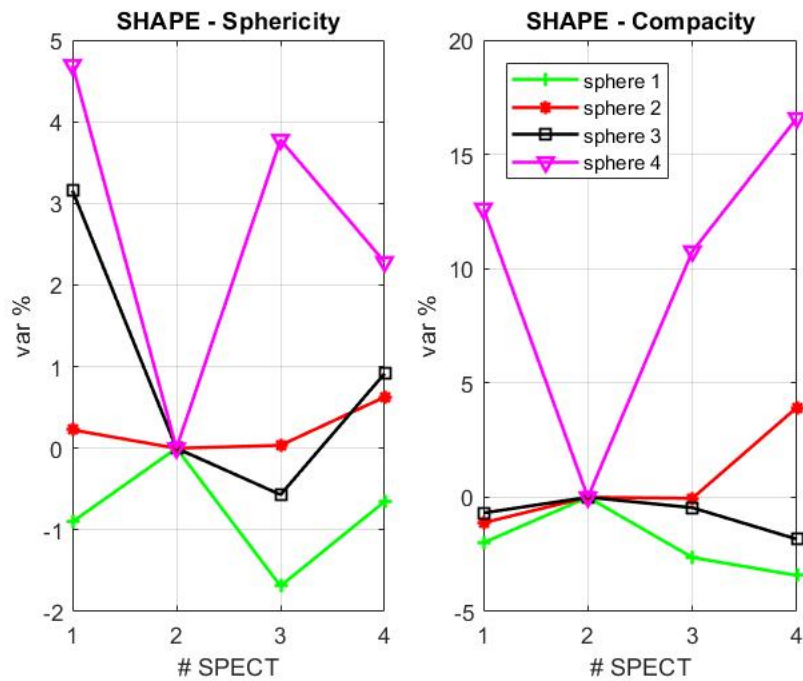


Fig. 5.5: Percentage variation of Sphericity and Compacity values

Since volumes smaller than 2.6 cc, according to our calculation, are not adequate for lesion dosimetry, the sphere 4 can be neglected in the these estimations although is it not excluded from the following diagrams in order to show its huge variation is due to the small volume.

According to Table 5.2 the mean value of sphericity for the sphere phantom is equal to $\mu = 1.123$ with a standard deviation of $\sigma = 3.01\%$. Starting from this estimation, in patients analysis if sphericity value is in the range of $\mu \pm 2\sigma$, the lesion can be considered spherical.

Tab. 5.2: Sphericity values

Spheres	Volume (mL)	Sphericity	Mean value	σ
Sphere #1	11.5	1.084	1.085	0.008
		1.094		
		1.076		
		1.087		
Sphere #2	5.6	1.107	1.107	0.003
		1.105		
		1.105		
		1.112		
Sphere #3	2.6	1.160	1.135	0.018
		1.125		
		1.118		
		1.135		

The second class features are analyzed: similarly, the smallest sphere is included in the graph to emphasize its anomalous trend. Figure 5.6 and Figure 5.7 show the percentage variation of all four acquisition values, except for the smallest spheres, the trends seem to be constant: Skewness and Kurtosis value vary in a range of $\pm 5\%$ and $\pm 2\%$ respectively. Energy and entropy values are in the range of $\pm 1\%$ and $\pm 5\%$.

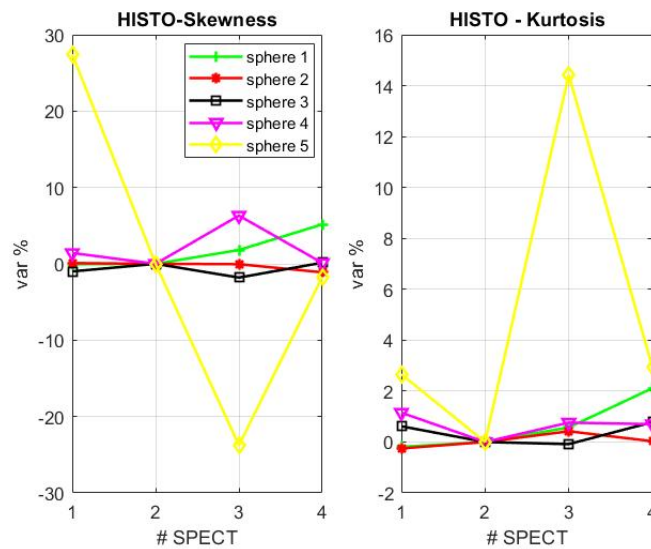


Fig. 5.6: HISTO-Skewness, Kurtosis values

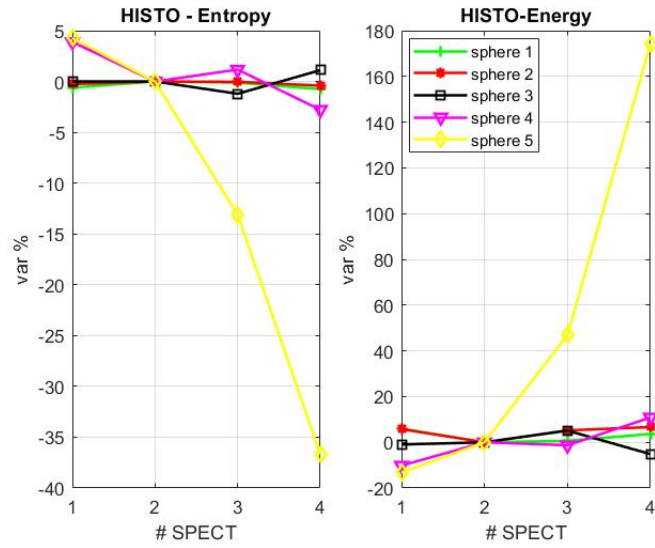


Fig. 5.7: HISTO-Entropy and Energy values

Trends of all volumes suggest that the computation is not reliable for volumes smaller than 1.1 cc.

For higher order features computation, the smallest sphere (the number 5) is not reported in the graphs because it results to be not valid for LifeX software.

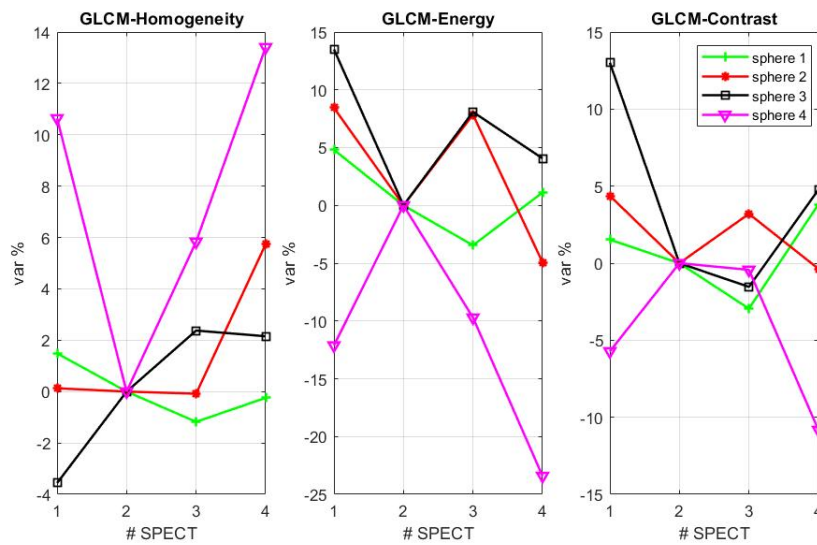


Fig. 5.8: GLCM-Homogeneity, Energy, Contrast values

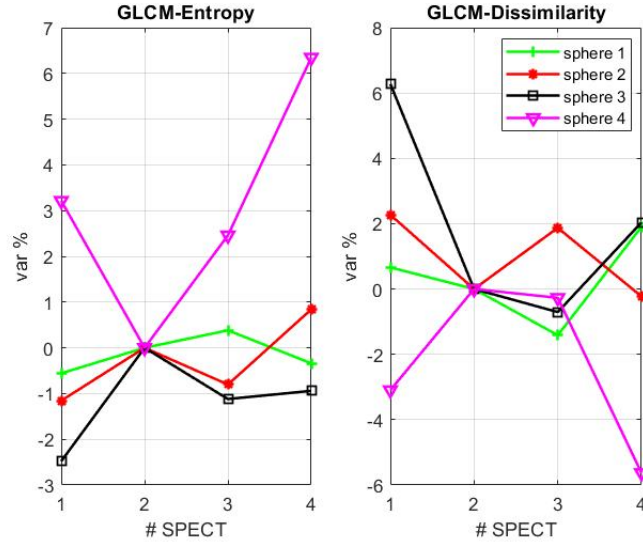


Fig. 5.9: GLCM-Entropy, Dissimilarity values

According to the dosimetric limit, neglecting the sphere 4, it is possible to define the variation range at $\pm 6\%$ for the Homogeneity and, $\pm 15\%$ for Energy and Contrast. Entropy and Dissimilarity show a percentage variation of $\pm 1\%$ and $\pm 6\%$ respectively.

In GLRLM analysis, the sphere 4 shows a similar trend with respect to the other volumes. Even if its volume is under the dosimetric limit, the software has a good response in terms of GLRLM values except for LGRE feature.

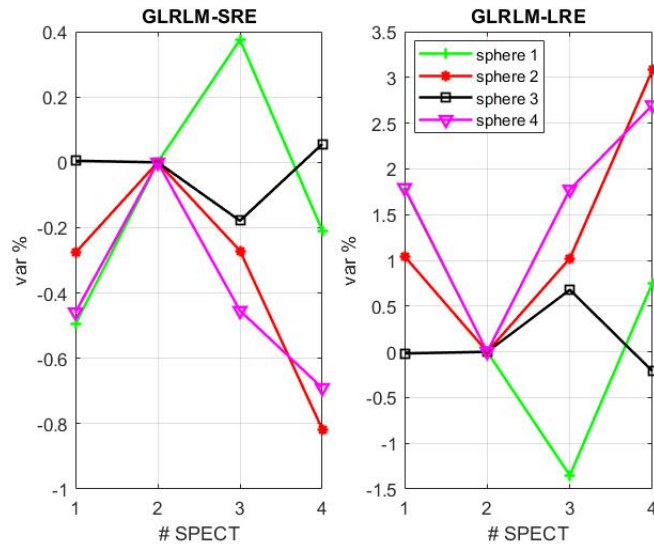


Fig. 5.10: GLRLM-SRE, LRE values

SRE and LRE values vary in a range of $\pm 0.8\%$ and $\pm 3\%$.

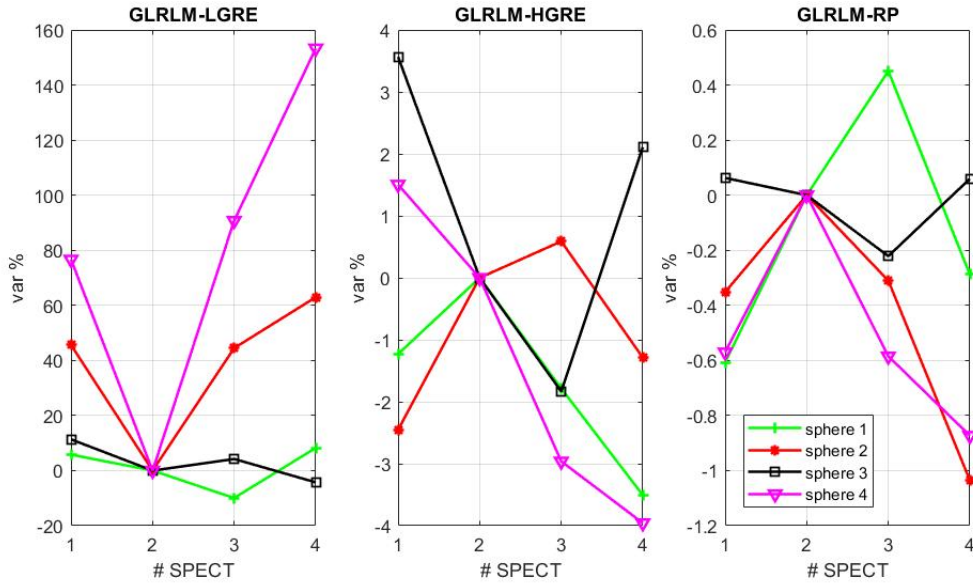


Fig. 5.11: GLRLM-LGRE, HGRE and RP values

LGRE is affected by a huge percentage variation for volumes smaller than 5.6 cc, focusing on sphere 1 and 2 only, values are in the range of $\pm 10\%$, while HGRE and RP vary in a range of $\pm 4\%$ and $\pm 1\%$.

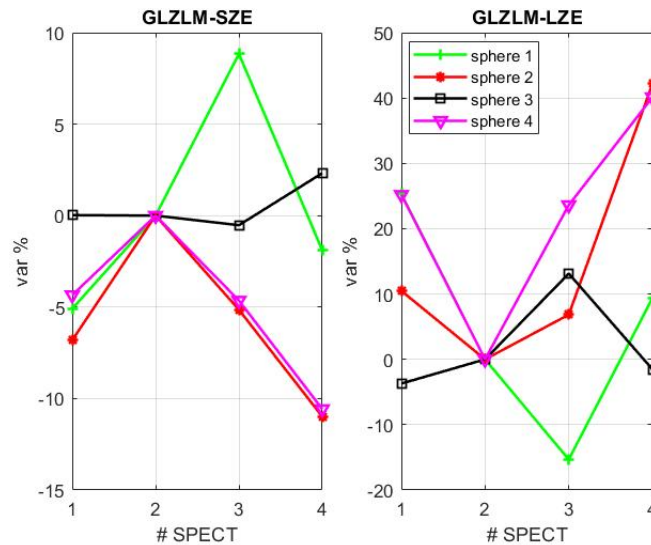


Fig. 5.12: GLZLM-SZE and LZE

These two features have a good result for all four spheres, it is not affected by the small volume of the sphere 4 that is under the dosimetric volume limit.

Similar behavior appears in HGZE and ZP that vary in the range $\pm 14\%$ and $\pm 8\%$ respectively, while LGZE, as in the case of LGRE shows a remarkable dependence on volumes.

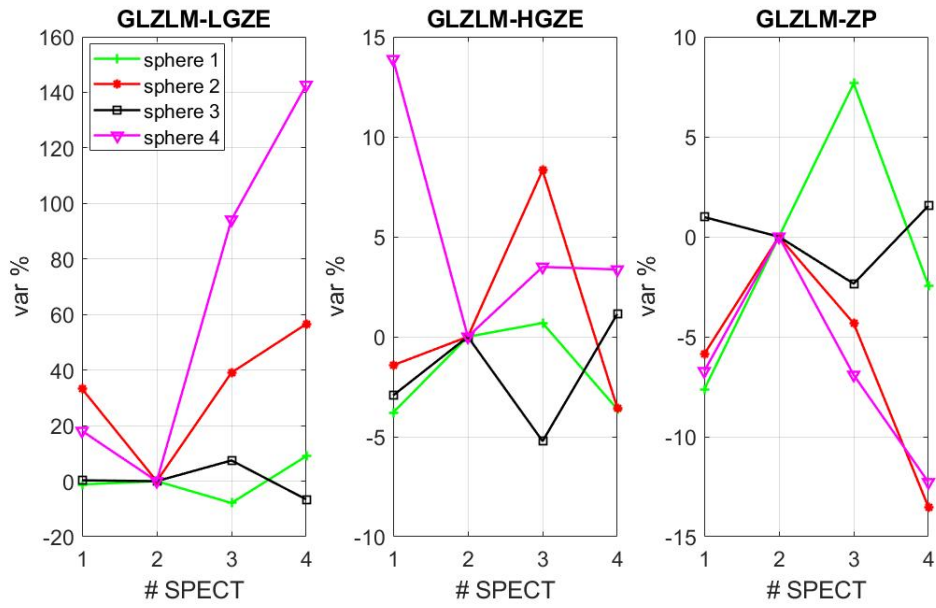


Fig. 5.13: GLZLM-LGZE, HGZE and ZP values

In Table 5.3, all the features values computed are reported.

Tab. 5.3: Features values related to the sphere phantom

	Features	Mean value μ	σ	$\sigma\%$
Shape	Sphericity	1.12	0.033	3 %
	Compacity	1.54	0.43	28 %
Histogram	Skewness	0.62	0.08	13 %
	Kurtosis	2.40	0.13	5 %
	Entropy	1.65	0.07	4 %
	Energy	0.026	0.004	16 %
GLCM	Homogeneity	0.14	0.03	19 %
	Energy	0.005	0.004	82 %
	Contrast	274	142	52 %
	Entropy	2.5	0.4	14 %
	Dissimilarity	13.3	3.5	26 %
GLRLM	SRE	0.99	0.01	0.6 %
	LRE	1.06	0.02	2.3 %
	LGRE	0.06	0.01	18.4 %
	HGRE	770	70	9 %
	RP	0.98	0.01	0.8 %
GLZLM	SZE	0.82	0.07	8.7 %
	LZE	2.2	0.71	32 %
	LGZE	0.06	0.01	20 %
	HGZE	754	92	12 %
	ZP	0.77	0.08	11 %

6

Patients analysis

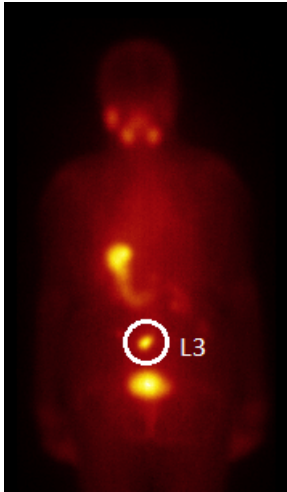
6.1 Dataset

Eight patients affected by metastatic differentiated thyroid carcinoma have been included in our study. The inclusion criteria involve a total thyroidectomy before the Radioiodine treatment.

Tab. 6.1: Dataset

Pt	M/F	Age ¹	PTMN, Typology	Treatment	Activity (MBq)	Data	Lesion type	
				#			Bone	Visceral
#1	F	78	pT1a Nx M1, F ²	I	5566	26/11/18	3	-
#2	F	70	pT2(m)pNx, F	I	5500	25/07/16	1	-
				II	9250	29/05/17	1	-
#3	F	58	-, F	I	3700	19/12/16	7	-
				II	7224	28/06/17	6	-
#4	M	72	-, P ³	I	4449	19/11/18	-	5
#5	F	22	pT1a(m)pN1bpM1, P	I	3700	24/10/16	-	8
				II	9250	29/05/17	-	1
#6	F	66	pT2 N0 cM1, F	I	5550	03/12/18	3	-
#7	F	63	pT3 Nx M1, P	I	5590	13/03/17	5	-
#8	M	54	-, F	I	5595	18/06/18	6	-
				II	7221	17/12/18	5	-

Table 6.1 shows all patients characteristics whose data have been analyzed, six women and two men: their age at diagnosis is in the range between 22 and 78 and they present a maximum of 8 visceral and 7 bone metastases. Radioiodine treatments were performed from July 2016 to December 2018.

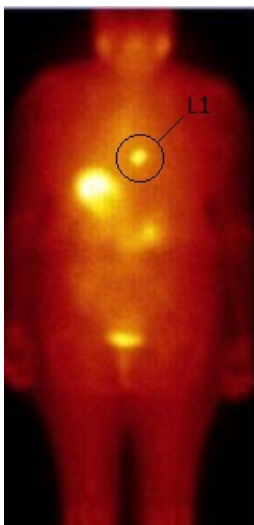


Patient #1

Activity = 5566.0 MBq

Date: 26/11/2018

Lesion #	Volume (cm^3)	Dose (Gy)
L1	17.83	1.54
L2	5.14	7.0
L3	8.63	39.6

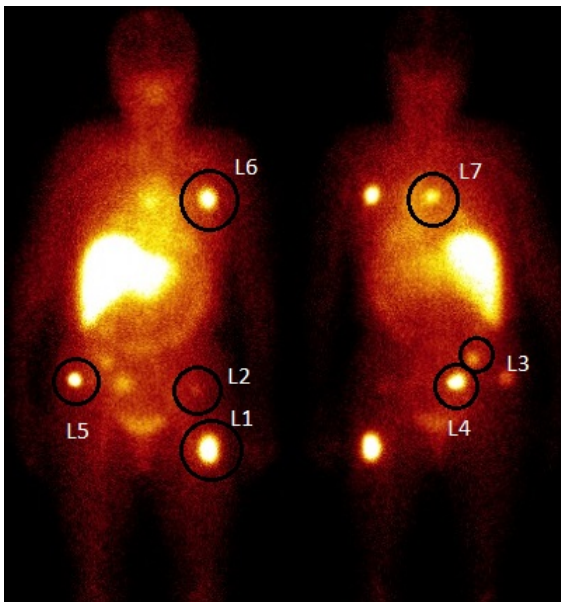


Patient #2

Activity = 9286.6 MBq

Date: 29/05/2017

Lesion #	Volume (cm^3)	Dose (Gy)
L1	27.06	85.43

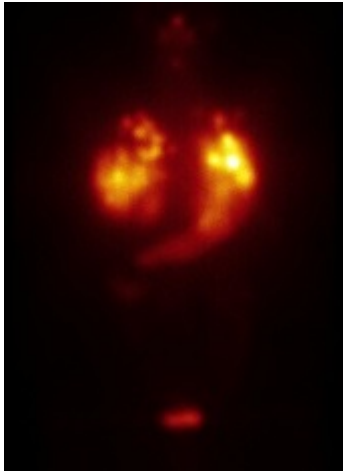


Patient #3

Activity = 3716 MBq

Date: 19/12/2016

Lesion #	Volume (cm^3)	Dose (Gy)
L1	7.79	177.49
L2	5.74	44.65
L3	9.45	81.81
L4	4.27	105.39
L5	4.07	105.25
L6	4.32	337.17
L7	4.82	69.97

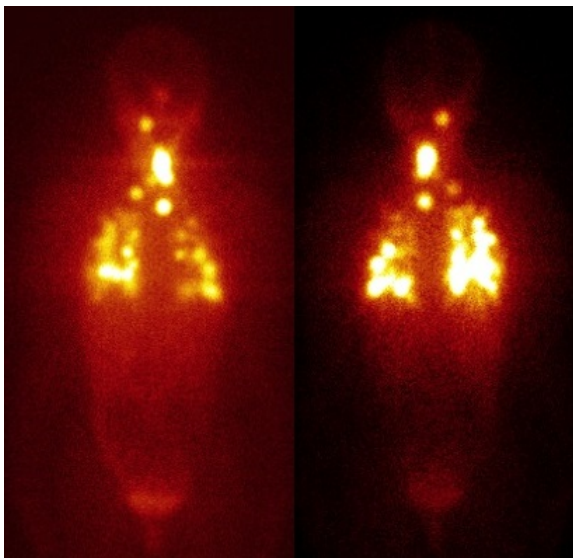


Patient #4

Activity = 4449 MBq

Date: 19/11/2018

Lesion #	Volume (cm^3)	Dose (Gy)
L1	4.73	113.4
L2	11.83	62.35
L3	50.17	137.0
L4	69.04	105.96
L5	3.45	82.93

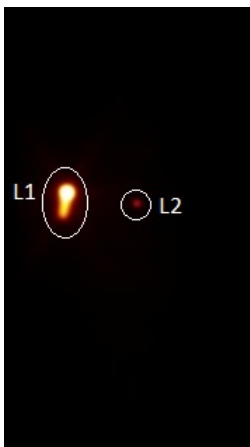


Patient #5

Activity = 5552 MBq

Date: 24/10/2016

Lesion #	Volume (cm^3)	Dose (Gy)
L1	6.17	159.84
L2	7.27	115.27
L3	5.20	56.27
L4	5.55	76.74
L5	18.41	45.47
L6	5.79	81.43
L7	7.82	80.56
L8	7.94	12.68

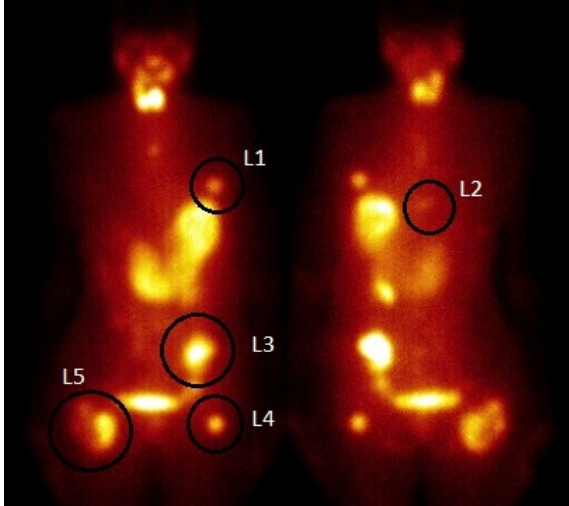


Patient #6

Activity = 5550.0 MBq

Date: 03/12/2018

Lesion #	Volume (cm^3)	Dose (Gy)
L1	25.42	693.6
L2	7.66	81.93
L3	11.19	5.8

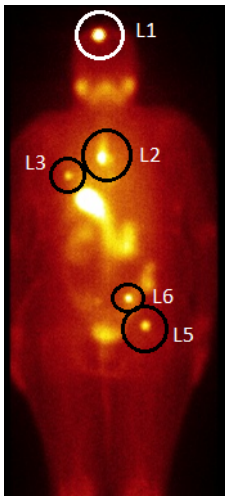


Patient #7

Activity = 5596.0 MBq

Date: 13/03/2017

Lesion #	Volume (cm^3)	Dose (Gy)
L1	5.42	103.0
L2	6.63	26.5
L3	85.33	121.0
L4	11.22	129.8
L5	195.43	40.7



Patient #8

Activity = 7220.8 MBq

Date: 17/12/2018

Lesion #	Volume (cm^3)	Dose (Gy)
L1	9.07	73.7
L2	10.62	13.03
L3	6.25	24.3
L4	6.25	2.7
L5	10.23	18.65
L6	9.88	14.06

6.2 Features extraction

Through LifeX software, all the tomographic images acquired are loaded. A total number of 21 features for each SPECT acquisition are extracted and then analyzed. Considering all the treatments these eight patients were subjected to, a total number of 51 lesions are analyzed, and more than 4000 features values are collected and evaluated.

6.2.1 Shape feature analysis

The first feature extracted and analyzed is the Shape feature called *Sphericity*.

As explained in Paragraph 3.1, since Dose values are computed on the base of the MIRDO method which assumes spheric lesions, the first step of this work has been checking sphericity values of each lesion. In Table 6.2 sphericity values of each metastases are reported and compared with sphere phantom values in order to evaluate if they really can be considered spheric and whether the MIRDO method assumptions constitute a good approximation.

In Paragraph 5.2 the sphere phantom sphericity value is defined as $\mu \pm \sigma$ with $\mu = 1.123$ and $\sigma = 0.030$.

$$\text{Sphericity} = 1.123 \pm 0.030$$

Table 6.2 checks whether lesions sphericity values are included in both $\mu \pm \sigma$ or $\mu \pm 2\sigma$ ranges in order to understand the uncertainty upon which a lesion can be approximated to a sphere or not.

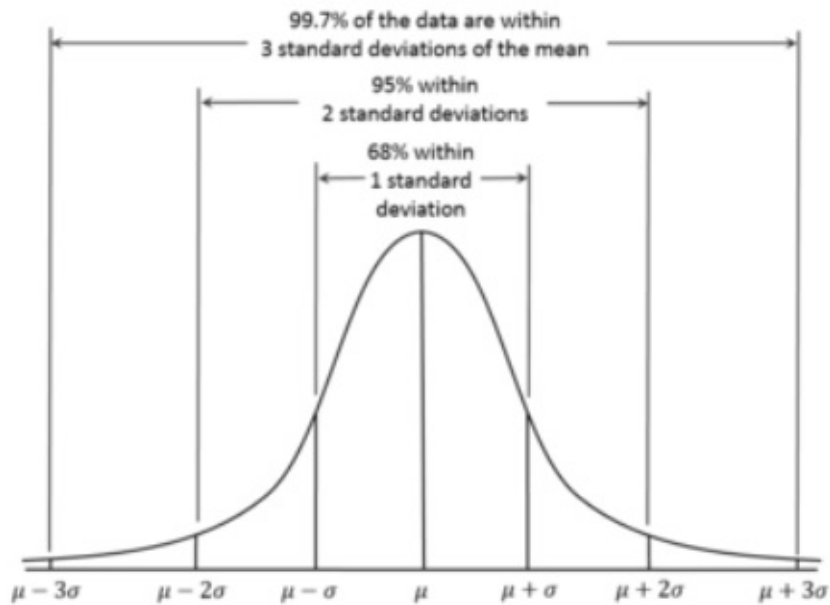


Fig. 6.1: Gaussian Distribution

Tab. 6.2: Sphericity values

Patients	Lesions #	Sphericity		sigma		2 sigma	
		T1	T2	T1	T2	T1	T2
Patient #1	L1	1.059		no		ok	
	L2	1.088		no		ok	
	L3	1.085		no		ok	
Patient #2	L1	1.044	1.030	no	no	no	no
Patient #3	L1	1.061		no		ok	
	L2	1.097		ok		ok	
	L3	1.080		no		ok	
	L4	1.107		ok		ok	
	L5	1.108		ok		ok	
	L6	1.108		ok		ok	
	L7	1.102		ok		ok	
Patient #4	L1	1.077		no		ok	
	L2	1.068		no		ok	
	L3	0.910		no		no	
	L4	0.833		no		no	
	L5	1.104		ok		ok	
Patient #5	L1	1.103		ok		ok	
	L2	1.034		no		no	
	L3	1.051	1.013	no	no	no	no
	L4	1.084		no		ok	
	L5	0.887		no		no	
	L6	1.099		ok		ok	
	L7	1.003		no		no	
	L8	1.049		no		no	
Patient #6 ⁴	L1	1.070		no		ok	
Patient #7	L1	1.106		ok		ok	
	L2	1.082		no		ok	
	L3	0.985		no		no	
	L4	1.082		no		ok	
	L5	0.948		no		no	
Patient #8	L1	1.085	1.058	no	no	ok	ok
	L2	1.034	1.071	no	no	no	ok
	L3	1.087	1.062	no	no	ok	ok
	L4	1.062		no		ok	
	L5	1.088	1.086	no	no	ok	ok
	L6	1.078	1.088	no	no	ok	ok

On 51 lesions, only 9 are included in the range $\mu \pm \sigma$ so that, it is assumed more accurate to consider spheric, lesions whose feature values are included in $\mu \pm 2\sigma$. In this perspective the 60% of analyzed metastases can be assumed spherical and MIRD method can correctly compute the absorption Dose values.

6.3 *Statistical Analysis*

Following data computation and evaluation, it can be interesting to analyze all features values in relation with the clinical treatment response of each metastases. A nuclear medicine specialist, analyzing patients' whole-body planar scintigraphies during the second treatment, has been able to define all lesions responses as follows:

- progressive disease (PD);
- stable disease (SD);
- partial response (PR);
- complete response (CR).

This response is obtained comparing the metastases iodine avidity between first and second treatment acquisitions.

Hence, in this section, only patients subjected to two treatments are taken into account: from our dataset reported in Table 6.1 four patients, who have satisfied this requirement, are included in this analysis.

1. Patient #2;
2. Patient #3 ⁵;
3. Patient #5;
4. Patient #8;

In Figure 6.2 the diagram shows the classification of all lesions into the four response classes.

⁵ Table 6.2 does not report values related to the second treatment because dosimetric analysis has not been done, so that we had no acquisition to perform features analysis

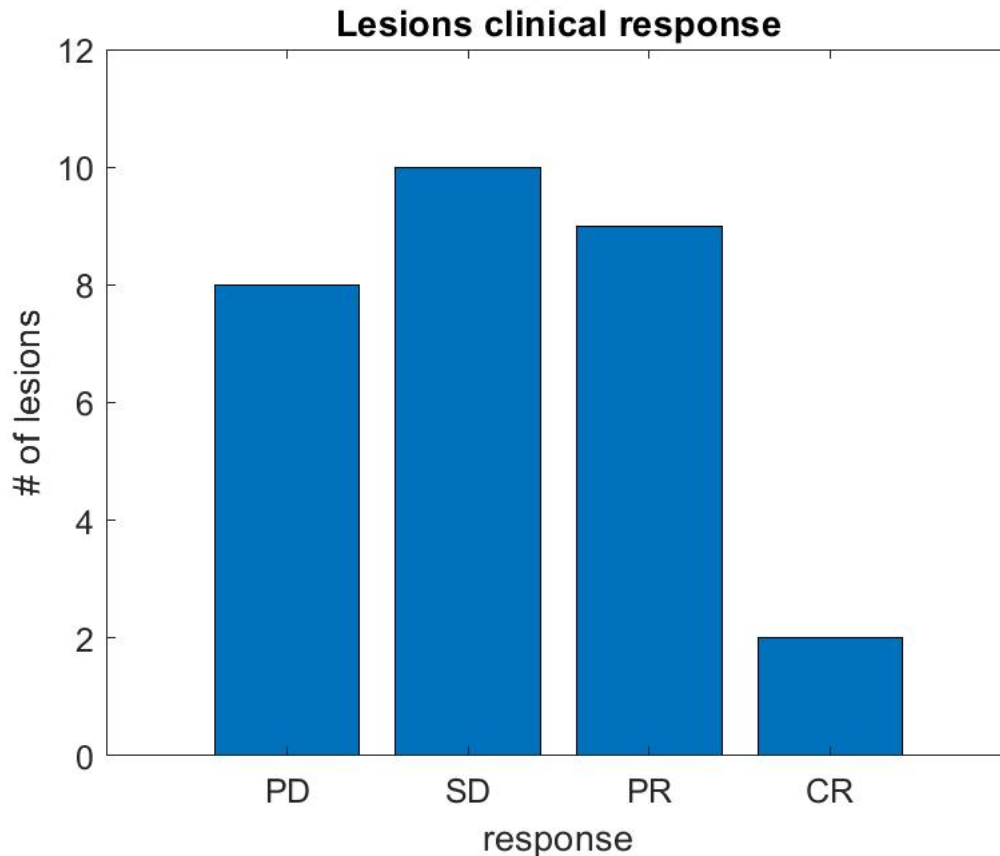


Fig. 6.2: Lesion clinical response

The aim of this statistical analysis is to analyze the 21 features computed on all 29 lesions in relation with their clinical treatment response in order to evaluate their possibly prognostic meaning.

6.3.1 Wilcoxon-Mann-Whitney test and Box-and-whisker Plot

Since we cannot assume that all features extracted from SPECT images are normally distributed, a *Wilcoxon-Mann-Whitney test* is performed. This statistical test, also called *U test*, is performed through MedCalc Statistical Software (*MedCalc Software bvba, Ostend, Belgium; <https://www.medcalc.org>; 2015, version 15.8*) and it is applied in order to evaluate the significance of the difference between two independent populations. *Wilcoxon-Mann-Whitney test* is a *non-parametric* test of the *null hypothesis* defined as a general statement which provides no relationship between two analyzed samples.

The most meaningful parameter which comes out from *Wilcoxon-Mann-Whitney test* is the *p (probability)-value* or *asymptotic significance* which is the probability, for a given statistical model that, assumed the null hypothesis verified, the statistical summary results equal or greater then the actual observed results. The p-value is used in order to quantify

the idea of *statistical significance* of the result: if the obtained value is small ($p < 0.05$) it means that two populations can be considered statistically separated.

All features that resulted to have a significant p-value are graphical represented: box plots are produced in order to show the statistical distribution of features data.

The *box-and-whisker plot* displays a graphical statistical summary of a variable: it is constituted by a central box which represents values from the lower (25%) to the upper (75%) quartile, with a middle line within which represents the median as shown in Figure 6.3.

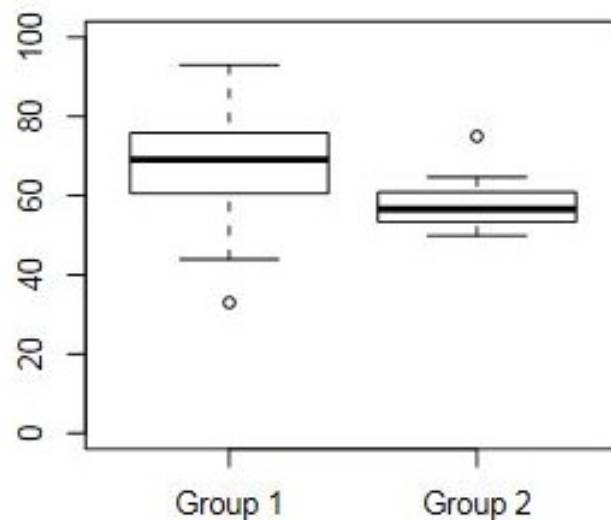


Fig. 6.3: Box Plot example

Since this test is used to analyze two independent populations, in our study, all lesions are distinguished into two groups as a function of their treatment response. Here, the discrimination criteria defined in collaboration with a nuclear medicine specialist:

- not responding, which includes *progressive disease* and *stable disease*;
- responding, which includes *partial response* and *complete response*;

6.3.2 ROC curve analysis

All features are also evaluated using *Receiver Operating Characteristic (ROC) curve analysis* which is also performed by MedCalc Statistical Software. When we compare two samples, one with a disease and the other without, rarely we can observe a perfect separation between them: the distribution of test results is represented in Figure 6.4.

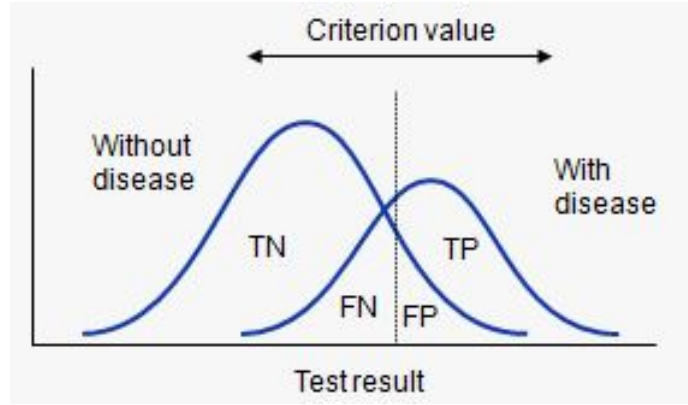


Fig. 6.4: Distribution of the test results

In Figure 6.4 the *criteria value (cut-off)* is represented: it is the threshold value which discriminates the two samples, but, in addition to the group that correctly results to have a positive test outcome (TP=True Positive fraction), it also includes a fraction of population which actually have negative result (FP=False Positive fraction). The same occurs for negative test outcome: there are some cases without disease which are correctly classified (TN=True Negative fraction) with some other cases which actually have a disease (FN=False Negative fraction).

In our study this test is performed in order to discriminate lesions response to treatment: *ROC curve analysis* provides a distinction into the same two classes displayed in Sub-paragraph 6.3.1.

According to this subdivision and the aim of this analysis, in Table 6.3 the meaning of all fractions is represented.

Tab. 6.3: Different fractions (TP, FP, TN, FN) representation

Test	Responding	Response		Total	
		n	Not Responding		n
Positive	True Positive (TP)	a	False Positive (FP)	c	a + c
Negative	False Negative (FN)	b	True Negative (TN)	d	b + d
Total		a + b		c + d	

Two main coefficients are computed and evaluated in this analysis:

- **Sensitivity:** the probability which provides the test result positive and the lesion classified as 'Responding'

$$Sensitivity = \frac{a}{a + b};$$

- **Specificity:** the probability which provides the test result negative when lesions

are classified as 'Not Responding'

$$Specificity = \frac{d}{c + d}$$

ROC curves show *Sensitivity* as a function of *Specificity* and they are computed for different cut-off points. A test with a very good discrimination has a *ROC curve* that passes very close to the upper left corner which corresponds to the highest test accuracy as shown in Figure 6.5.

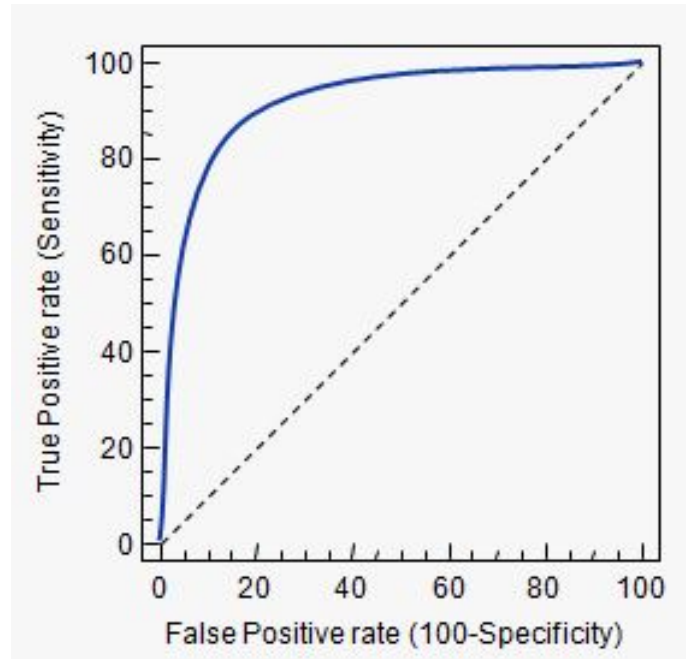


Fig. 6.5: Example of the perfect discrimination test ROC curve

In addition to *Sensitivity* and *Specificity*, MedCalc software gives as output also a value related to the *Area Under the Curve (AUC value)*. The physical meaning of this value is here explained: an *AUC value*, for instance, equal to 0.8, means that, if we select randomly a case from the positive group, it will have a test value larger than the 80% of the negative group [63]. An *AUC value* equal to 0.5 means that there is no difference between the two distributions. To have a perfect separation we want the area under the ROC curve equal to 1.

All ROC curves which are shown in Chapter 7 are related to the maximum *AUC value* obtainable.

7

Results

Wilcoxon-Mann-Whitney test and *ROC curves analysis* were performed on 21 features computed for all 29 lesions of patients which were included in the statistical analysis: a total number of 609 data were collected and the analysis was performed.

Both analysis were carried out through two different collection data approaches:

1. computation of features absolute values recorded at the second acquisition time which is assumed to be the most meaningful;
2. computation of features percentage variation between the last acquisition and the second one.

7.1 *Statistical analysis results: first approach*

First, *Wilcoxon-Mann-Whitney test* was performed and then *Box Plots* were produced. 21 p-values, one for each feature, were evaluated: if we consider statistically acceptable p-values smaller than 0.05, the best statistical result is the one related to the GLZLM feature *HGZE* (p-value = 0.034). Generally, in medical field, a p-value < 0.1 can be also considered statistically relevant: in this perspective also HISTO features called *Skewness*, *Kurtosis*, *Entropy* and GLRLM feature *HGRE* could be taken into account. Results are displayed through box plots and reported in Figures 7.1 and 7.2.

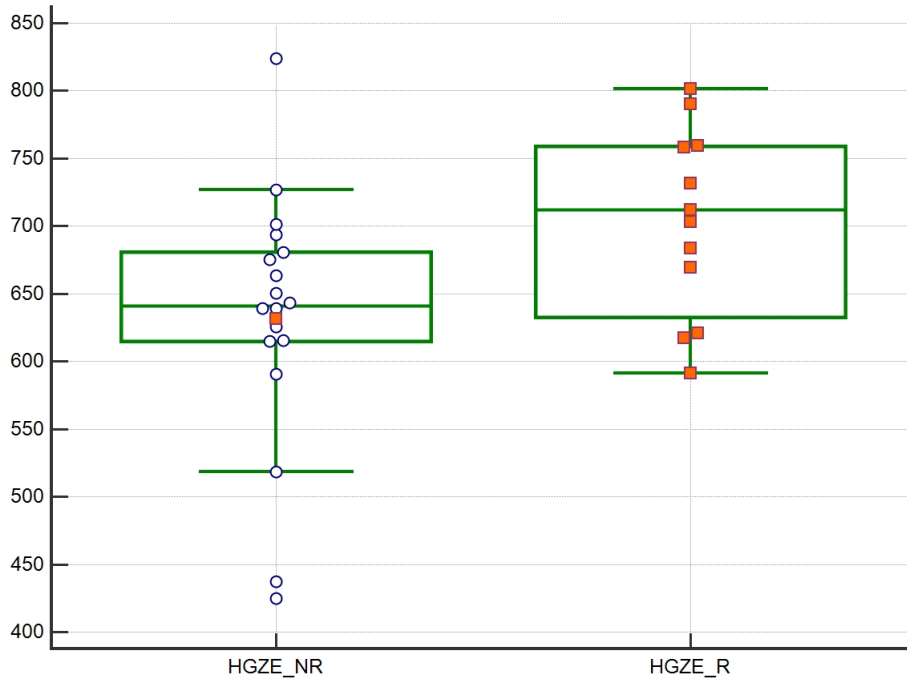


Fig. 7.1: Box Plot GLZLM-HGZE

Figure 7.1 represents the feature values distribution of the two samples (NR-R): responding median value is much higher than the not responding 75 percentile and these two distributions can be considered distinct.

Figure 7.2 displays box plots related to *Skewness*, *Kurtosis* and *Entropy* features, where this distinction seems to be less pronounced ($0.05 < p < 0.10$).

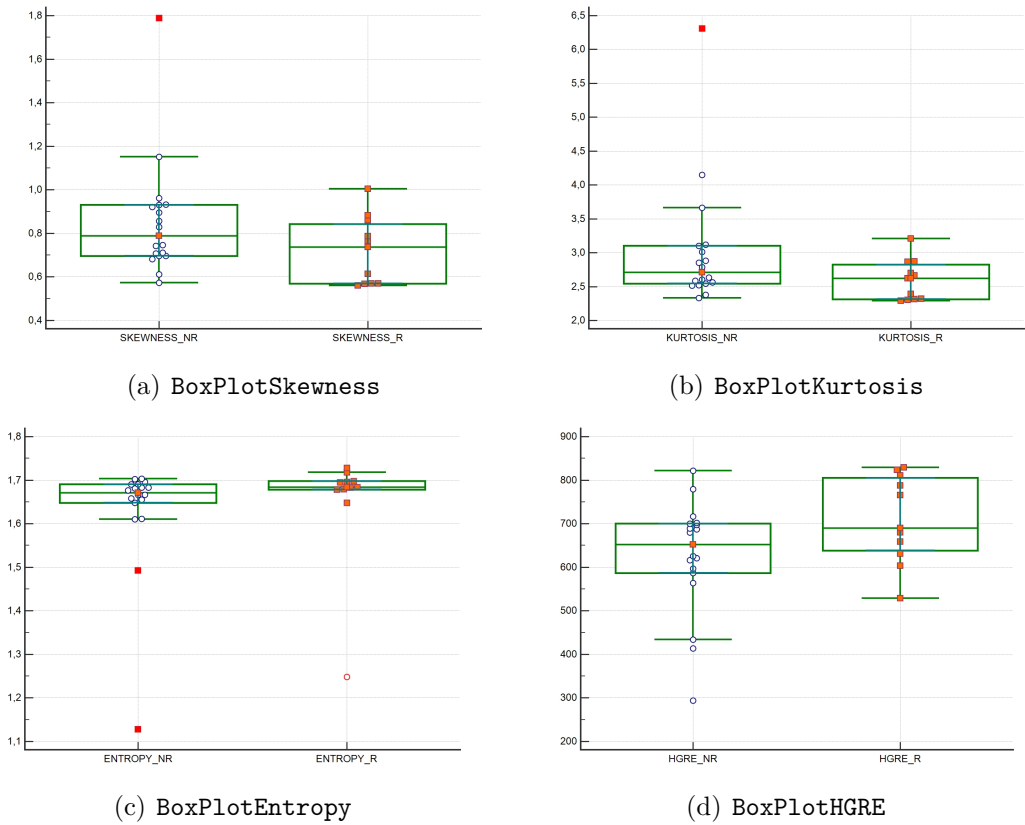


Fig. 7.2: Box Plots

Then, *ROC curves analysis* is performed: 21 *ROC curves*, one for each feature, were plotted and the corresponding 42 *Sensitivity* and *Specificity* values were evaluated.

First, we focused on *Specificity* values: we noticed that, Histo features *Skewness* and *Kurtosis* are characterized by a 100% *Specificity* and 36.4% *Sensitivity*; plots are reported in Figure 7.3.

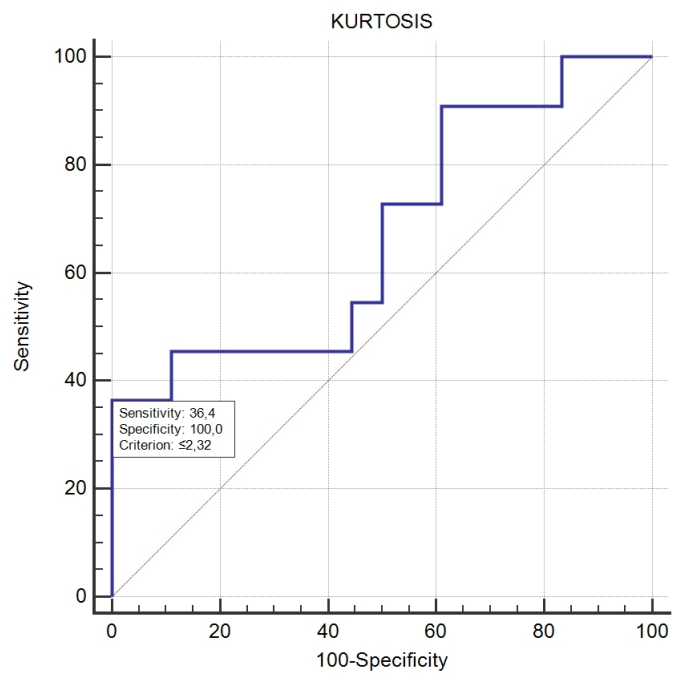
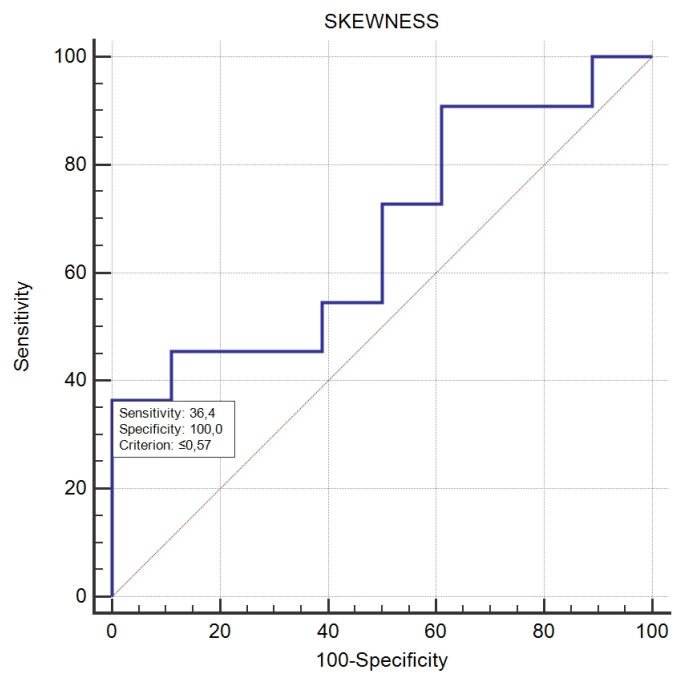


Fig. 7.3: HISTO Skewness, Kurtosis ROC curves

Using *Skewness* value to predict treatment response is therefore possible: if the *Skewness* value related to a lesion is found ≤ 0.57 we can suggest that the lesion will positively respond to the treatment. However, a *Sensitivity* of 36.4% means that only one third of the responding lesions will be detected by this criterion. The same conclusions are drawn for *Kurtosis*, with an associated criterion ≤ 2.32 . Then, looking at these values, we can suggest that, lesions with *Skewness and Kurtosis* values which respect their criterion, can be classified as responding and probably will not need a second radioiodine treatment.

Focusing on *AUC values*, the highest result is the one obtained with to GLZLM feature *HGZE* ($AUC=0.72$), even though it does not show high *Specificity* and *Sensibility* values as shown in Figure 7.4. If *HGZE* values >701.2 half of the responding lesions are detected, but in addition it encloses also 11% of the not responding ones.

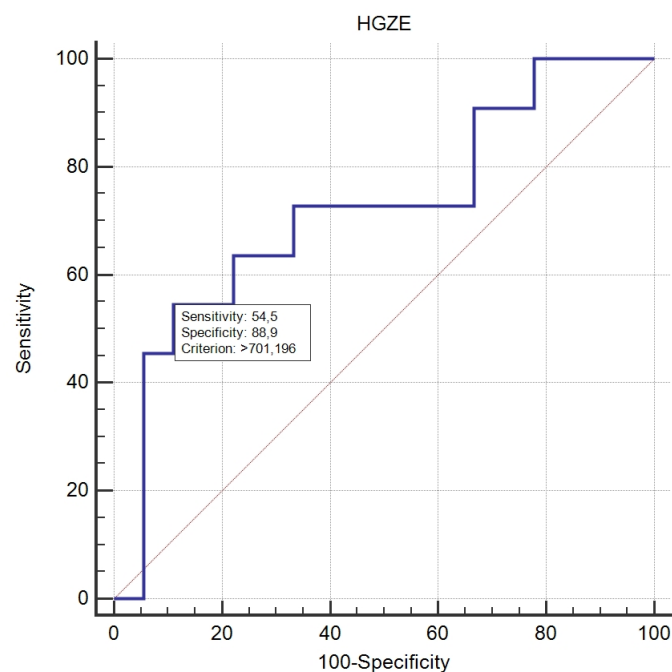


Fig. 7.4: HGZE ROC curve

ROC curves related to other features evaluated, are shown in Appendix D: they show a *Specificity* not so high; a large *Sensitivity* value means that, the associated criterion includes a large number of responding lesions, but, if the *Specificity* is not 100% in addition, also some non responding lesions are counted.

According to these analysis we can assert that results obtained are consistent. The *U test* results have been confirmed with ROC curves analysis.

7.2 Statistical analysis results: second approach

The second analysis approach provides the computation of the percentage variation between the fourth and the second acquisitions feature values.

Wilcoxon-Mann-Whitney test was performed: among all 21 p-values evaluated, the one related to *Histo Skewness* resulted to be acceptable ($p < 10\%$). Figure 7.5 displays *Histo Skewness* box plot: the responding median value is higher than the not responding 75 percentile which makes a relevant separation between two samples. All the other box plots are reported in Appendix E.

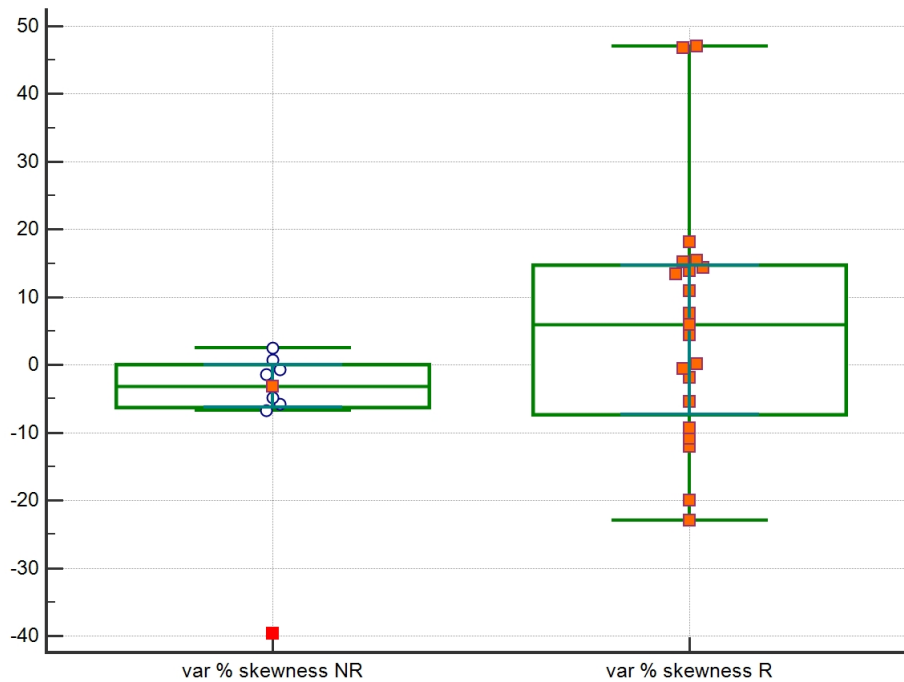


Fig. 7.5: Box Plot HISTO Skewness

With the same procedure previously adopted, also ROC curves analysis was performed on all features. Looking at *Specificity* values, *Contrast and Dissimilarity* features resulted to be significant: due to these features evaluations, we can be able to immediately recognize lesions which are characterized by a good treatment response. Figure 7.6 shows the relative ROC curves: both *Contrast* and *Dissimilarity* were defined by a 36.4 % *Sensitivity* and 100% *Specificity*. According to these results, *Contrast* and *Dissimilarity* features are able to detect one third of responding lesions without considering any case which have no good treatment response. When features trends are evaluated and the percentage variation between the last and the second acquisition is computed, if the lesion is defined by a variation of *Contrast* $\leq -8.1\%$ or a *Dissimilarity* $\leq -3.8\%$ it can be classified as responding and it will not need further treatments.

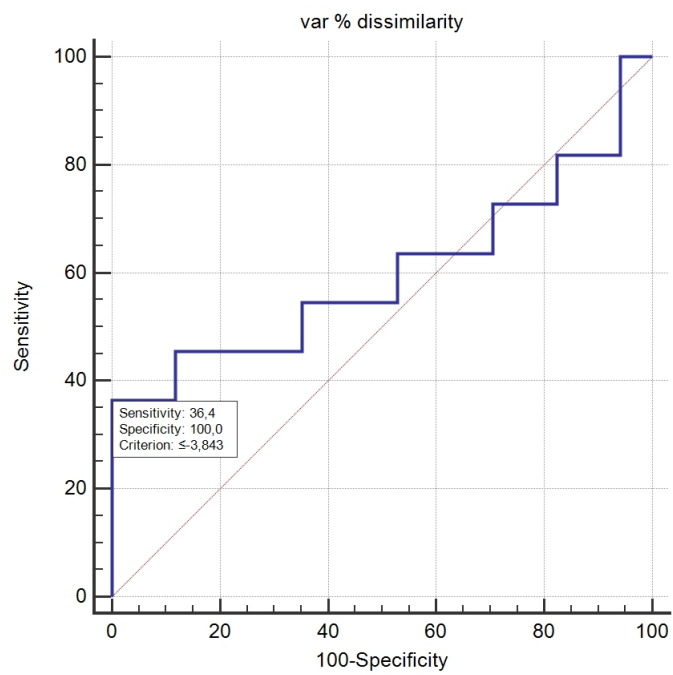
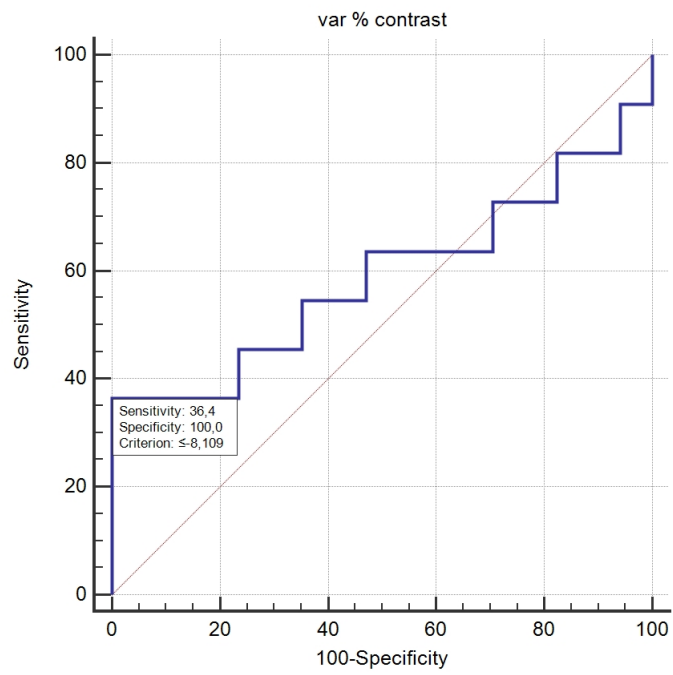


Fig. 7.6: Contrast and Dissimilarity ROC curves

The same evaluation was drawn in GLRLM *HGRE* feature whose *Sensitivity* and *Specificity* values are 45.5% and 100% respectively. If the percentage variation of HGRE values results to be $\leq -8.2\%$, almost half responding lesions are counted and all not responding ones are excluded. HGRE relative ROC curve is shown in Figure 7.7.

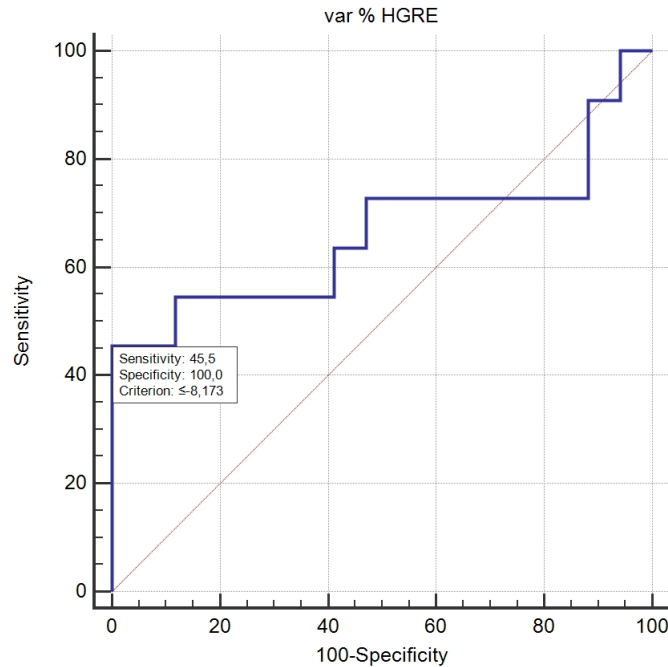


Fig. 7.7: GLRLM HGRE ROC curves

7.3 Statistical analysis results: mean absorbed Dose

Statistical analysis was also performed on the mean lesion absorbed Dose values. Each lesion is characterized by a single Dose value which is computed through MIRD method defined in Paragraph 3.1.

Wilcoxon-Mann-Whitney test did not give as output a statistical significance since p-value resulted to be much higher than 0.05 and the relative box plot is reported in Figure 7.8. Dose box plot is consistent with *Wilcoxon-Mann-Whitney test*: the non significant p-value is also reflected in a not distinct samples.

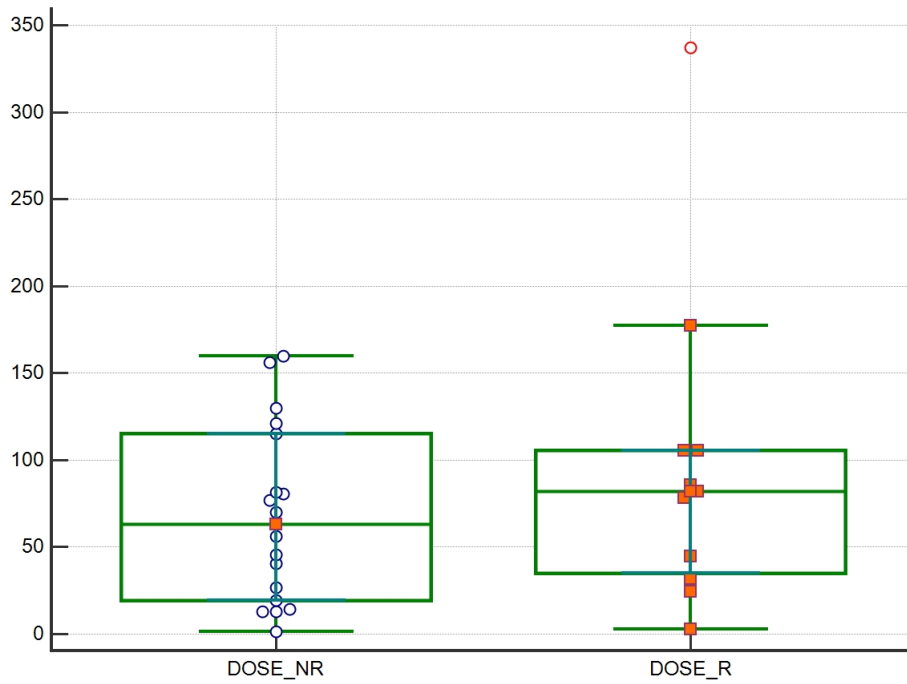


Fig. 7.8: Lesion absorbed Dose box plot

Then, the *ROC curve analysis* was performed and the relative plot is displayed in Figure 7.9.

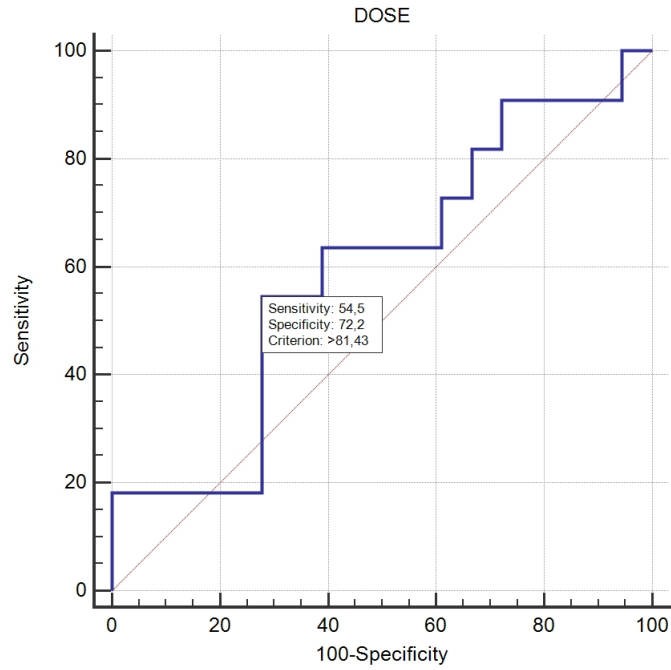


Fig. 7.9: Lesion absorbed Dose ROC curve

The relative *AUC* value results to be equal to 0.60; the *Sensitivity* and *Specificity* are 54.5% and 72.2% respectively. The absorbed Dose associated criterion which discriminates the two samples in terms of treatment response is about 81 Gy.

Conclusions

This thesis work has been developed on patients affected by a metastatic differentiated thyroid carcinoma (MDTC). These patients are treated with radioiodine (^{131}I): the administered activity is usually empirically fixed, but, this approach does not provide an optimization and a personalization of the therapeutic plan since it does not take into account patient-related activity distribution. A dosimetric protocol has been adopted at A.O. Ordine Mauriziano Umberto I Hospital [*Dosimetria durante terapia di carcinoma differenziato della tiroide metastatico - Protocollo dosimetrico*] to evaluate patient specific radioiodine distribution and absorbed dose to organs (target and organs at risk). Moreover, lesion dosimetry is useful to determine the maximum tolerable activity, which is the maximum activity value to be delivered to the patient keeping risk of side effects acceptable. According to the MIRD method, a standard regulation for internal dosimetry, the mean absorbed dose values have been computed. It assumes an uniform radioactive concentration of the radionuclide within organs suggesting that, the estimation of the mean absorbed dose can be predictive of biological effects. One of the purposes of dosimetric analysis has been the estimation of the dose delivered to each metastases and the evaluation of their therapeutic response.

All MDTC patients treated with ^{131}I at A.O. Mauriziano Hospital follow a dosimetric protocol: four SPECT/CT acquisitions are acquired 4, 24, 48, 96 hours after radionuclide administration (activity: 3.7-11.2 GBq); lesions are contoured by a nuclear medicine physician and doses are evaluated according to MIRD method.

Aim of this thesis work has been to test the feasibility of texture analysis and features evaluation performed on the four SPECT images acquired following the dosimetric protocol. In order to fulfill this aim, the local image feature extraction software LifeX has been used. The first issue we met has been the LifeX software management since it works on PET images and it is not designed to SPECT acquisitions. A Matlab code, reported in Appendix A, has been written and tested in order to use LifeX on SPECT images too.

A preliminary study has been performed on a NEMA PET-CT sphere phantom in order to test and evaluate the feasibility of this analysis approach. First, a discretization analysis have been performed, and resampling with 64 bins has been confirmed to be the best one to use, as reported in literature [28]. Phantom features extraction has shown that, volumes smaller than 1.1 cc, cannot be examined with the proposed features evaluation. Then, features analysis has been performed in order to understand the variation range under which features can be considered constant. This analysis has been conducted on the Shape feature Sphericity, since, obviously, all spheres contained in the phantom are spherical: the range was evaluated as standard deviation of the outcome and it has been resulted to be 3%.

Then, the presented procedure has been applied on all patients included in this thesis work. Treatment responses (whether patients are responding or not to therapy) of each lesion have been evaluated by a nuclear medicine specialist.

Texture analysis and features evaluation have been performed on the four SPECT images acquired following the dosimetric protocol. 21 features have been evaluated on all four acquisitions of 8 patients, considering a total number of 51 lesion which have produced 34272 data, however, since statistical analysis was due only on patients treated at least twice, our dataset has been still reduced to 4 patients for a total number of 29 lesions which have produced a data collection of 9744 values.

A statistical analysis has been developed on two datasets: first, considering the features values computed at the second acquisition time, second, the percentage variation of features values between the forth and the second acquisitions. Two statistical analysis methodologies have been applied: *Wilcoxon-Mann-Whitney test* which have produced box plots and *ROC curve analysis*. Both approaches have given consistent results: features with a statistical relevance ($p\text{-value} < 0.05$) have shown distinct samples in box plots and have produced good *Specificity* values in *ROC curves analysis*.

Nowadays, as reported in literature, dose value is the best parameter to discriminate responding from not responding lesions. Lesion absorbed dose values of completely responding metastases have been found significantly higher compared to the ones computed on not responding lesions. The threshold absorbed dose generally adopted in order to discriminate responding to not responding lesions is 85 Gy. ROC curve analysis have shown AUC values higher than 0.5 for lesion volumes not too small [60].

The associated criterion computed in *ROC curve analysis* is 81 Gy, very close to the one reported in literature. In terms of *AUC*, *Sensitivity* and *Specificity*, from our analysis, texture feature *HGZE*, *HGRE* and *Skewness*, *Kurtosis*, *Contrast* and *Dissimilarity* show better values (*HGZE*: $AUC=0.72$, *HGRE*: 45.5% Sensitivity and 100% Specificity, *Skewness*, *Kurtosis*, *Contrast*, *Dissimilarity*: 36.4% Sensitivity and 100% Specificity).

The main limit of our study has been the low number of patients.

We can assert that further patients inclusion in our dataset is necessary to increase the statistical power of this study.

Follow up of patients subjected to radioiodine treatment continues for months; the possibility to predict tumor response within the first week after treatment could be useful in patient management: based on prediction, further and more personalized treatments could be evaluated.

Abstract based on this thesis results was presented at the XIV Congresso Nazionale Associazione Italiana di Medicina Nucleare (AIMN) 2019 and it was accepted as "walking poster": it is reported in AppendixC.

Appendix A

Matlab script

```
dd=dir(C:...SPECTimages);
NN=length(dd);
infoPET=dicominfo(infoPET.IMA);
for ii=1:NN
XX=[C:...SPECTimages dd(ii).name];
spect3d(: , : , :)=dicomread(XX);
MM=size(spect3d,3);
dirname=[dd(ii).name new];
mkdir(dirname);
for jj=1:MM
infoSPECT=dicominfo(XX);
infoPET.PatientWeight=10;
infoPET.SliceThickness=infoSPECT.SliceThickness;
infoPET.Rows=infoSPECT.Rows;
infoPET.Columns=infoSPECT.Columns;
infoPET.SliceThickness=infoSPECT.SliceThickness;
infoPET.PixelSpacing=infoSPECT.PixelSpacing;
infoPET.Width=infoSPECT.Width;
infoPET.Height=infoSPECT.Height;
infoPET.NumberOfSlices=infoSPECT.NumberOfSlices;
infoPET.PatientName=infoSPECT.PatientName;
infoPET.MediaStorageSOPClassUID=1.2.840.10008.5.1.4.1.1.2;
infoPET.SOPClassUID=1.2.840.10008.5.1.4.1.1.2;
infoPET.ImagePositionPatient(1)=0;
infoPET.ImagePositionPatient(2)=0;
infoPET.ImagePositionPatient(3)=jj*infoSPECT.SliceThickness;
```

```
infoPET.SliceLocation=jj*infoSPECT.SliceThickness;
dicomwrite(spect3d(: , : , jj),[dirname infoSPECT.PatientName.FamilyName
num2str(ii-2) 'set' num2str(jj) '.IMA'], infoPET);
end
clear spect3d
end
```

Appendix B

Wilcoxon-Mann-Whitney test: probability values

B.1 p-values: first approach

Features	p values	Sensitivity (%)	Specificity (%)	Cut-off	AUC
HGZE	0.03	54.5	88.9	>701.2	0.72
HGRE	0.09	45.5	88.9	>716.4	0.68
Skewness	0.12	36.4	100	<=0.57	0.67
Kurtosis	0.12	36.4	100	<=2.32	0.67
Entropy	0.12	81.8	55.6	>1.68	0.67
Sphericity	0.55	100	27.8	>1.01	0.57
Compacity	0.43	81.8	44.4	<=1.97	0.59
Energy	0.25	72.7	50	<=0.25	0.63
Homogeneity	0.24	81.8	50	<=0.18	0.63
Contrast	0.25	45.5	83.3	>190.3	0.63
Dissimilarity	0.17	54.5	77.8	>11.3	0.65
SRE	0.44	54.5	83.3	>0.98	0.59
LRE	0.46	54.5	83.3	<=1.07	0.59
RP	0.46	54.5	77.8	>0.98	0.59
SZE	0.62	54.5	77.8	>0.79	0.56
LZE	0.43	54.5	83.8	<=2.3	0.60
LGZE	0.39	63.6	66.7	<=0.06	0.60
ZP	0.46	54.5	83.3	>0.74	0.59
GLCM Energy	0.93	27.3	88.9	<=0.01	0.51
GLCM Entropy	0.90	36.4	88.9	<=2.6	0.52
LGRE	0.93	45.5	72.2	<=0.07	0.51

B.2 *p*-values: second approach

Features	p values	Sensitivity (%)	Specificity (%)	Cut-off (%)	AUC
Skewness	0.10	54.5	88.2	>10.9	0.64
Contrast	0.61	36.4	100	<=-8.11	0.59
Dissimilarity	0.42	36.4	100	<=-3.8	0.60
HGRE	0.33	45.5	100	<=-8.2	0.66
Sphericity	0.72	55.6	94.1	>0.43	0.68
Kurtosis	0.14	54.6	94.1	>10.9	0.66
Comapacity	0.54	81.8	52.9	>-0.56	0.67
GLCM Energy	0.24	45.5	94.1	>9.6	0.60
GLCM Entropy	0.42	45.5	94.1	<=-1.16	0.57
Entropy	0.26	63.6	82.4	<=1.01	0.63
Homogeneity	0.33	72.7	70.6	>0.96	0.68
SRE	0.48	63.6	64.7	<=-0.2	0.58
LRE	0.54	54.5	70.6	<=-0.3	0.55
LGRE	0.54	54.5	76.5	>15.9	0.60
RP	0.54	54.5	70.6	<=-0.3	0.55
SZE	0.45	45.5	82.4	<=-5.6	0.58
LZE	0.58	63.6	70.6	>12.2	0.60
LGZE	0.51	72.7	52.9	>-4.9	0.56
HGZE	0.96	63.6	82.4	<=-2.8	0.65
ZP	0.48	63.6	70.7	<=-4.8	0.58

Appendix C

Abstract presented at XIV Congresso Nazionale Associazione Italiana di Medicina Nucleare (AIMN) 2019

Feasibility and prognostic impact of features analysis on ^{131}I SPECT-CT images in metastatic thyroid patients treated with radioiodine

Matteo Poli(1), Claudia Cutaia(1), Alessandra Pecora(1), Elisa Richetta(1), Viviana Garbaccio(2), Désirée Deandreis(3), Riccardo Pellerito(2), Michele Stasi(1)

(1) Nuclear Medicine Dept. AO Ordine Mauriziano, Turin (2) Medical Physics Dept. AO Ordine Mauriziano, Turin (3) Nuclear Medicine Dept., Turin

Introduzione

In metastatic differentiated thyroid cancer (MDTC) the radioiodine treatment is a consolidated approach. The effectiveness of the therapy can be verified on post administration imaging where tomography represents the most accurate option. Aim of this study is to evaluate the feasibility and prognostic impact of ^{131}I SPECT-CT images features analysis (FA) performed on metastatic lesion in MDTC patients.

Materiali

FA is performed on SPECT-CT images with a free software (LIFEx, CEA 2017) taking into account texture features (TF) and first-order features (FF). TF include Gray-Level Occurrence Matrix GLCM (e.g. homogeneity, contrast) and Gray-Level Zone Length Matrix GLZLM (e.g. HGZE); FF include histograms indices (e.g. skewness, kurtosis and entropy). On a spheres phantom (NEMA PET IEC) filled with liquid ^{131}I (13 MBq/ml), SPECT-CT images (at 3,120,160,216 h after preparation) were acquired. Five volume of interests (VOIs) were contoured on phantom images, one for each sphere. VOIs were made

by a 3D segmentation tool choosing a threshold value to obtain a volume the most similar to the real one. Then, we performed TF and FF analysis using six different discretization levels (4, 8, 16, 32, 64, 128) on every single VOI. As results, the best discretization level to use and the minimum VOI volume that should be evaluated with this method were defined.

Risultati

For 6 MDTC patients (inclusion criteria: thyroidectomy, iodine remnant ablation) TF and FF analysis were computed on 4 SPECT-CT images (Siemens IntevoT2, 256x256, ITSCAC) acquired at 4,24,48,96 h after administration. Mean doses to lesion (MIRD sphere model) were also evaluated. 22 lesions (14 bone, 8 visceral) were contoured by a nuclear medicine specialist using a 3D segmentation tool and TF and FF analysis were computed. Treatment outcome was classified as responding (complete and partial response) or not responding (stable and progressive disease). FA was therefore correlated to 131I treatment response through ROC analysis (AUC, sensitivity (SS) and specificity (SP)).

In phantom analysis the minimal assessable volume was found equal to 1.2 cc and the optimal discretization level was found equal to 64, as suggested by literature: those results were therefore applied in patients analysis. In patients, mean dose ROC analysis showed an AUC equal to 0.62 (SS 75, SP 64). Similar results were found on GLCM features (homogeneity AUC 0.62, SS 63, SP 71 and contrast AUC 0.61, SS 38, SP 93). Higher effectiveness to discriminate the patient treatment response was shown by some FF features (skewness and kurtosis AUC 0.72, SS 50, SP 100, entropy AUC 72, SS 63, SP79) as well by TF Gray-Level Zone Length Matrix (HGZE AUC 0.76, SS 75, SP 93).

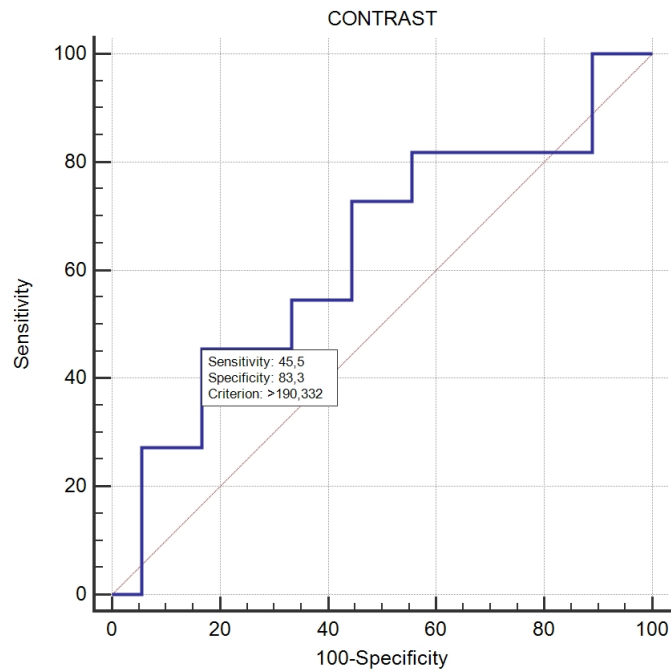
Conclusioni

In MDTC patients features analysis on 131I SPECT-CT images is feasible. Phantom analysis points out methods limits, allowing a standardization. Many features were evaluated in order to investigate their influence in the patient response discrimination. A positive prognostic capability was shown. These results should be integrated with the standard dose-response evaluation, giving to the physician a powerful tool in MDTC patients treatment management. However, the small sample involved does not allow clinical results yet: additional patients involved would consolidate the prognostic and predictive role of FA on 131I treatment response.

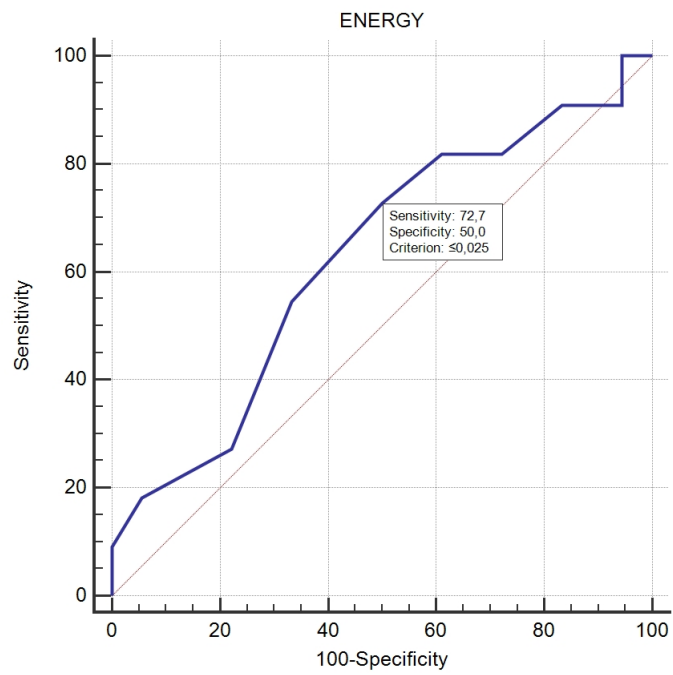
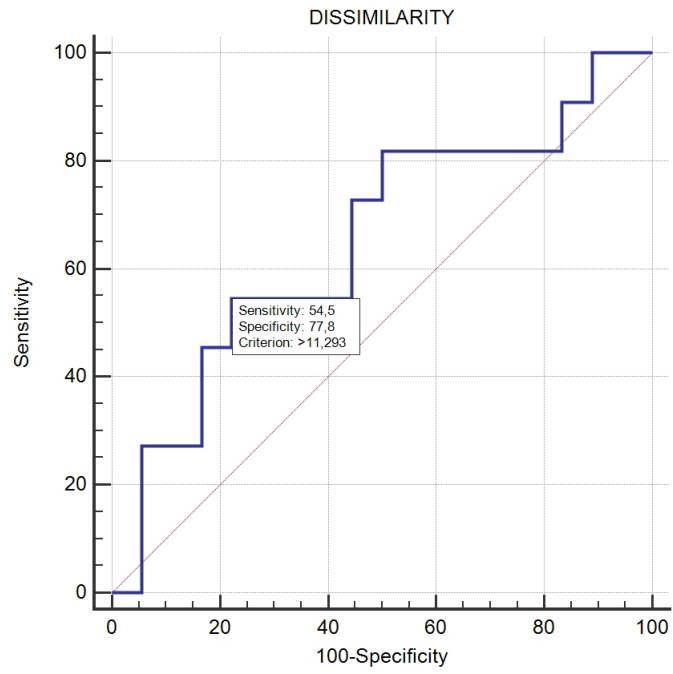
Appendix D

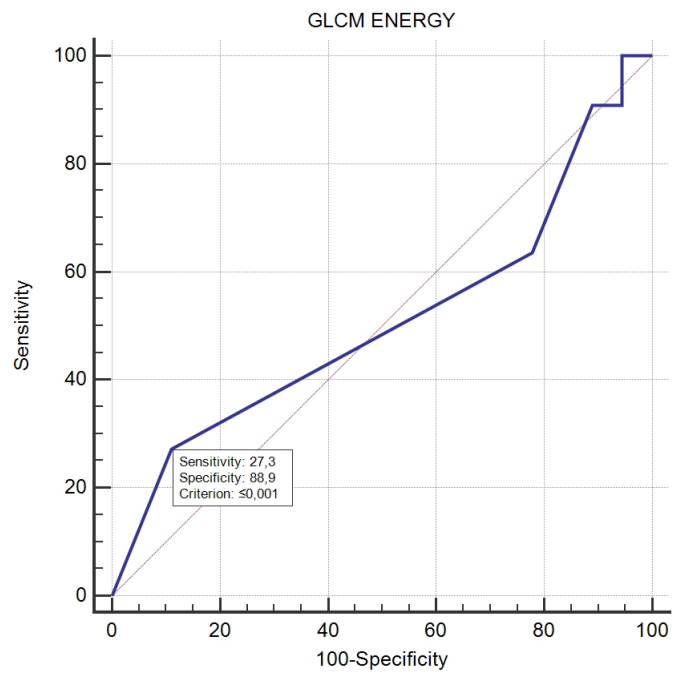
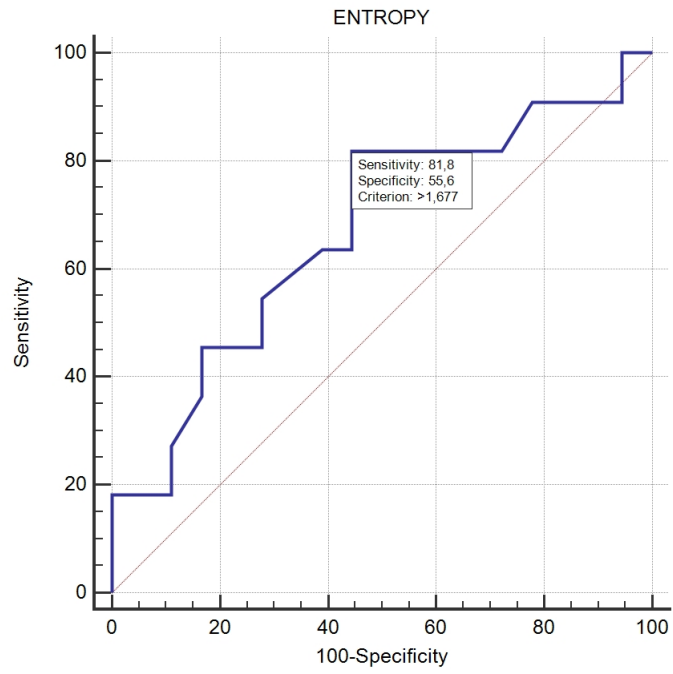
ROC curve analysis

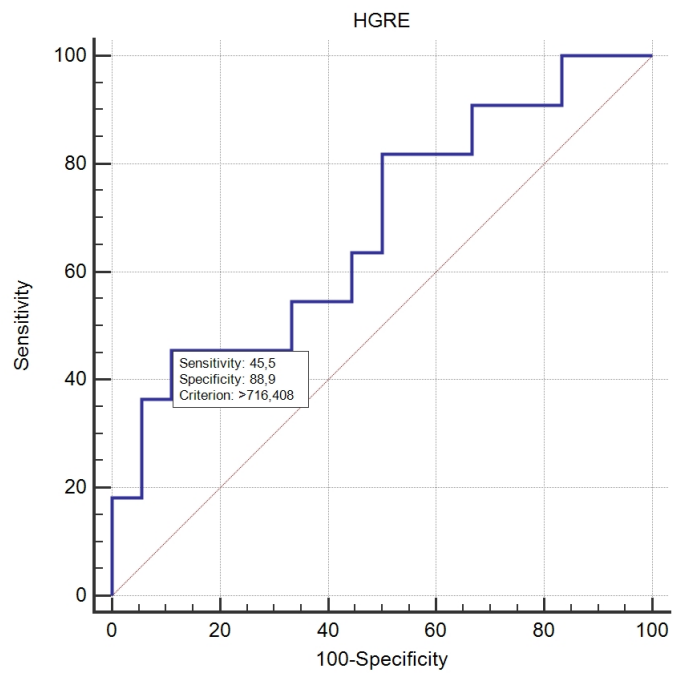
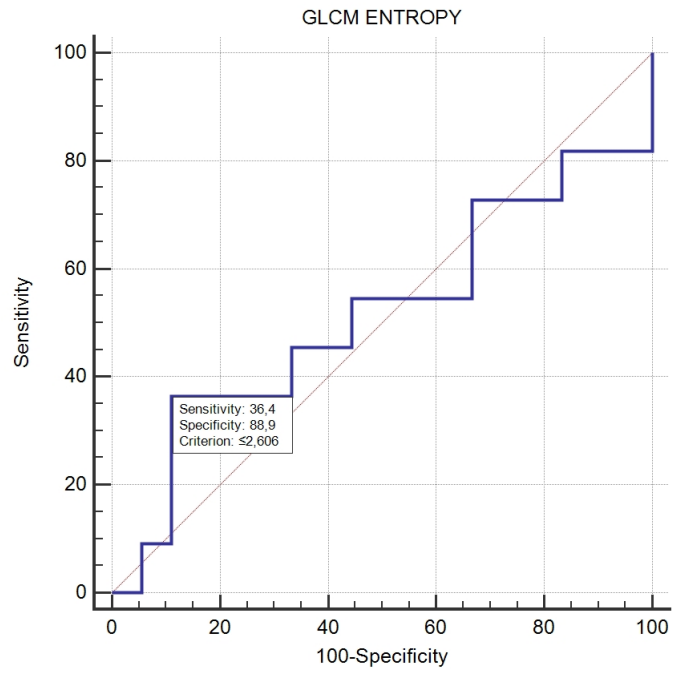
D.1 ROC curve analysis: first approach

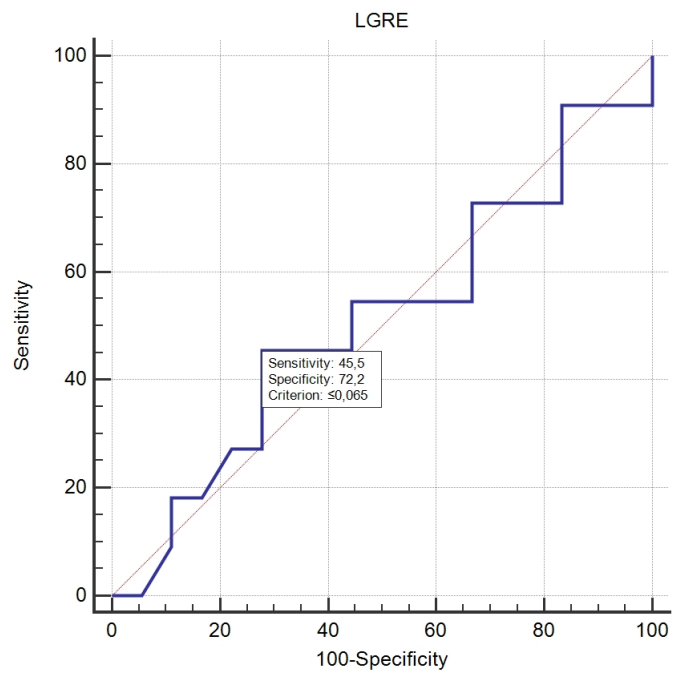
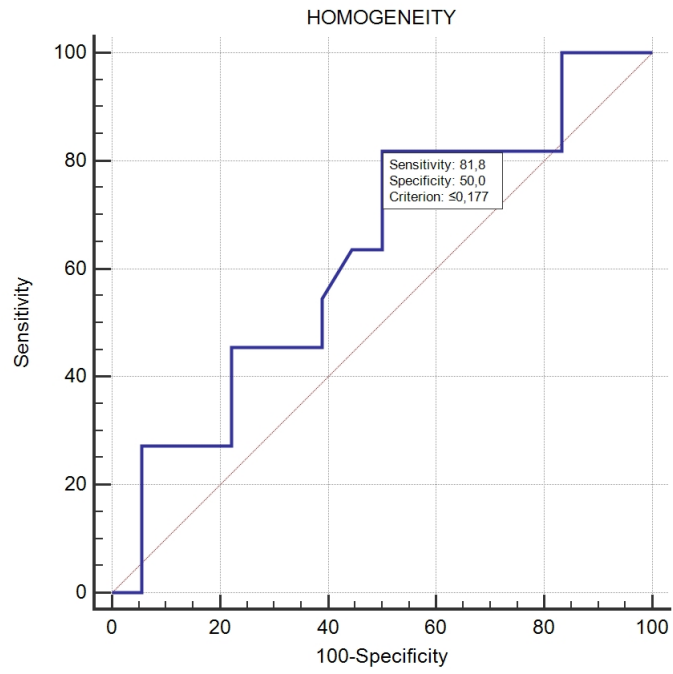


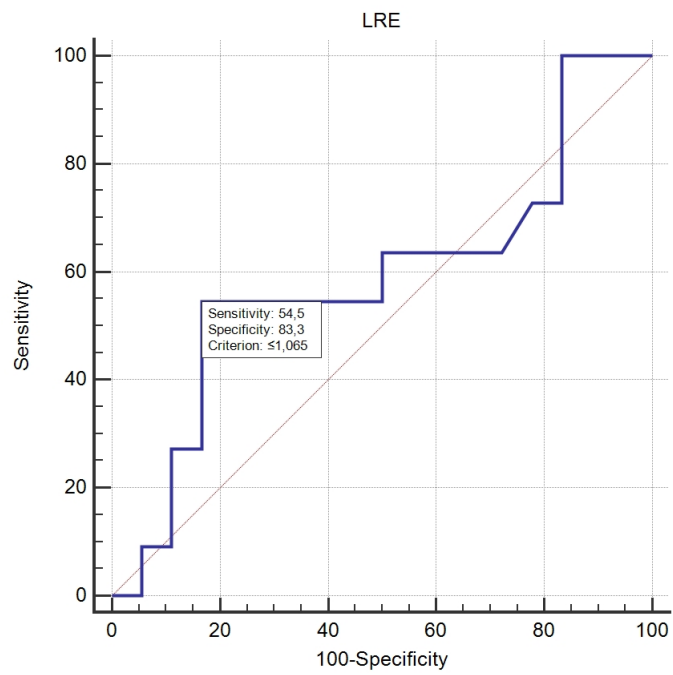
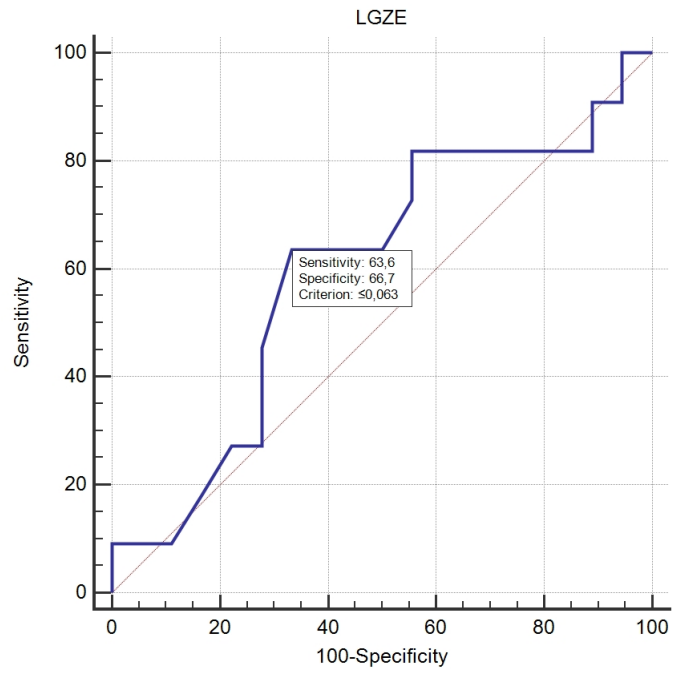
D.2 ROC curve analysis: second approach

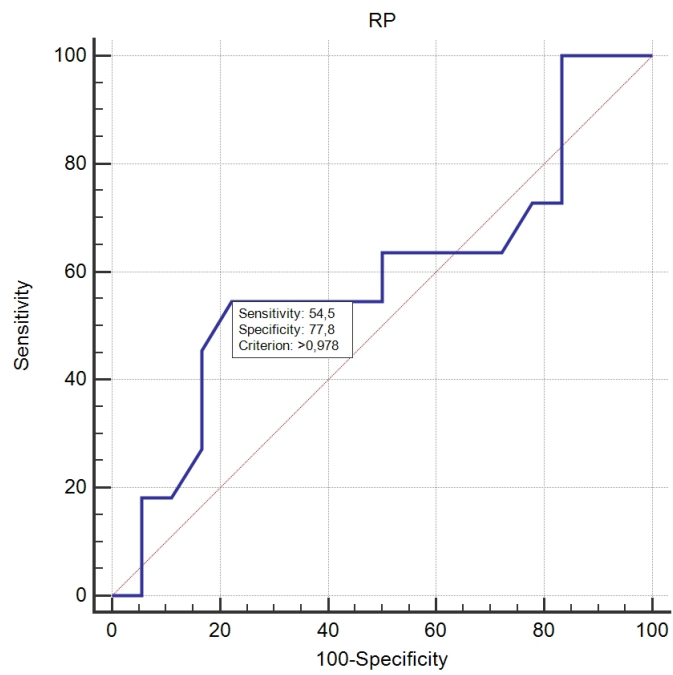
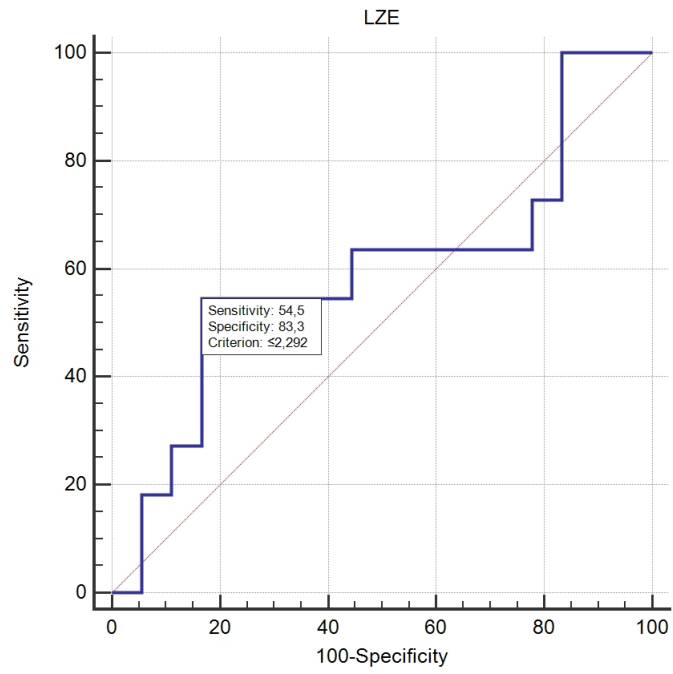


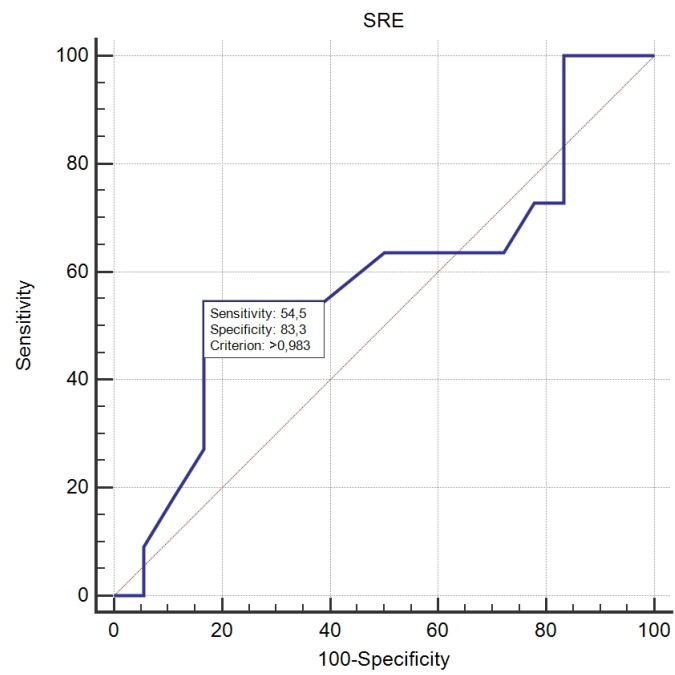
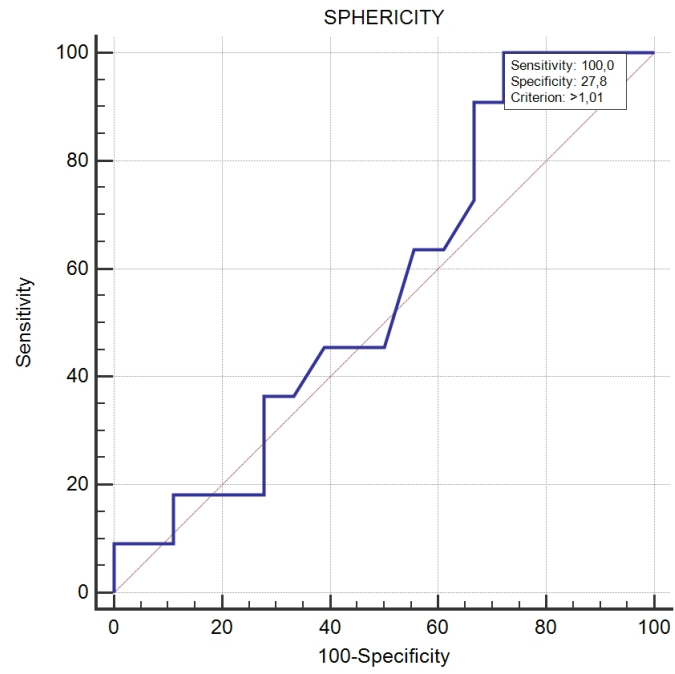


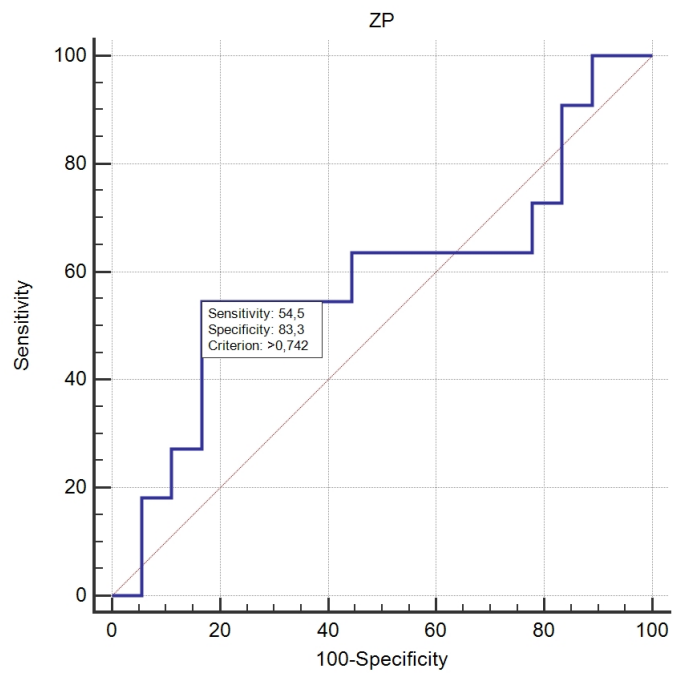
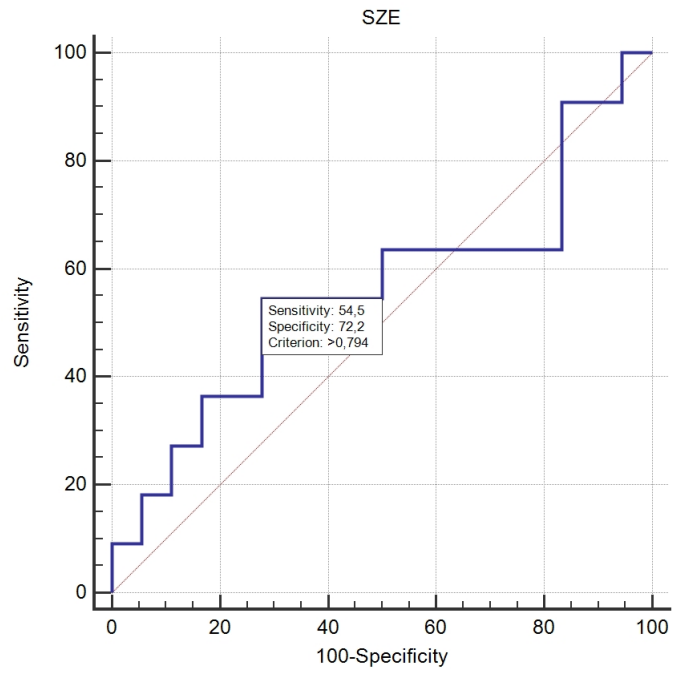


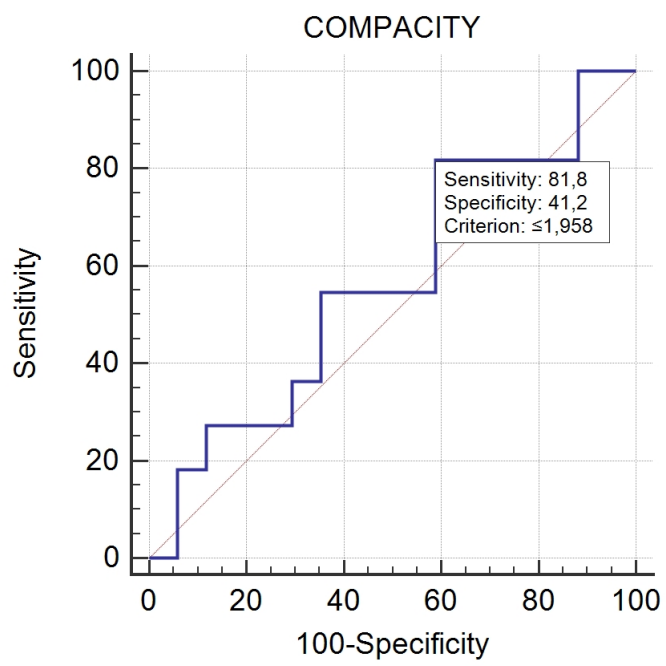


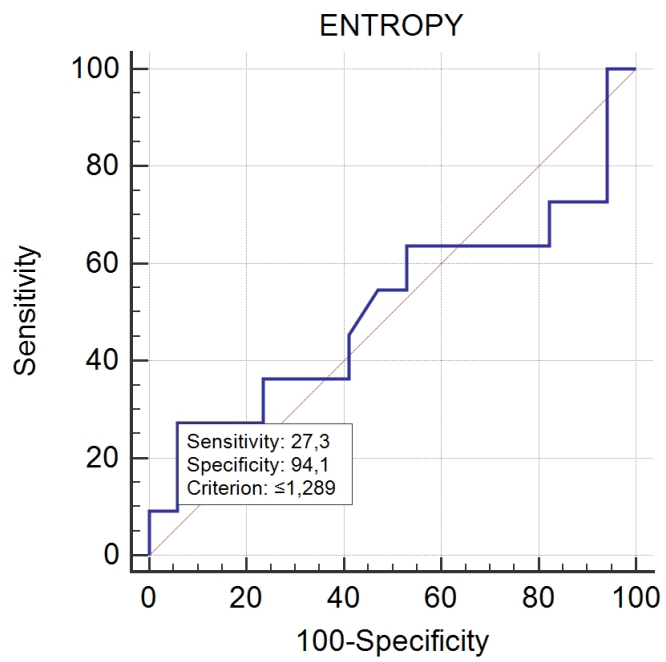
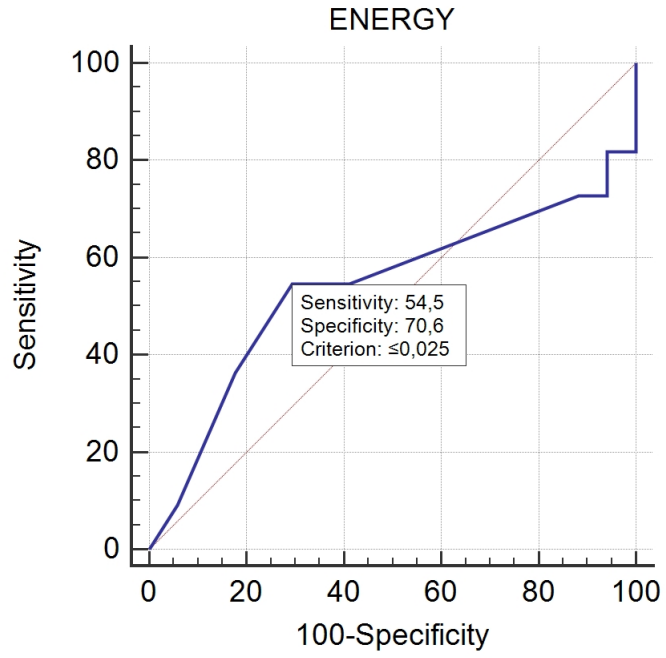


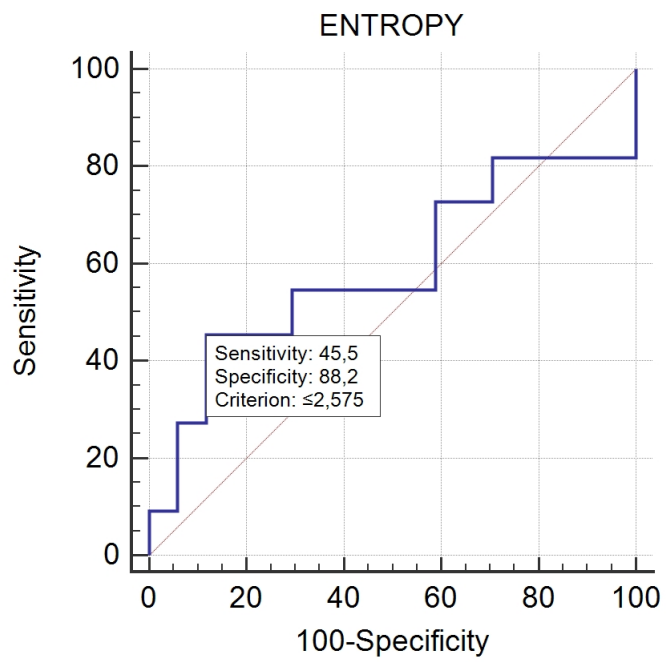
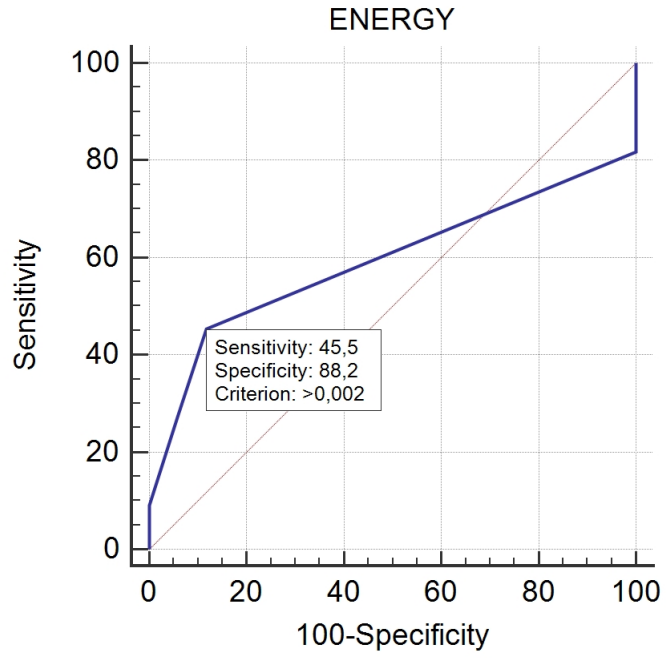


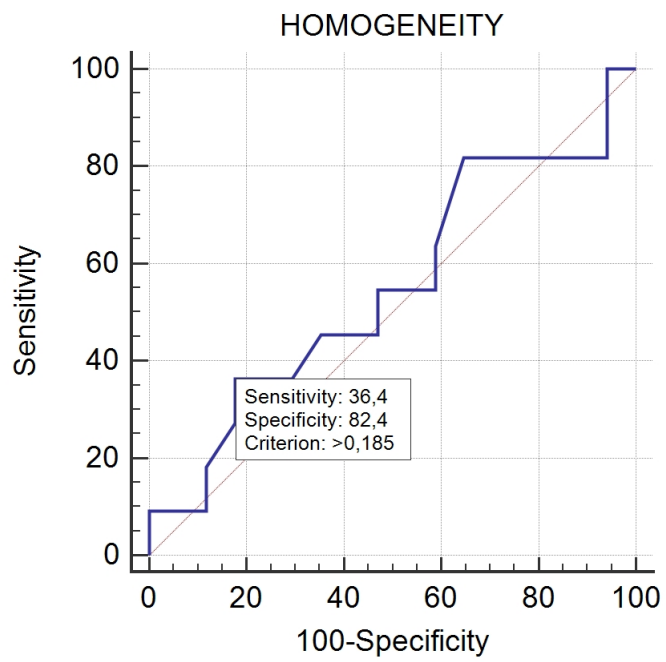
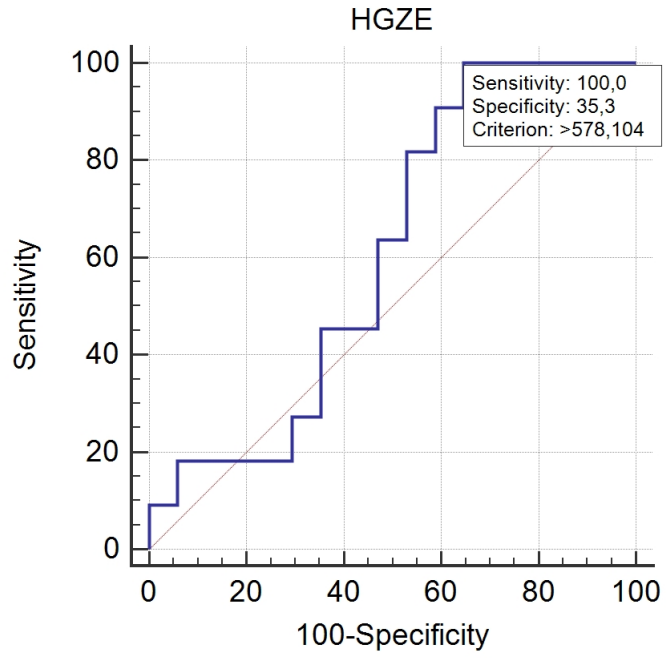


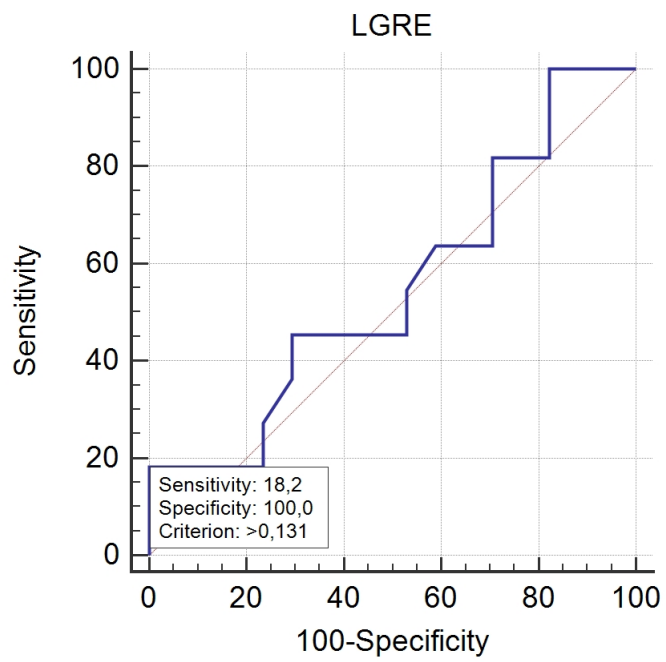
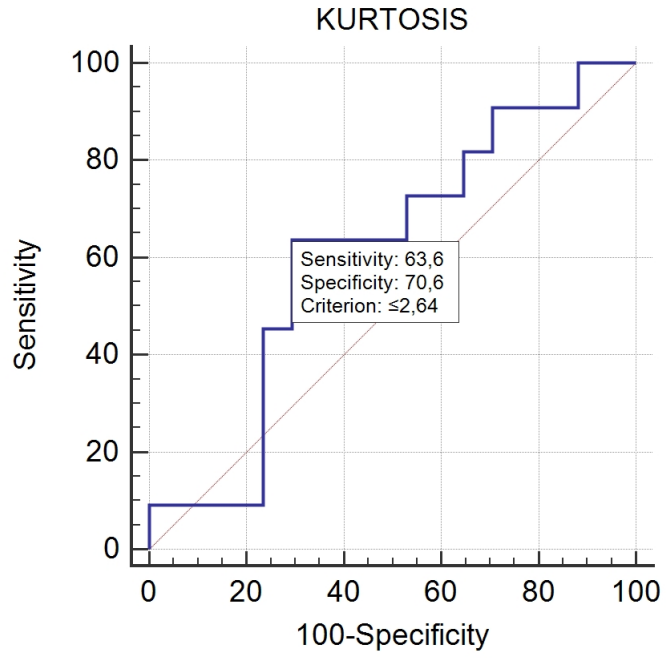


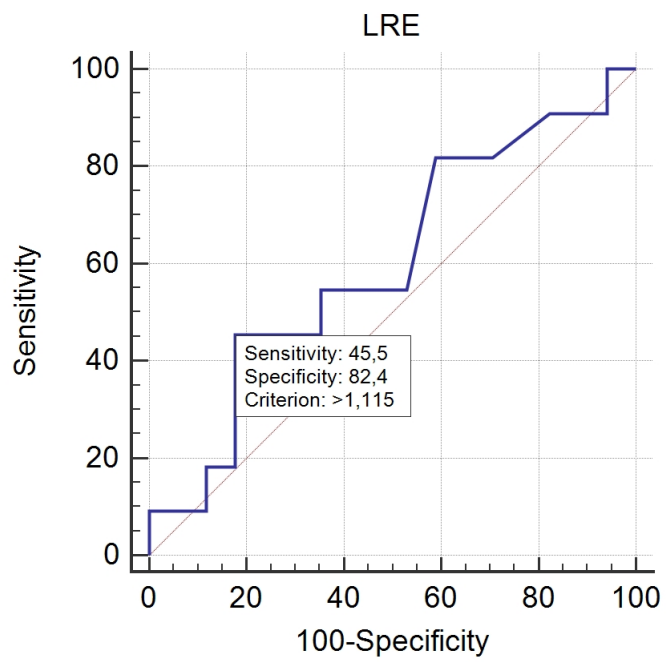
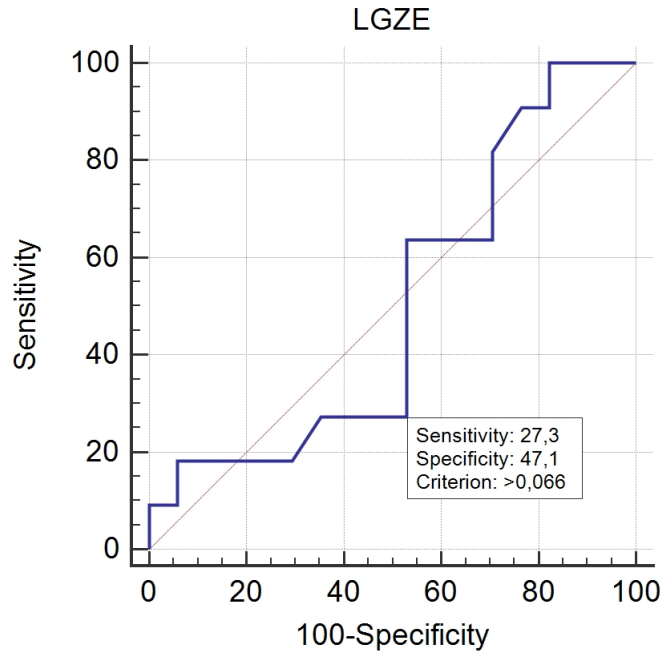


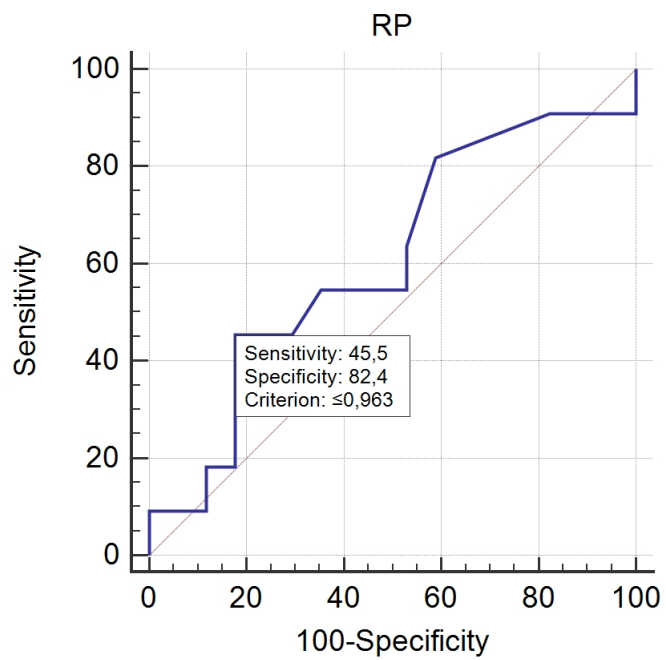
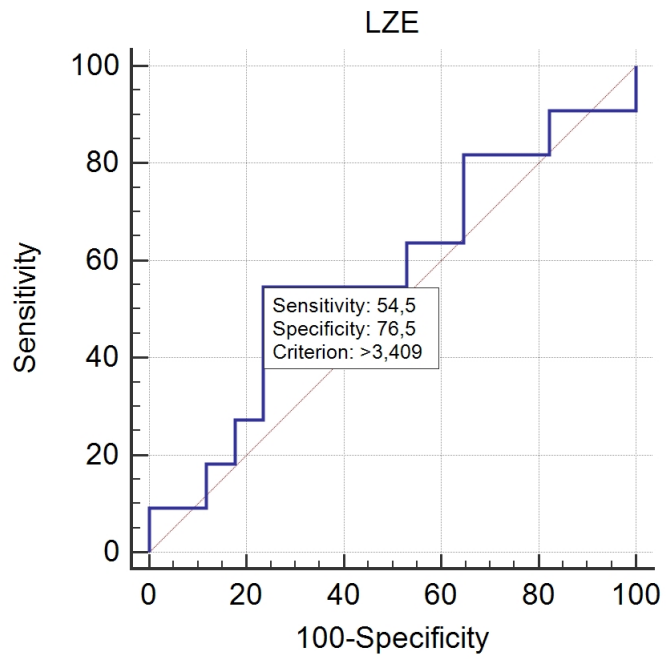


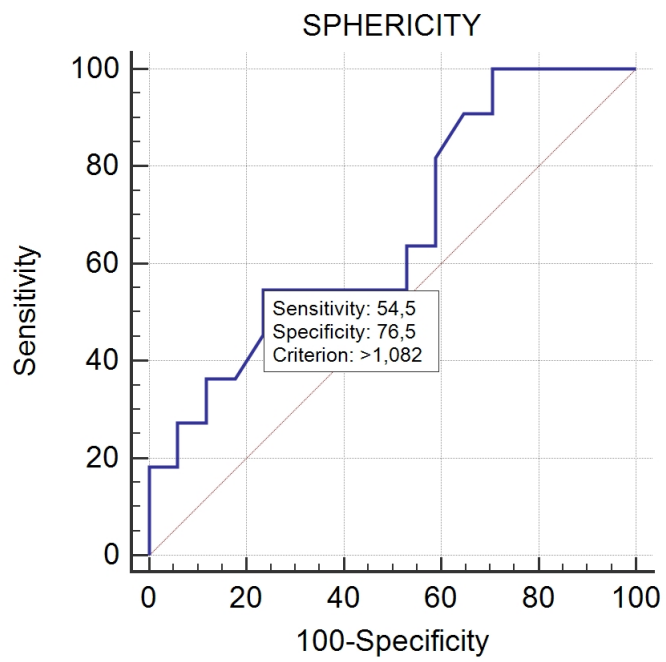
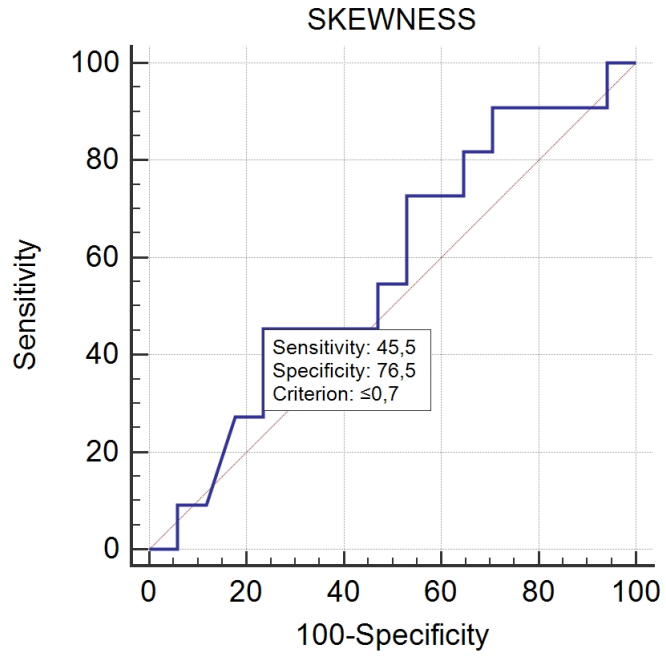


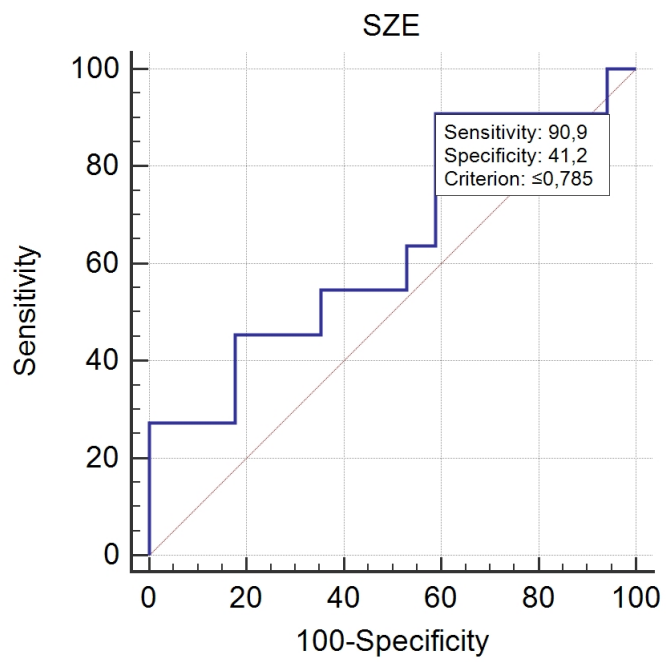
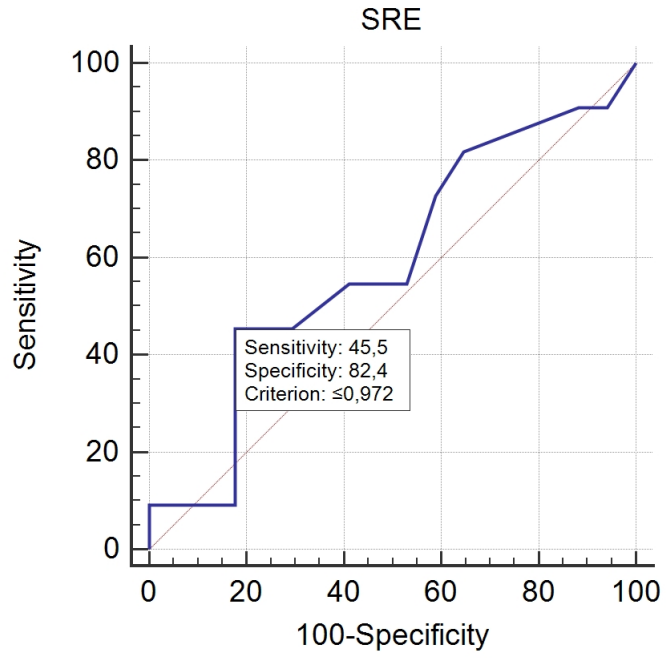


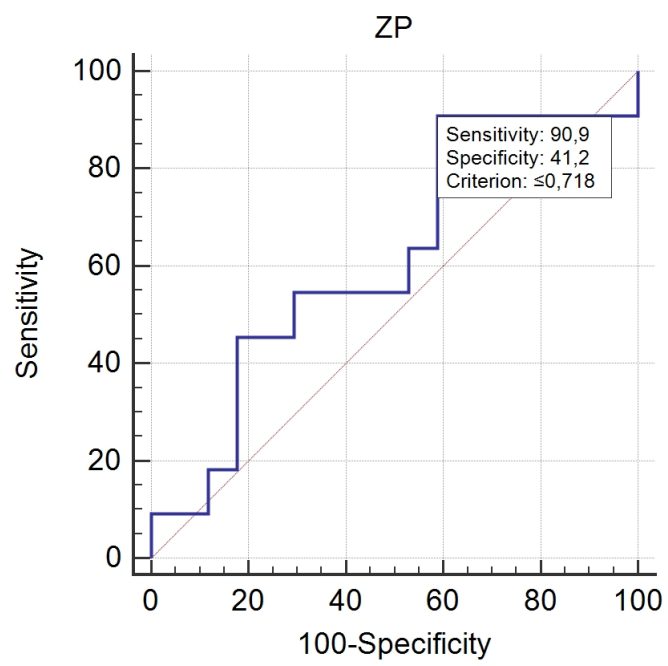








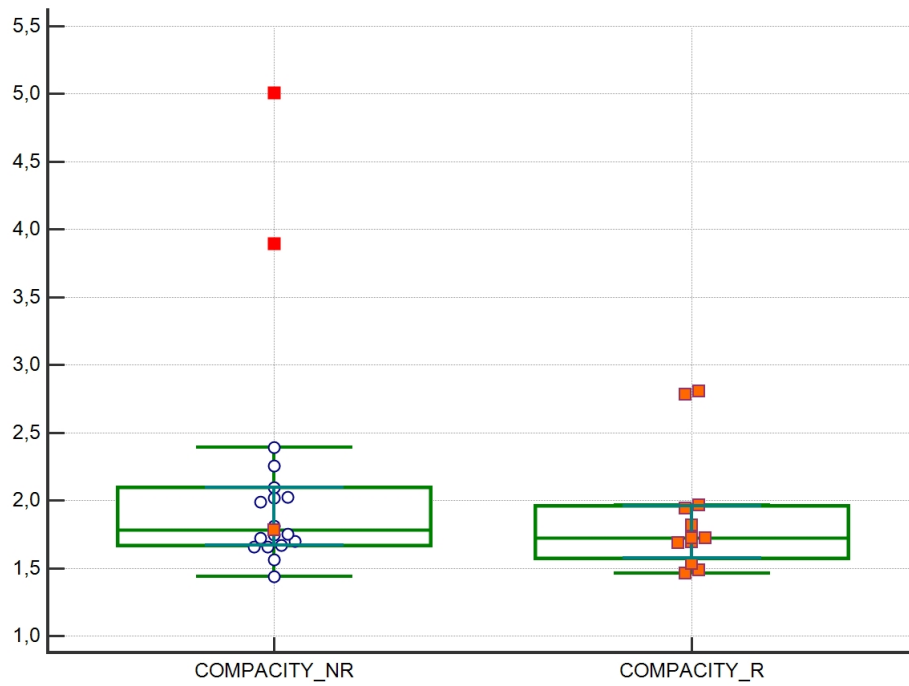




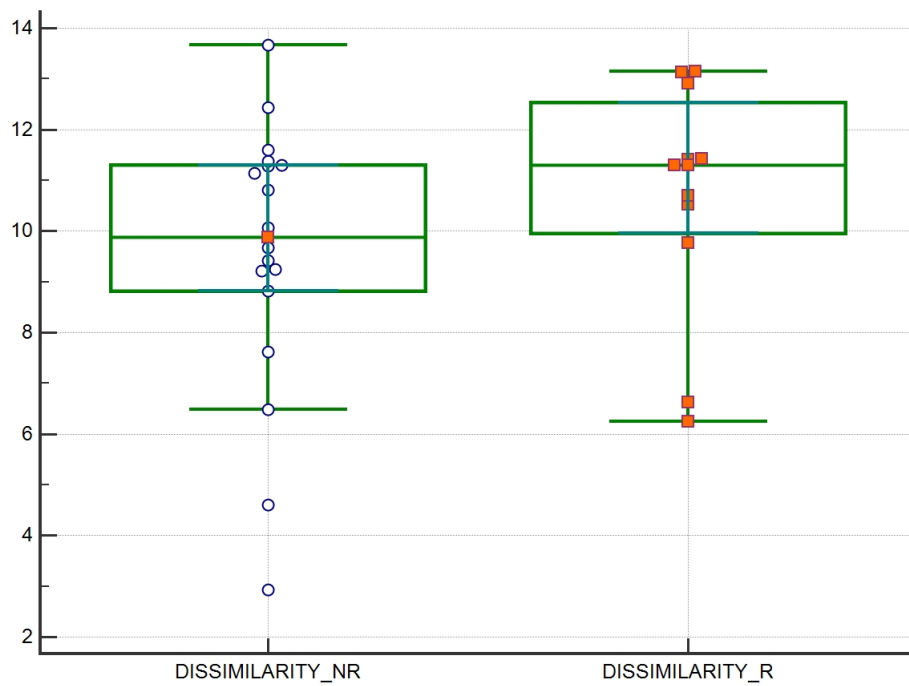
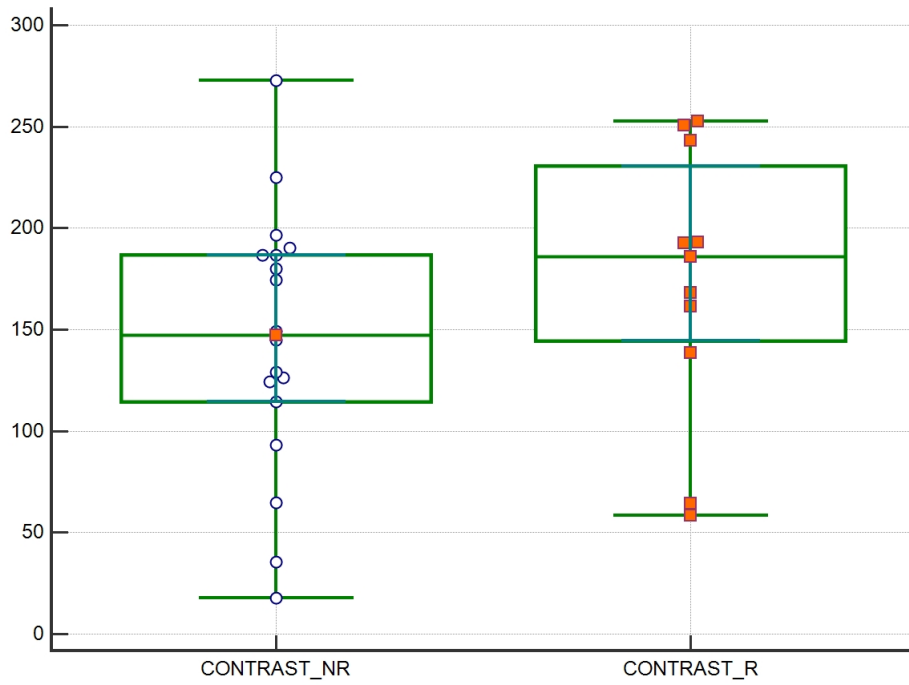
Appendix E

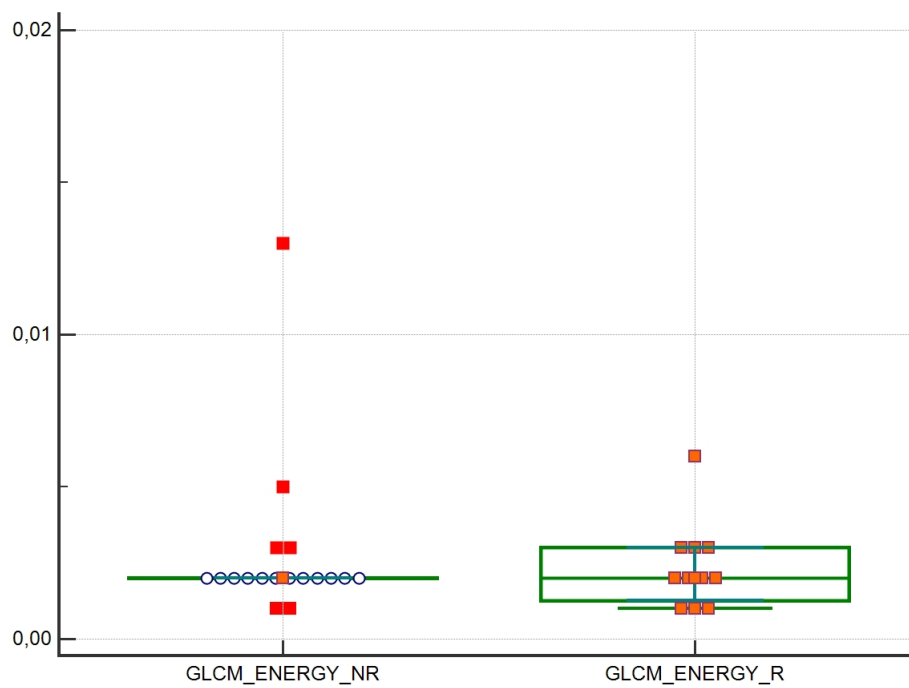
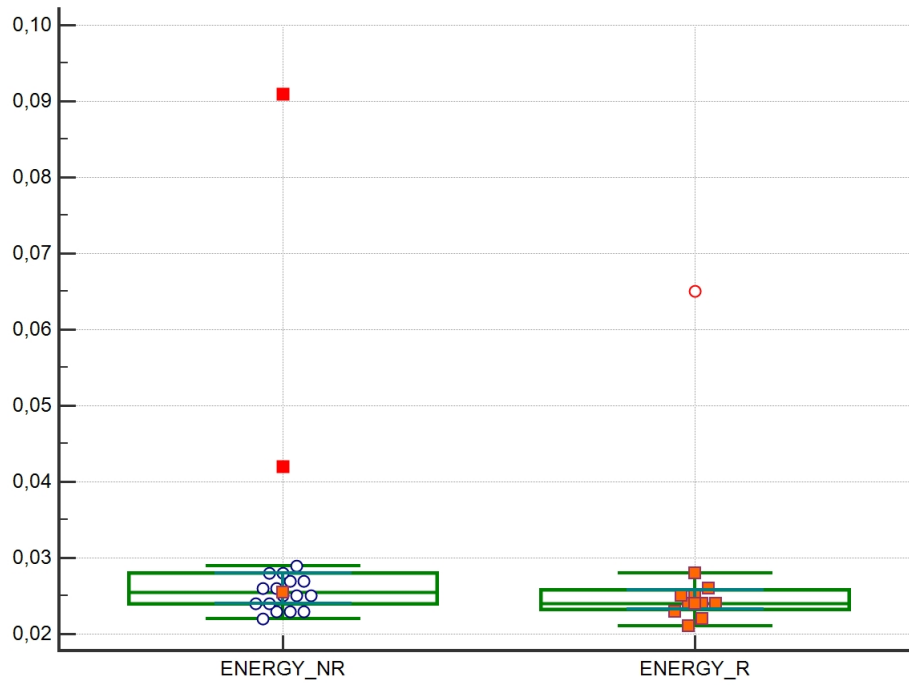
Box and whisker plots

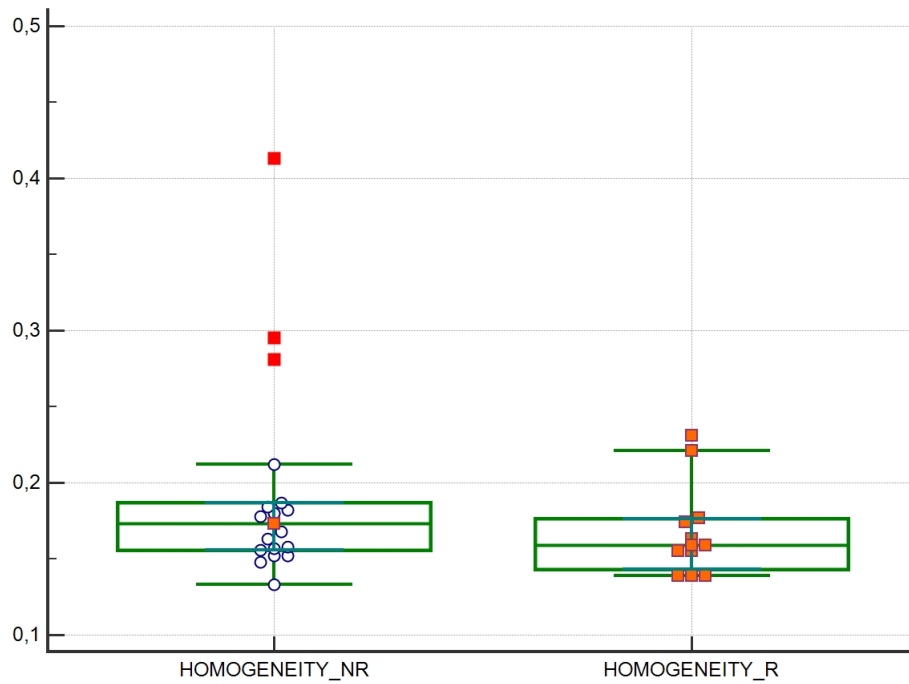
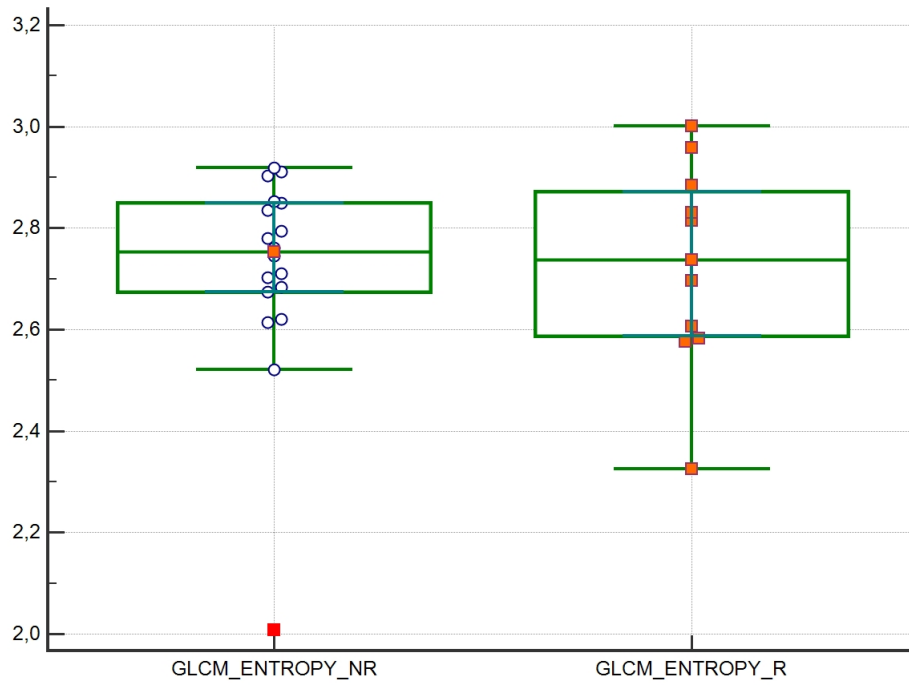
E.1 Box plot: first approach

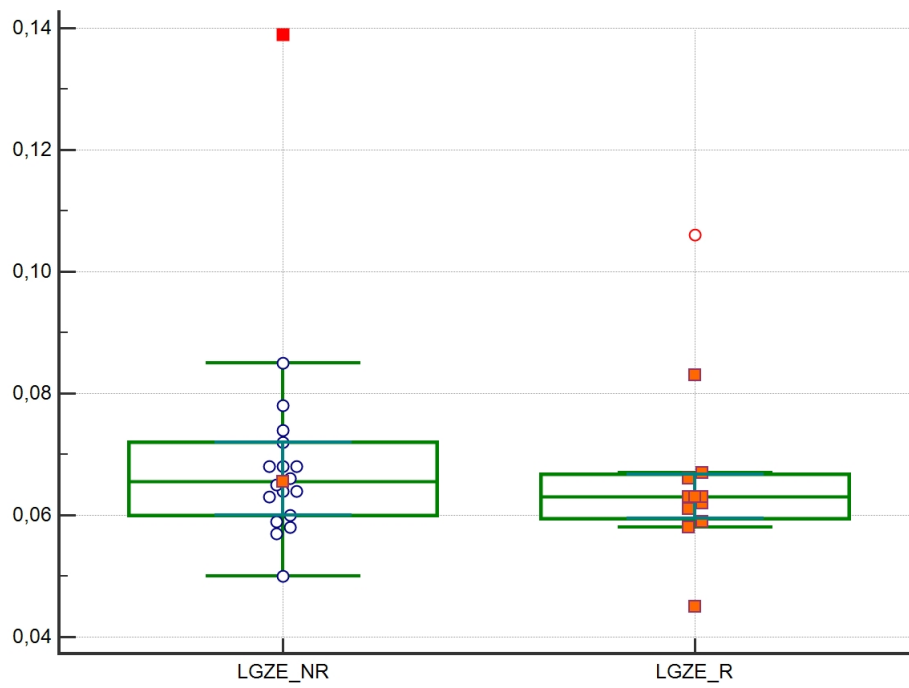
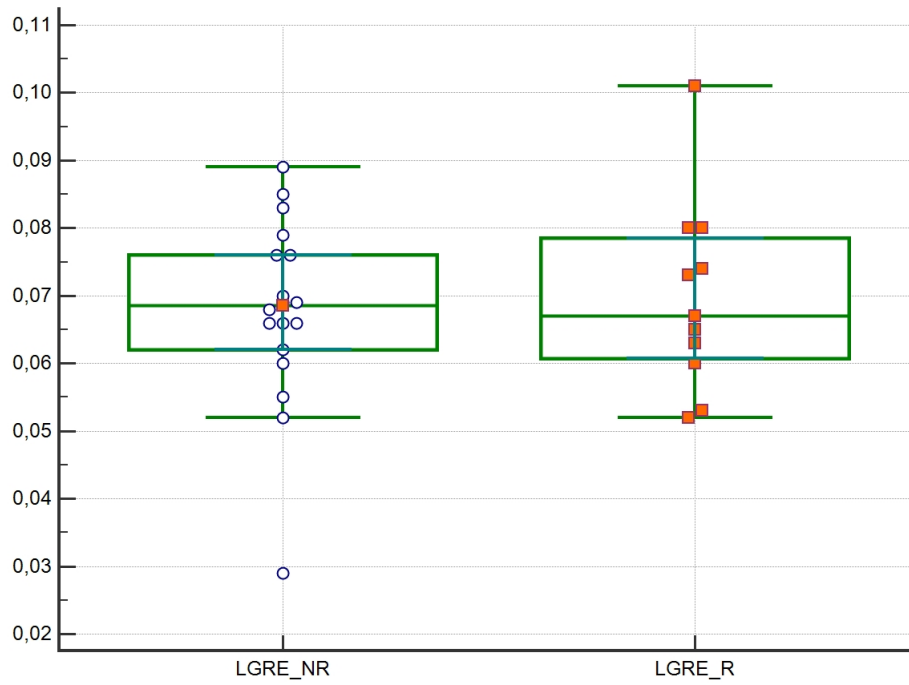


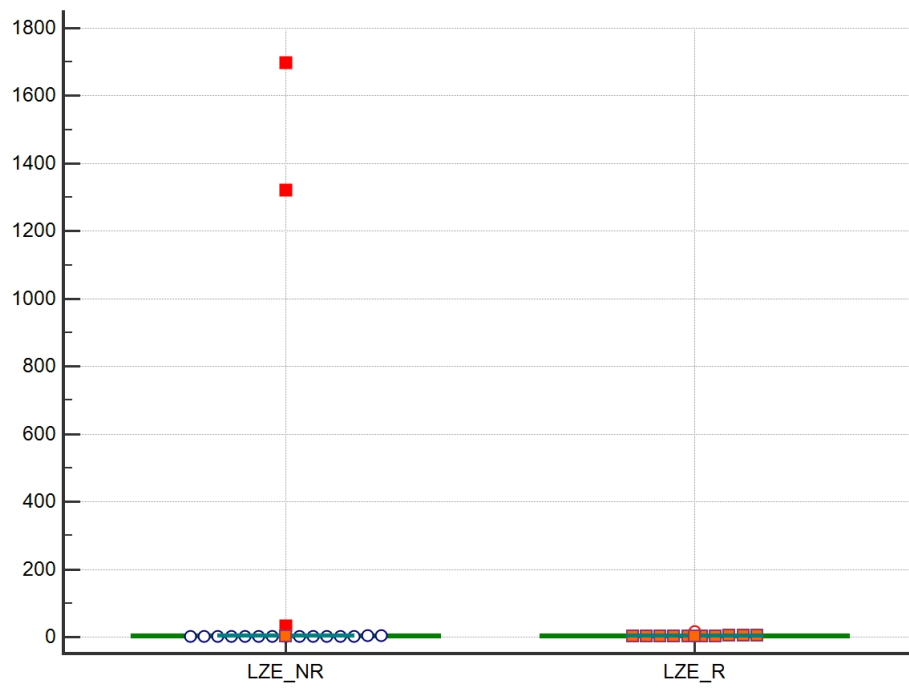
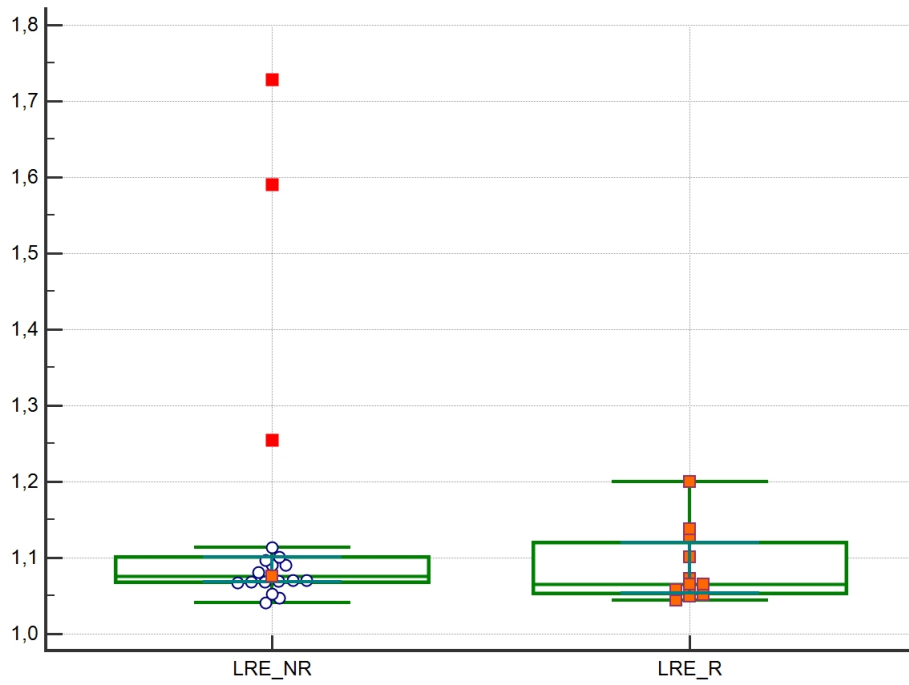
E.2 Box plot: second approach

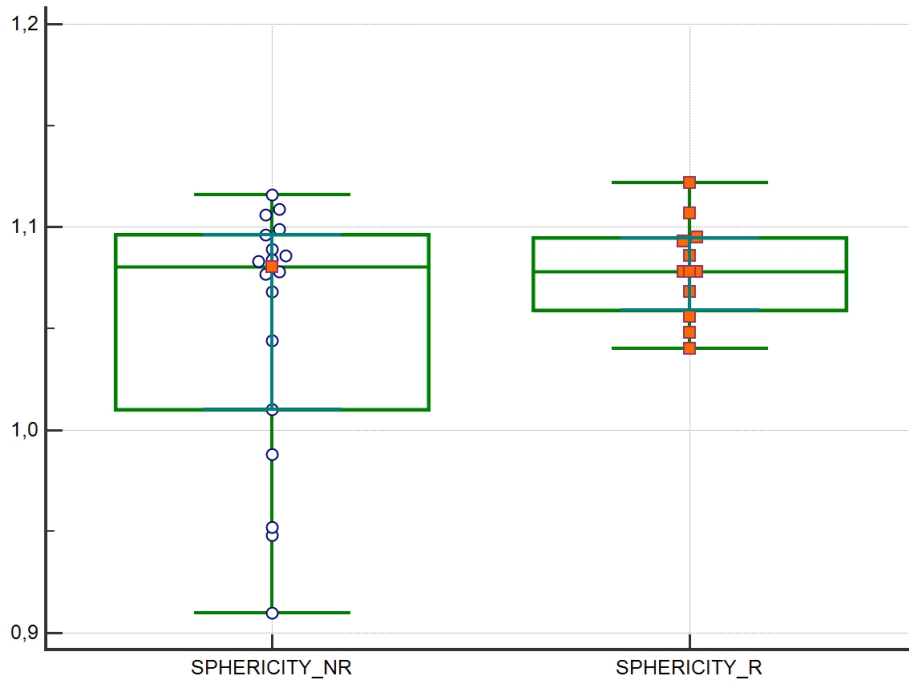
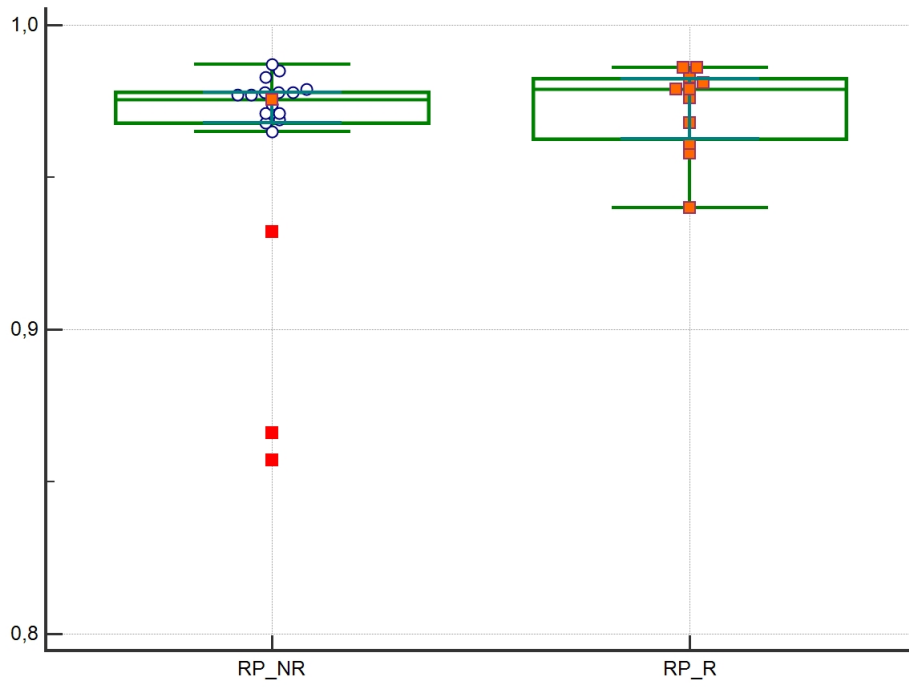


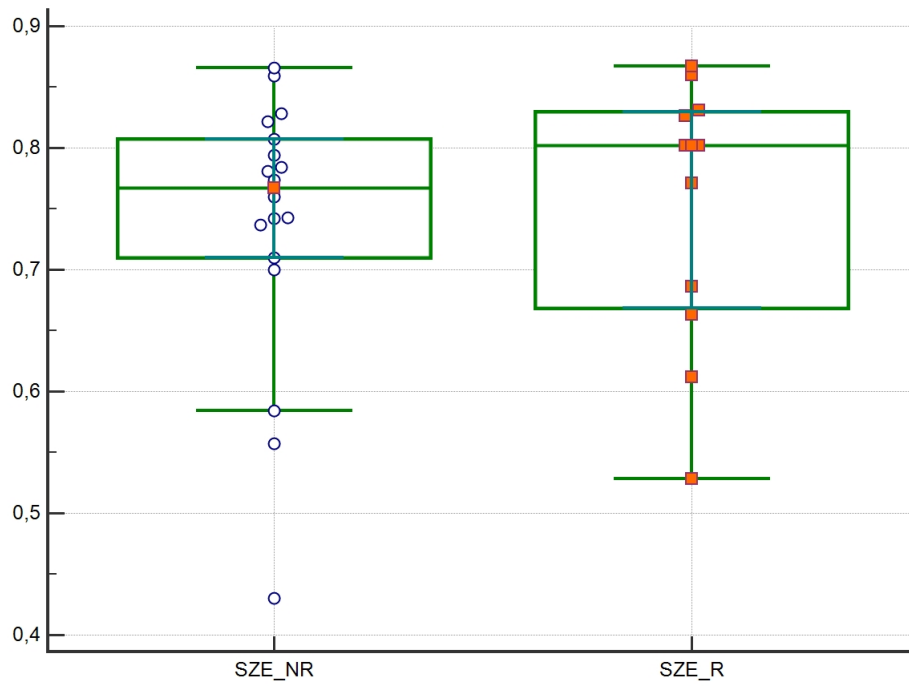
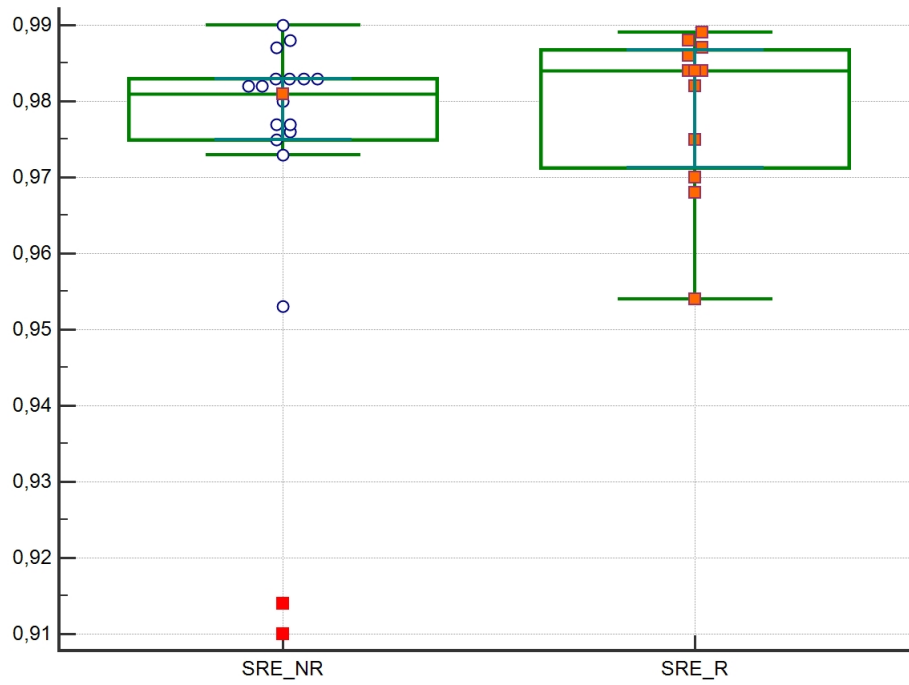


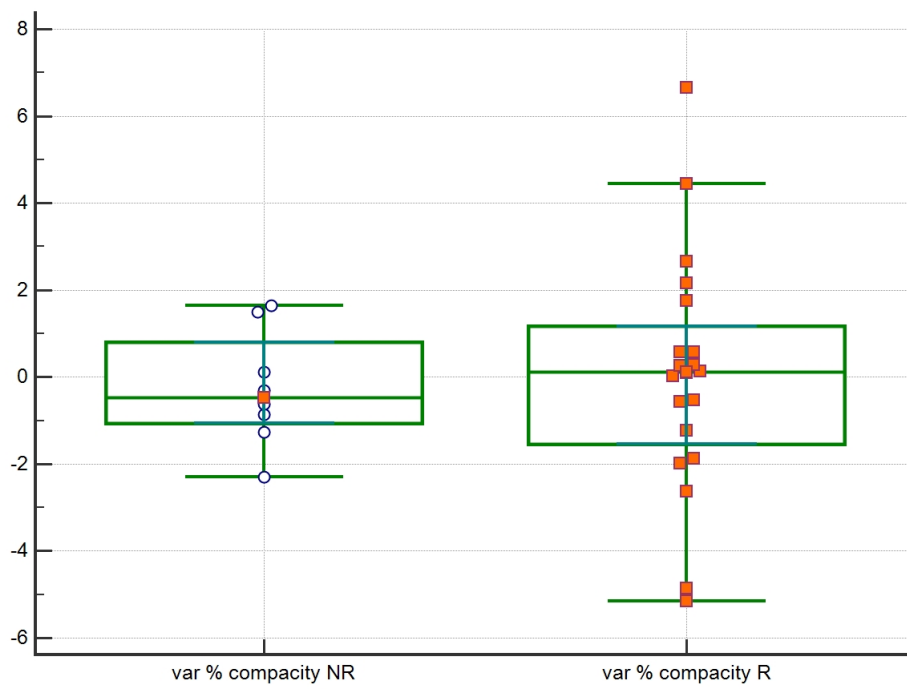
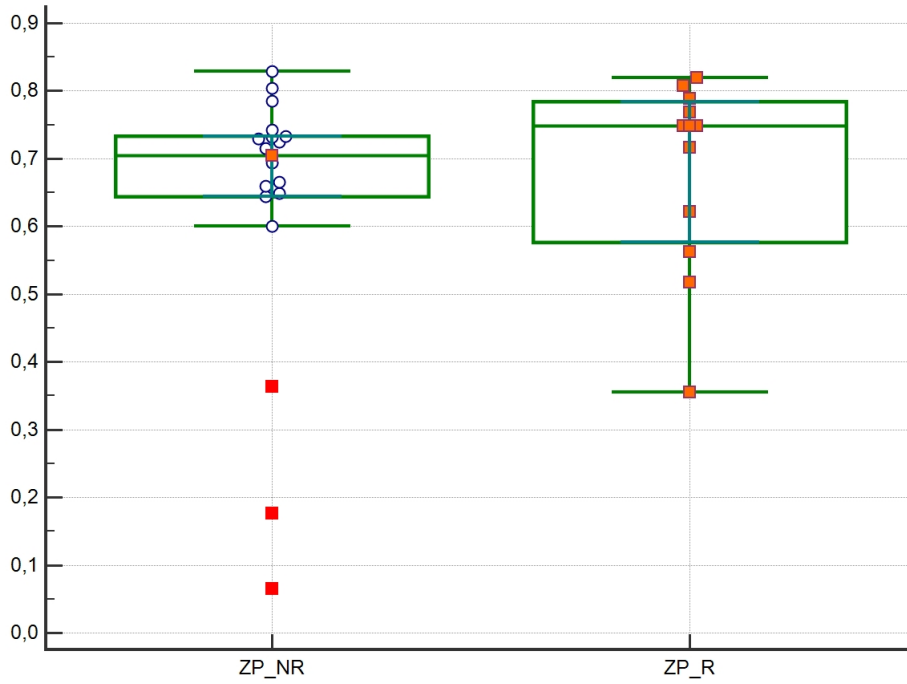


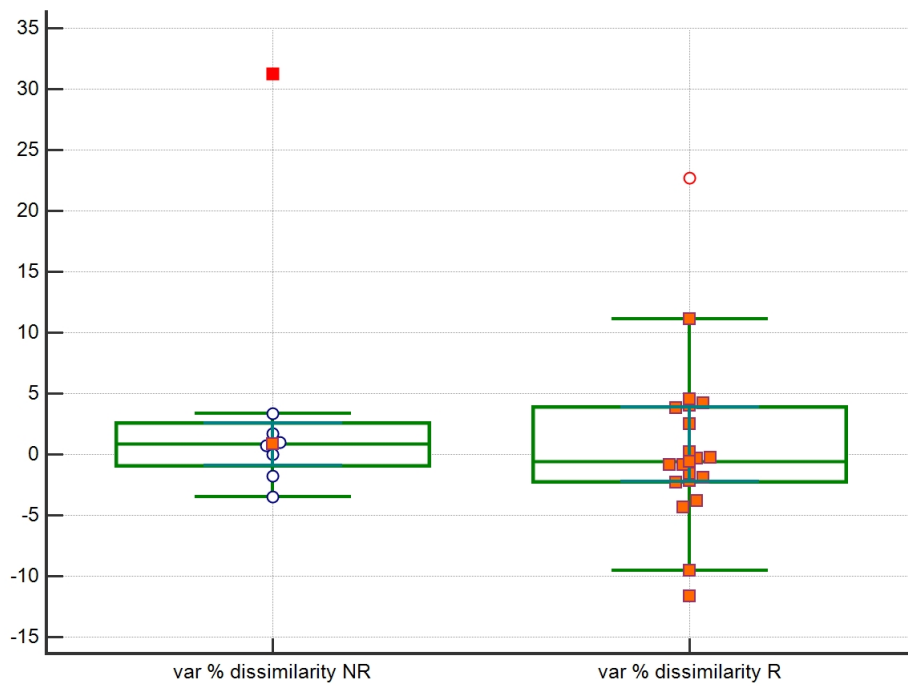
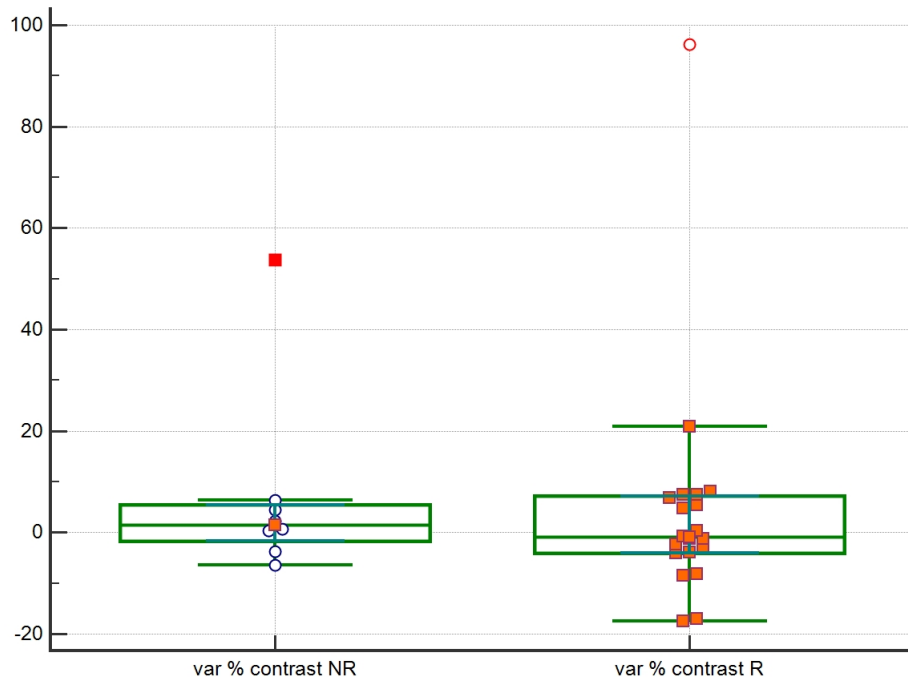


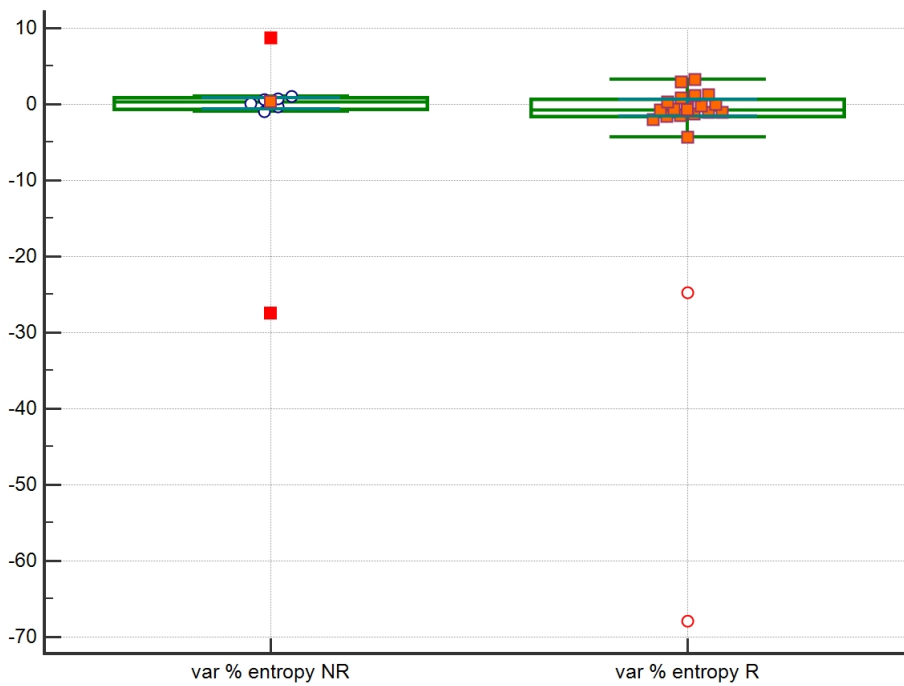
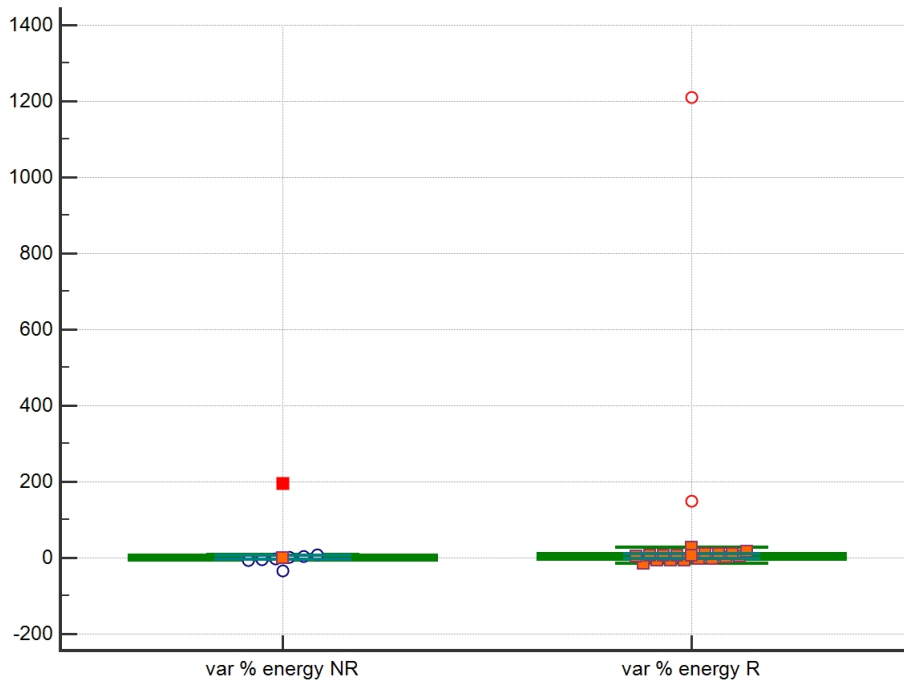


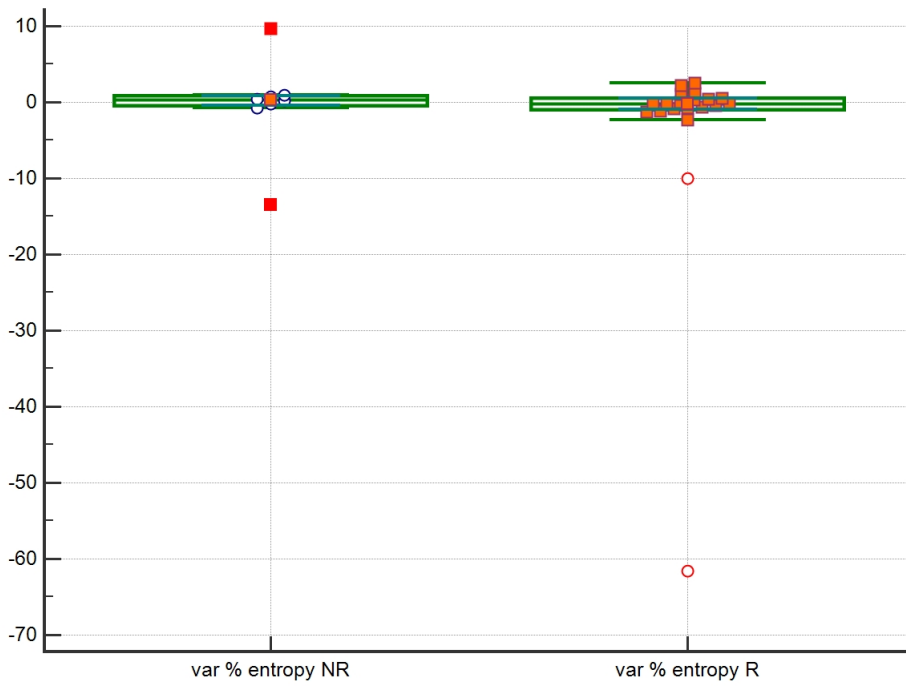
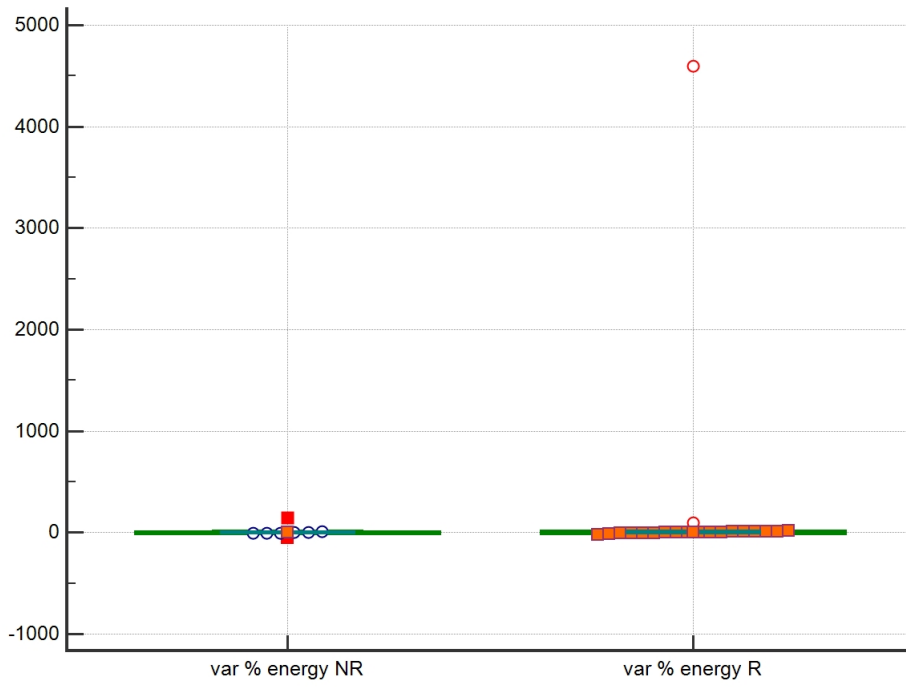


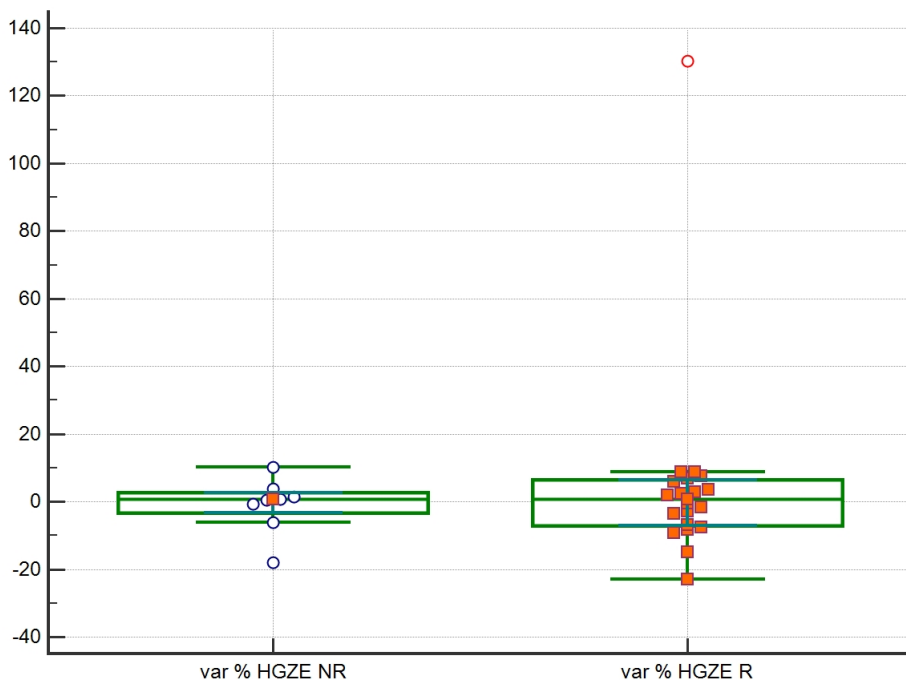
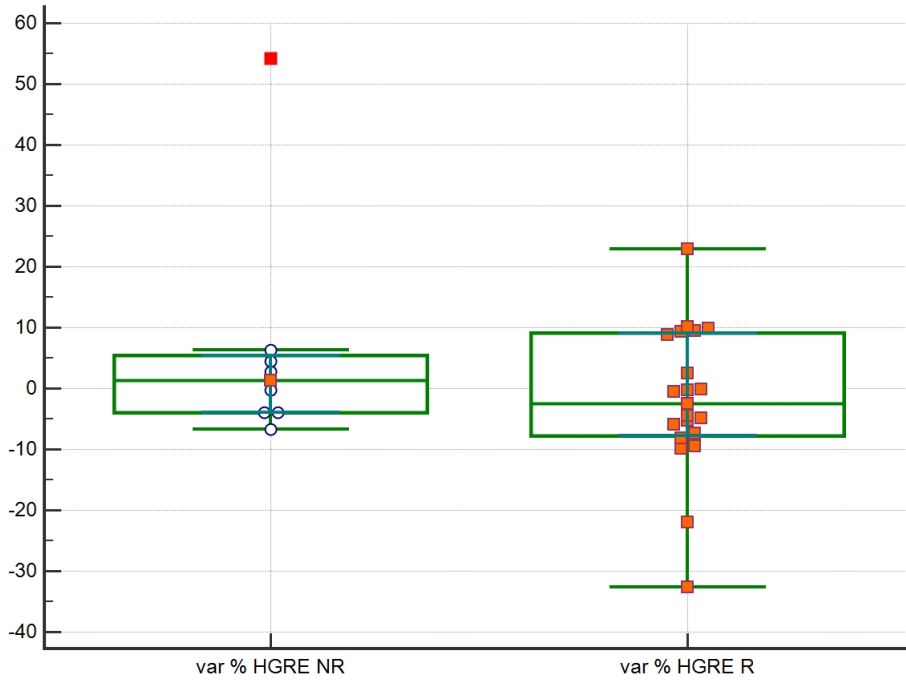


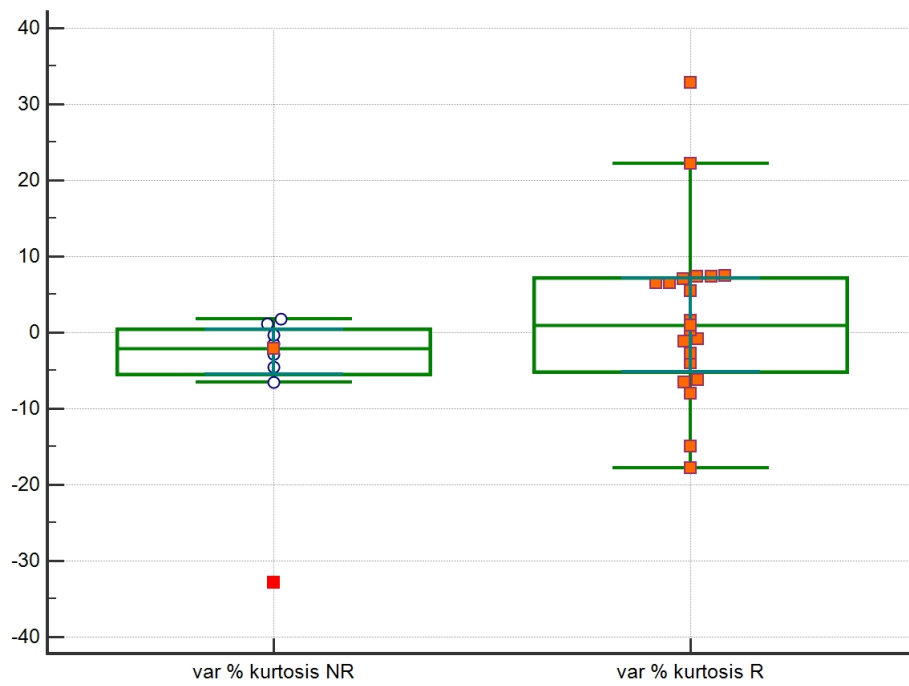
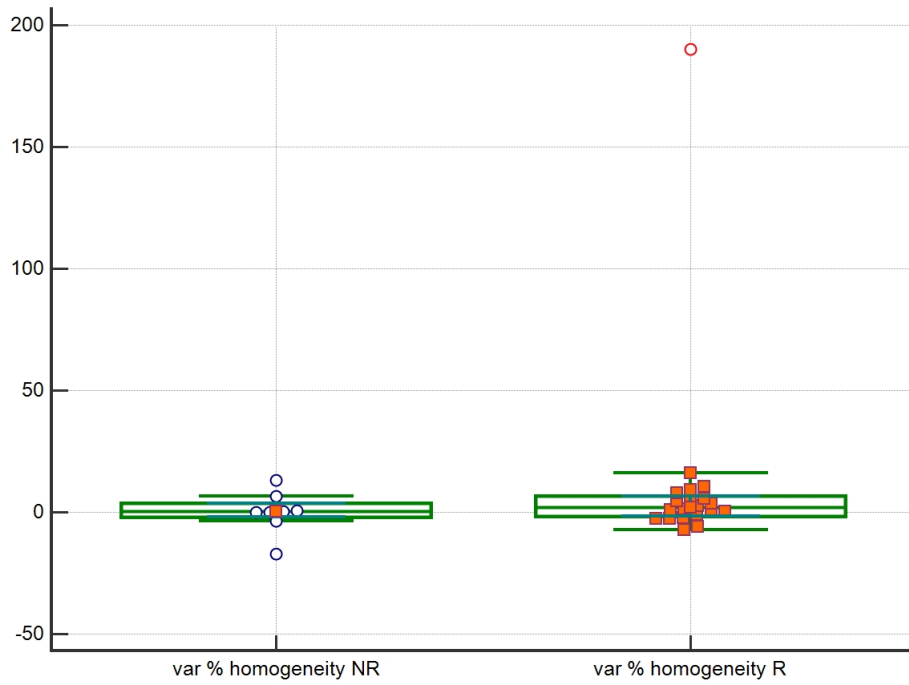


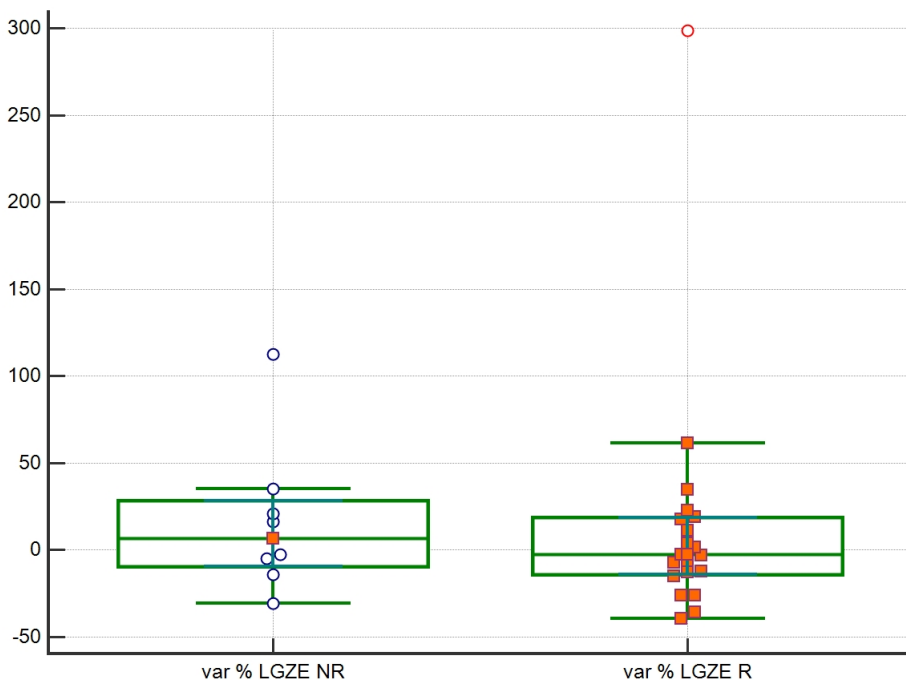
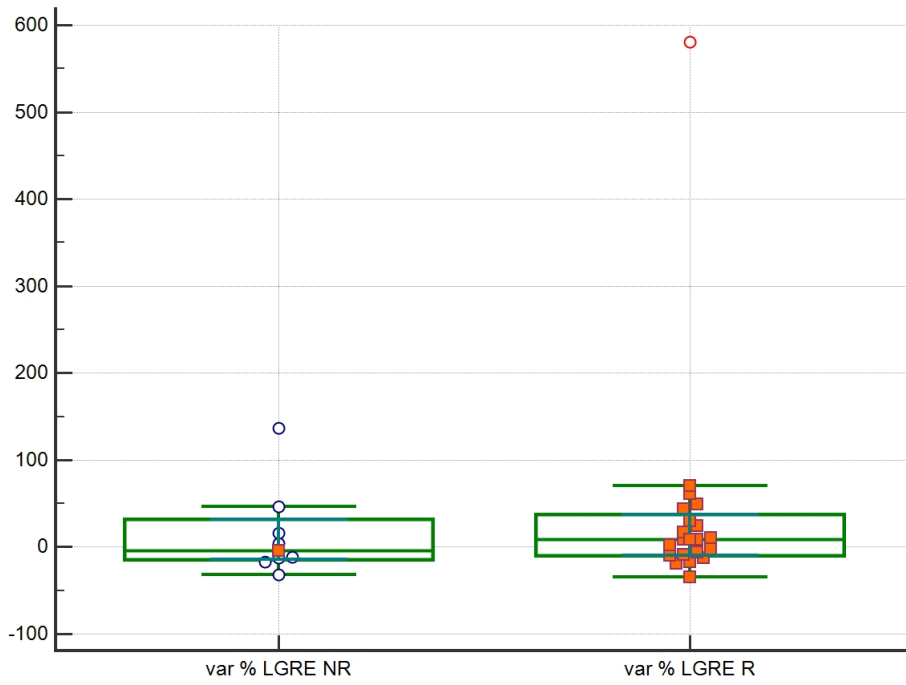


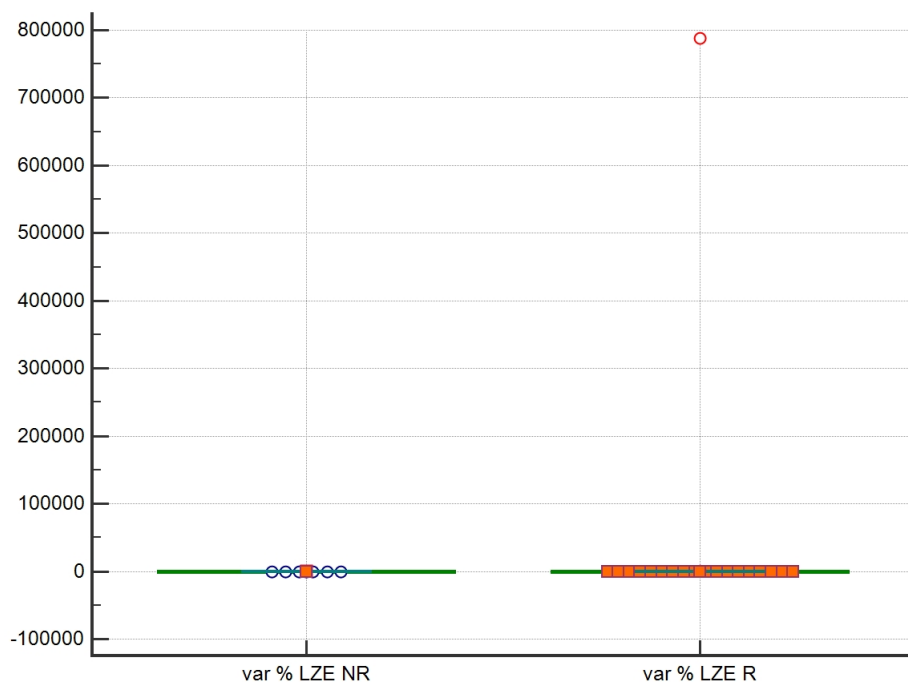
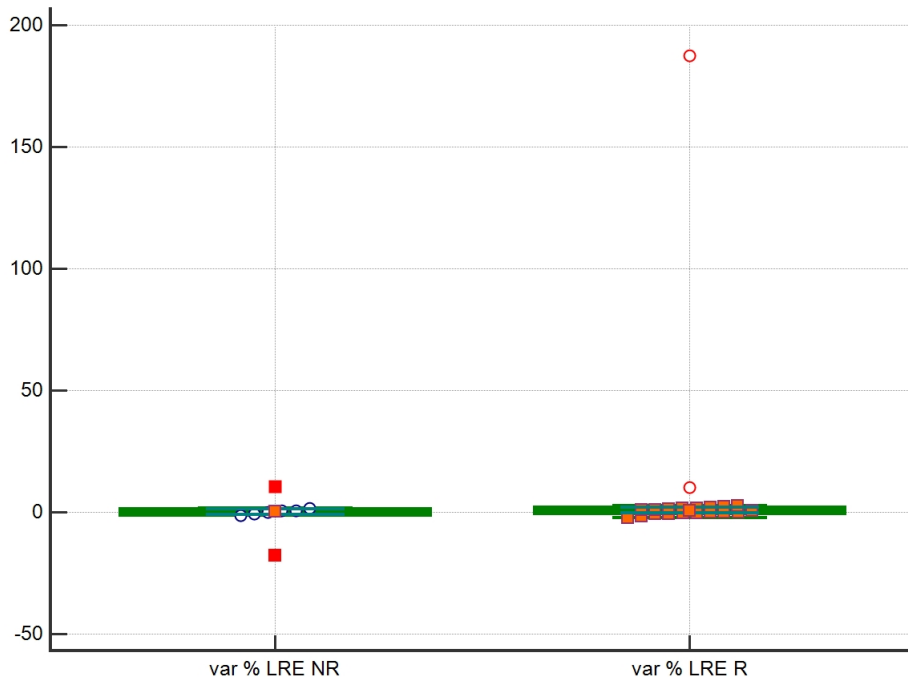


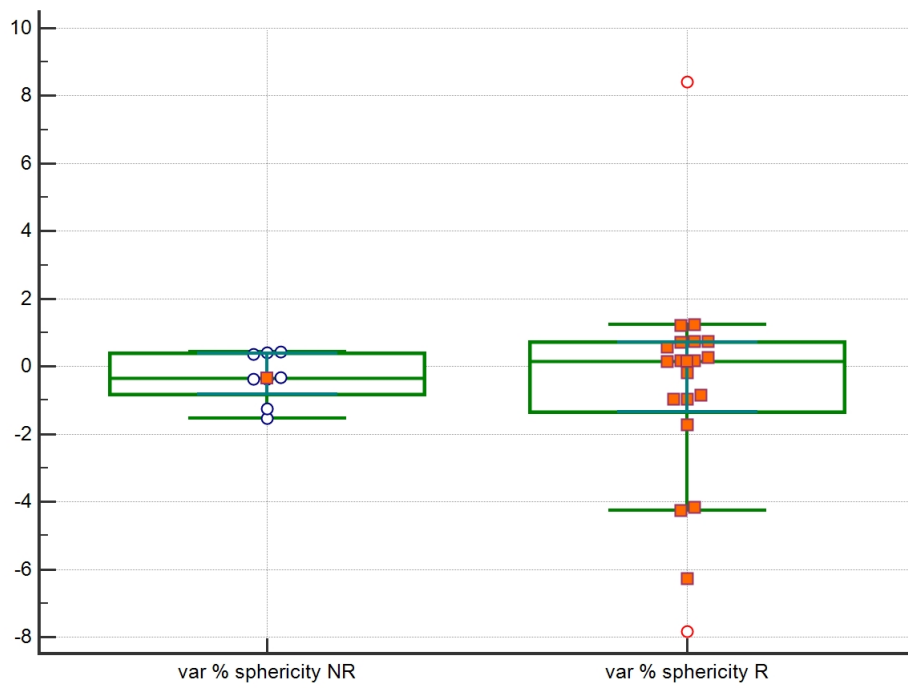
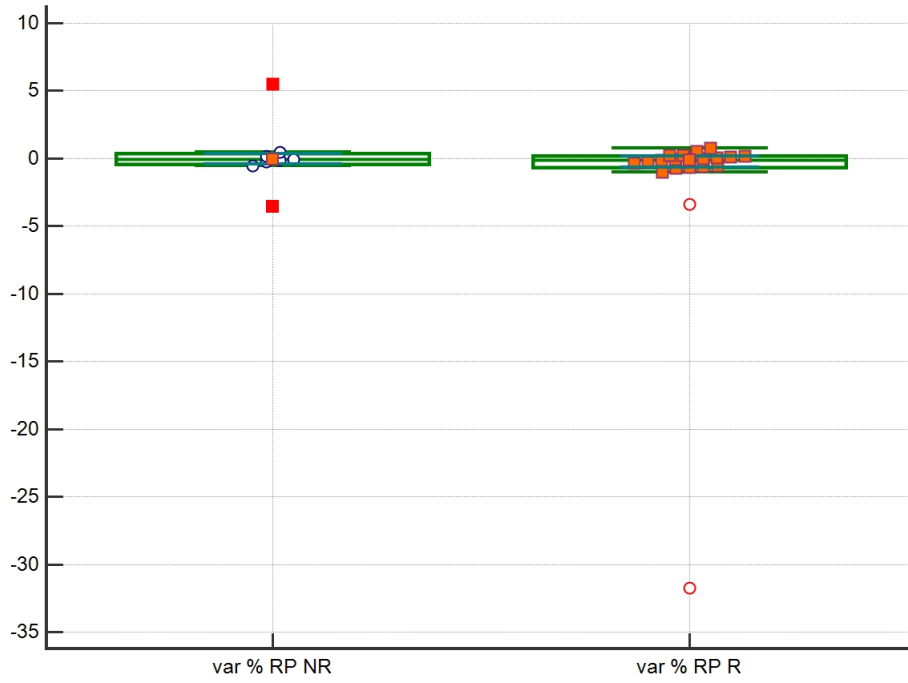


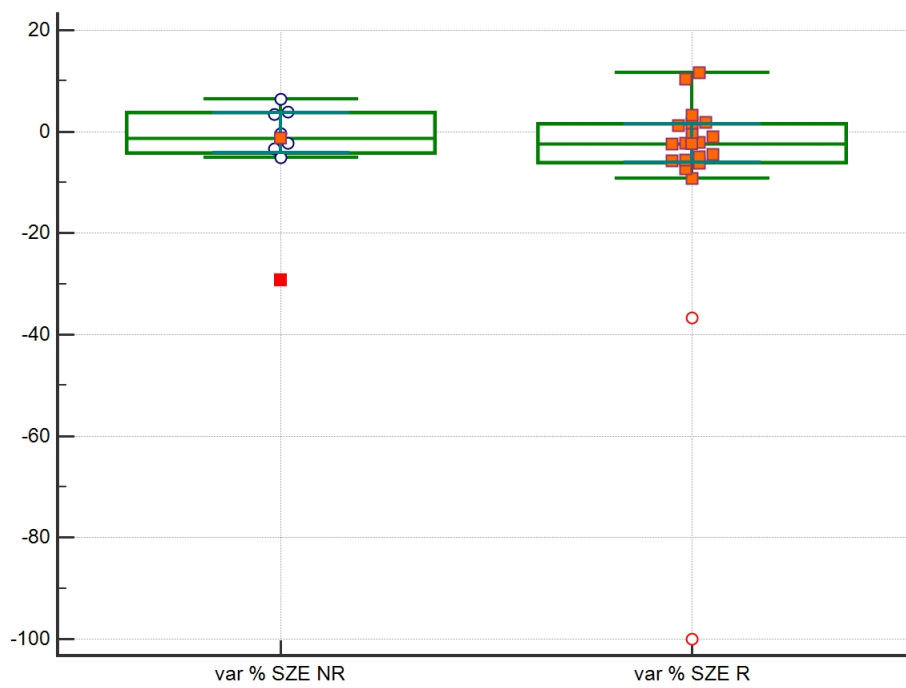
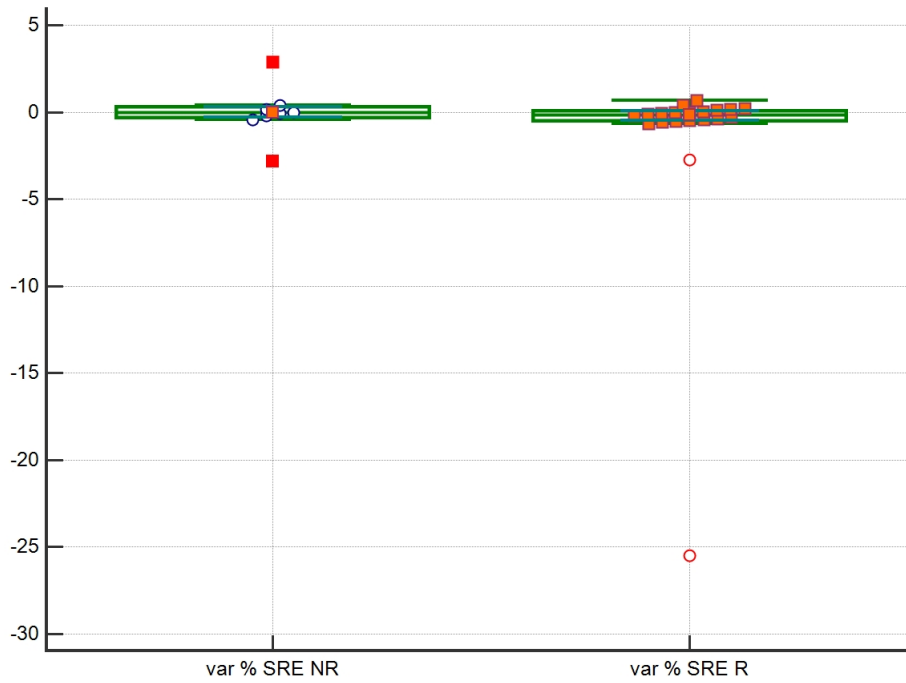


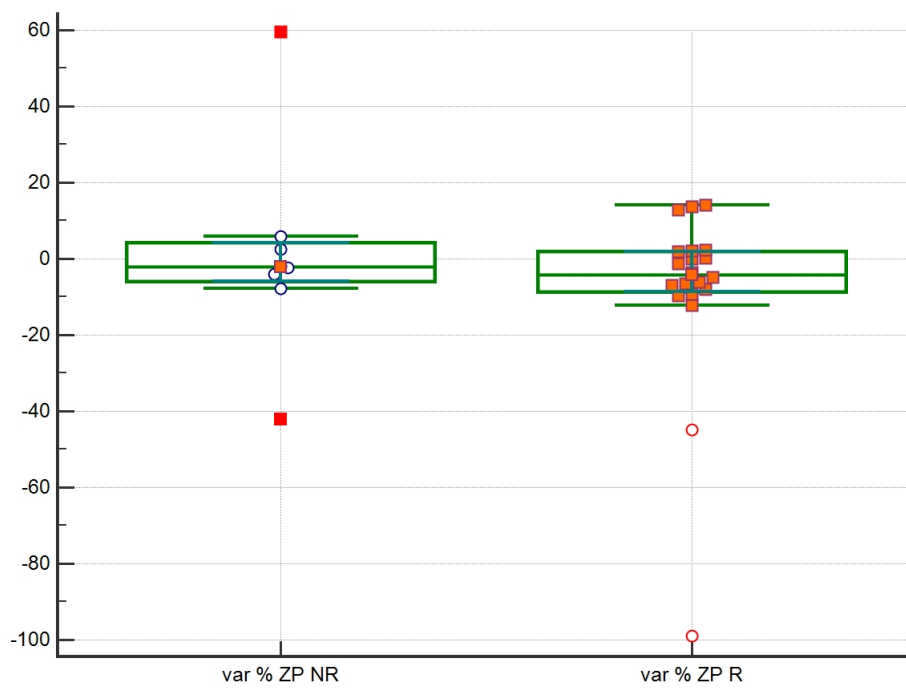












Bibliography

- [1] Hugo JWL Aerts. The potential of radiomic-based phenotyping in precision medicine: a review. *JAMA oncology*, 2(12):1636–1642, 2016.
- [2] Byeong-Cheol Ahn. Personalized medicine based on theranostic radioiodine molecular imaging for differentiated thyroid cancer. *BioMed research international*, 2016, 2016.
- [3] Dale L Bailey and JL Humm. *Nuclear medicine physics: a handbook for teachers and students*. IAEA, 2014.
- [4] RS Benua, NR Cicale, M Sonenberg, and RW Rawson. The relation of radioiodine dosimetry to results and complications in the treatment of metastatic thyroid cancer. *The American journal of roentgenology, radium therapy, and nuclear medicine*, 87:171–182, 1962.
- [5] L Bianchi, A Baroli, G Lomuscio, L Pedrazzini, A Pepe, L Pozzi, and C Chiesa. Dosimetry in the therapy of metastatic differentiated thyroid cancer administering high ¹³¹I activity: the experience of busto arszio hospital (italy). *The quarterly journal of nuclear medicine and molecular imaging: official publication of the Italian Association of Nuclear Medicine (AIMN)[and] the International Association of Radiopharmacology (IAR),[and] Section of the Society of..*, 56(6):515–521, 2012.
- [6] F Bonichon, X Buy, Y Godbert, V Pointillart, B Henriques de Figueiredo, A Gangi, and J Palussiere. Local treatment of metastases from differentiated thyroid cancer. In *Annales d'endocrinologie*, volume 76, pages 1S40–1S46. Elsevier, 2015.
- [7] B Brans, L Bodei, F Giammarile, Ola Lindén, M Luster, WJG Oyen, and Jan Tennvall. Clinical radionuclide therapy dosimetry: the quest for the “holy gray”. *European journal of nuclear medicine and molecular imaging*, 34(5):772–786, 2007.
- [8] Aaron P Brown, Jergin Chen, Ying J Hitchcock, Aniko Szabo, Dennis C Shrieve, and Jonathan D Tward. The risk of second primary malignancies up to three decades after

- the treatment of differentiated thyroid cancer. *The Journal of Clinical Endocrinology & Metabolism*, 93(2):504–515, 2008.
- [9] Ralph A Bundschuh, Julia Dinges, Larissa Neumann, Martin Seyfried, Norbert Zsótér, Laszló Papp, Robert Rosenberg, Karen Becker, Sabrina T Astner, Martin Henninger, et al. Textural parameters of tumor heterogeneity in 18f-fdg pet/ct for therapy response assessment and prognosis in patients with locally advanced rectal cancer. *Journal of Nuclear Medicine*, 55(6):891–897, 2014.
- [10] G Castellano, L Bonilha, LM Li, and F Cendes. Texture analysis of medical images. *Clinical radiology*, 59(12):1061–1069, 2004.
- [11] Sugama Chicklore, Vicky Goh, Musib Siddique, Arunabha Roy, Paul K Marsden, and Gary JR Cook. Quantifying tumour heterogeneity in 18 f-fdg pet/ct imaging by texture analysis. *European journal of nuclear medicine and molecular imaging*, 40(1):133–140, 2013.
- [12] C Chiesa, MR Castellani, C Vellani, E Orunesu, A Negri, R Azzeroni, F Botta, M Maccauro, G Aliberti, E Seregini, et al. Individualized dosimetry in the management of metastatic differentiated thyroid cancer. *The Quarterly Journal of Nuclear Medicine and Molecular Imaging*, 53(5):546, 2009.
- [13] Jack L Coffey, Mark Cristy, and Gordon G Warner. Specific absorbed fractions for photon sources uniformly distributed in the heart chambers and heart wall of a heterogeneous phantom. *Journal of Nuclear Medicine*, 22(1):65–71, 1981.
- [14] Gary JR Cook, Connie Yip, Muhammad Siddique, Vicky Goh, Sugama Chicklore, Arunabha Roy, Paul Marsden, Shahreen Ahmad, and David Landau. Are pretreatment 18f-fdg pet tumor textural features in non–small cell lung cancer associated with response and survival after chemoradiotherapy? *Journal of nuclear medicine*, 54(1):19–26, 2013.
- [15] David S Cooper, Gerard M Doherty, Bryan R Haugen, Richard T Kloos, Stephanie L Lee, Susan J Mandel, Ernest L Mazzaferri, Bryan McIver, Furio Pacini, Martin Schlumberger, et al. Revised american thyroid association management guidelines for patients with thyroid nodules and differentiated thyroid cancer: the american thyroid association (ata) guidelines taskforce on thyroid nodules and differentiated thyroid cancer. *Thyroid*, 19(11):1167–1214, 2009.
- [16] Fergus Davnall, Connie SP Yip, Gunnar Ljungqvist, Mariyah Selmi, Francesca Ng, Bal Sanghera, Balaji Ganeshan, Kenneth A Miles, Gary J Cook, and Vicky Goh.

Assessment of tumor heterogeneity: an emerging imaging tool for clinical practice? *Insights into imaging*, 3(6):573–589, 2012.

- [17] Désirée Deandreis, Carole Rubino, Hernan Tala, Sophie Leboulleux, Marie Terroir, Eric Baudin, Steve Larson, James A Fagin, Martin Schlumberger, and R Michael Tuttle. Comparison of empiric versus whole-body/-blood clearance dosimetry-based approach to radioactive iodine treatment in patients with metastases from differentiated thyroid cancer. *J Nucl Med*, 58(5):717–22, 2017.
- [18] Yuni K Dewaraja, Eric C Frey, George Sgouros, A Bertrand Brill, Peter Roberson, Pat B Zanzonico, and Michael Ljungberg. Mird pamphlet no. 23: quantitative spect for patient-specific 3-dimensional dosimetry in internal radionuclide therapy. *Journal of nuclear medicine: official publication, Society of Nuclear Medicine*, 53(8):1310, 2012.
- [19] Robert Dorn, Juergen Kopp, Harry Vogt, Peter Heidenreich, et al. Dosimetry-guided radioactive iodine treatment in patients with metastatic differentiated thyroid cancer: largest safe dose using a risk-adapted approach. *The Journal of Nuclear Medicine*, 44(3):451, 2003.
- [20] Janet F Eary, Finbarr O’Sullivan, Janet O’Sullivan, and Ernest U Conrad. Spatial heterogeneity in sarcoma 18f-fdg uptake as a predictor of patient outcome. *Journal of Nuclear Medicine*, 49(12):1973–1979, 2008.
- [21] I. Buvat F. Orlhac, C. Nioche. *Texture - User Guide, Local Image Features Extraction - LifeX*. F. Orlhac, C. Nioche, I. Buvat, 2018.
- [22] MA Flower, T Schlesinger, PJ Hinton, I Adam, AM Masoomi, MA Elbelli, RJ Ott, VR McCready, and CL Harmer. Radiation dose assessment in radioiodine therapy. 2. practical implementation using quantitative scanning and pet, with initial results on thyroid carcinoma. *Radiotherapy and Oncology*, 15(4):345–357, 1989.
- [23] Eleonore Fröhlich and Richard Wahl. The current role of targeted therapies to induce radioiodine uptake in thyroid cancer. *Cancer treatment reviews*, 40(5):665–674, 2014.
- [24] Joseph Galante, Matthew J Martin, Carlos Rodriguez, Wade Gordon, Emilio Bombardieri, Ettore Seregni, Laura Evangelista, Carlo Chiesa, and Arturo Chiti. Clinical applications of nuclear medicine targeted therapy.
- [25] Robert J Gillies, Paul E Kinahan, and Hedvig Hricak. Radiomics: images are more than pictures, they are data. *Radiology*, 278(2):563–577, 2015.

- [26] Vicky Goh, Balaji Ganeshan, Paul Nathan, Jaspal K Juttla, Anup Vinayan, and Kenneth A Miles. Assessment of response to tyrosine kinase inhibitors in metastatic renal cell cancer: Ct texture as a predictive biomarker. *Radiology*, 261(1):165–171, 2011.
- [27] Robert M Haralick, Karthikeyan Shanmugam, et al. Textural features for image classification. *IEEE Transactions on systems, man, and cybernetics*, (6):610–621, 1973.
- [28] Mathieu Hatt, Mohamed Majdoub, Martin Vallières, Florent Tixier, Catherine Cheze Le Rest, David Groheux, Elif Hindié, Antoine Martineau, Olivier Pradier, Roland Hustinx, et al. 18f-fdg pet uptake characterization through texture analysis: investigating the complementary nature of heterogeneity and functional tumor volume in a multi-cancer site patient cohort. *Journal of nuclear medicine*, 56(1):38–44, 2015.
- [29] Mathieu Hatt, Florent Tixier, Larry Pierce, Paul E Kinahan, Catherine Cheze Le Rest, and Dimitris Visvikis. Characterization of pet/ct images using texture analysis: the past, the present... any future? *European journal of nuclear medicine and molecular imaging*, 44(1):151–165, 2017.
- [30] Bryan R Haugen, Anna M Sawka, Erik K Alexander, Keith C Bible, Patrizio Caturegli, Gerard M Doherty, Susan J Mandel, John C Morris, Aziza Nassar, Furio Pacini, et al. American thyroid association guidelines on the management of thyroid nodules and differentiated thyroid cancer task force review and recommendation on the proposed renaming of encapsulated follicular variant papillary thyroid carcinoma without invasion to noninvasive follicular thyroid neoplasm with papillary-like nuclear features. *Thyroid*, 27(4):481–483, 2017.
- [31] Yuchen Jin, Douglas Van Nostrand, Lingxiao Cheng, Min Liu, and Libo Chen. Radioiodine refractory differentiated thyroid cancer. *Critical reviews in oncology/hematology*, 2018.
- [32] Joanna Klubo-Gwiezdzinska, Douglas Van Nostrand, Frank Atkins, Kenneth Burman, Jacqueline Jonklaas, Mihriye Mete, and Leonard Wartofsky. Efficacy of dosimetric versus empiric prescribed activity of 131i for therapy of differentiated thyroid cancer. *The Journal of Clinical Endocrinology & Metabolism*, 96(10):3217–3225, 2011.
- [33] Philippe Lambin, Emmanuel Rios-Velazquez, Ralph Leijenaar, Sara Carvalho, Ruud GPM van Stiphout, Patrick Granton, Catharina ML Zegers, Robert Gillies, Ronald Boellard, André Dekker, et al. Radiomics: extracting more information

- from medical images using advanced feature analysis. *European journal of cancer*, 48(4):441–446, 2012.
- [34] Michael Lassmann, Christoph Reiners, and Markus Luster. Dosimetry and thyroid cancer: the individual dosage of radioiodine. *Endocrine-related cancer*, 17(3):R161–R172, 2010.
- [35] Ralph TH Leijenaar, Georgi Nalbantov, Sara Carvalho, Wouter Jc Van Elmpt, Esther GC Troost, Ronald Boellaard, Hugo JWL Aerts, Robert J Gillies, and Philippe Lambin. The effect of suv discretization in quantitative fdg-pet radiomics: the need for standardized methodology in tumor texture analysis. *Scientific reports*, 5:11075, 2015.
- [36] Francisco DC Guerra Liberal, Adriana Alexandre S Tavares, and Joao Manuel RS Tavares. Palliative treatment of metastatic bone pain with radiopharmaceuticals: A perspective beyond strontium-89 and samarium-153. *Applied Radiation and Isotopes*, 110:87–99, 2016.
- [37] Hyeyeun Lim, Susan S Devesa, Julie A Sosa, David Check, and Cari M Kitahara. Trends in thyroid cancer incidence and mortality in the united states, 1974-2013. *Jama*, 317(13):1338–1348, 2017.
- [38] R Lopes, A Ayache, N Makni, P Puech, A Villers, S Mordon, and N Betrouni. Prostate cancer characterization on mr images using fractal features. *Medical physics*, 38(1):83–95, 2011.
- [39] Markus Luster, SE Clarke, M Dietlein, M Lassmann, P Lind, WJG Oyen, Jan Tennvall, and E Bombardieri. Guidelines for radioiodine therapy of differentiated thyroid cancer. *European journal of nuclear medicine and molecular imaging*, 35(10):1941, 2008.
- [40] Arndt Meier, Catherine Farrow, Benjamin E Harris, Gregory G King, and Allan Jones. Application of texture analysis to ventilation spect/ct data. *Computerized Medical Imaging and Graphics*, 35(6):438–450, 2011.
- [41] James Nagarajah, Marcel Janssen, Philipp Hetkamp, and Walter Jentzen. Iodine symporter targeting with ¹²⁴i/¹³¹i theranostics. *Journal of Nuclear Medicine*, 58(Supplement 2):34S–38S, 2017.
- [42] JPB O’connor, CJ Rose, A Jackson, Y Watson, S Cheung, F Maders, BJ Whitcher, C Roberts, GA Buonaccorsi, G Thompson, et al. Dce-mri biomarkers of tumour heterogeneity predict crc liver metastasis shrinkage following bevacizumab and folfox-6. *British journal of cancer*, 105(1):139, 2011.

- [43] Fanny Orlhac, Christophe Nioche, Michaël Soussan, and Irène Buvat. Understanding changes in tumor textural indices in pet: a comparison between visual assessment and index values in simulated and patient data. *J Nucl Med*, 58(3):387–392, 2017.
- [44] Fanny Orlhac, Michaël Soussan, Jacques-Antoine Maisonobe, Camilo A Garcia, Bruno Vanderlinden, and Irène Buvat. Tumor texture analysis in 18f-fdg pet: relationships between texture parameters, histogram indices, standardized uptake values, metabolic volumes, and total lesion glycolysis. *J Nucl Med*, 55(3):414–22, 2014.
- [45] Bosoon Park, Kurt C Lawrence, William R Windham, Yud-Ren Chen, and Kevin Chao. Discriminant analysis of dual-wavelength spectral images for classifying poultry carcasses. *Computers and Electronics in Agriculture*, 33(3):219–231, 2002.
- [46] Philipp Ritt, Hans Vija, Joachim Hornegger, and Torsten Kuwert. Absolute quantification in spect. *European journal of nuclear medicine and molecular imaging*, 38(1):69–77, 2011.
- [47] C Rubino, F De Vathaire, ME Dottorini, P Hall, C Schwartz, JE Couette, Marie-Gabrielle Dondon, MT Abbas, C Langlois, and M Schlumberger. Second primary malignancies in thyroid cancer patients. *British journal of cancer*, 89(9):1638, 2003.
- [48] Marcus Ruhlmann, Walter Jentzen, Verena Ruhlmann, Cinzia Pettinato, Gloria Rossi, Ina Binse, Andreas Bockisch, and Sandra Rosenbaum-Krumme. High level of agreement between pretherapeutic 124i pet and intratherapeutic 131i imaging in detecting iodine-positive thyroid cancer metastases. *Journal of Nuclear Medicine*, 57(9):1339–1342, 2016.
- [49] Paolo Russo, Michele Larobina, Francesca Di Lillo, Silvana Del Vecchio, and Giovanni Mettivier. Combined spect/ct and pet/ct for breast imaging. *Nuclear Instruments and Methods in Physics Research Section A: Accelerators, Spectrometers, Detectors and Associated Equipment*, 809:58–66, 2016.
- [50] Massimo Salvatori and Markus Luster. Radioiodine therapy dosimetry in benign thyroid disease and differentiated thyroid carcinoma. *European journal of nuclear medicine and molecular imaging*, 37(4):821–828, 2010.
- [51] Martin Schlumberger, Marcia Brose, Rosella Elisei, Sophie Leboulleux, Markus Luster, Fabian Pitoia, and Furio Pacini. Definition and management of radioactive iodine-refractory differentiated thyroid cancer. *The lancet Diabetes & endocrinology*, 2(5):356–358, 2014.

- [52] Christine Spitzweg, Keith C Bible, Lorenz C Hofbauer, and John C Morris. Advanced radioiodine-refractory differentiated thyroid cancer: the sodium iodide symporter and other emerging therapeutic targets. *The lancet Diabetes & endocrinology*, 2(10):830–842, 2014.
- [53] Michael G Stabin, Richard B Sparks, and Eric Crowe. Olinda/exm: the second-generation personal computer software for internal dose assessment in nuclear medicine. *The Journal of Nuclear Medicine*, 46(6):1023, 2005.
- [54] Guillaume Thibault, Bernard Fertil, Claire Navarro, Sandrine Pereira, Pierre Cau, Nicolas Levy, Jean Sequeira, and Jean-Luc Mari. Shape and texture indexes application to cell nuclei classification. *International Journal of Pattern Recognition and Artificial Intelligence*, 27(01):1357002, 2013.
- [55] Florent Tixier, Catherine Cheze Le Rest, Mathieu Hatt, Nidal M Albarghach, Olivier Pradier, Jean-Philippe Metges, Laurent Corcos, and Dimitris Visvikis. Intratumor heterogeneity characterized by textural features on baseline 18f-fdg pet images predicts response to concomitant radiochemotherapy in esophageal cancer. *Journal of Nuclear Medicine*, 52(3):369, 2011.
- [56] Mihran Tuceryan and Anil K Jain. Texture analysis. In *Handbook of pattern recognition and computer vision*, pages 235–276. World Scientific, 1993.
- [57] R Michael Tuttle, Rebecca Leboeuf, Richard J Robbins, Rebecca Qualey, Keith Pentlow, Steven M Larson, and Chee Y Chan. Empiric radioactive iodine dosing regimens frequently exceed maximum tolerated activity levels in elderly patients with thyroid cancer. *Journal of Nuclear Medicine*, 47(10):1587–1591, 2006.
- [58] Douglas Van Nostrand, Frank Atkins, Fred Yeganeh, Elmo Acio, Randy Bursaw, and Leonard Wartofsky. Dosimetrically determined doses of radioiodine for the treatment of metastatic thyroid carcinoma. *Thyroid*, 12(2):121–134, 2002.
- [59] Ansam Shaheen Wal’a Al-jubeh and Othman Zalloum. Radioiodine i-131 for diagnosing and treatment of thyroid diseases.
- [60] Roel Wierds, Boudewijn Brans, Bas Havekes, Gerrit J Kemerink, Servais G Halders, Nicolaas N Schaper, Walter H Backes, Felix M Mottaghy, and Walter Jentzen. Dose–response relationship in differentiated thyroid cancer patients undergoing radioiodine treatment assessed by means of 124i pet/ct. *Journal of Nuclear Medicine*, 57(7):1027–1032, 2016.

- [61] Stephen SF Yip and Hugo JWL Aerts. Applications and limitations of radiomics. *Physics in Medicine & Biology*, 61(13):R150, 2016.
- [62] Huan Yu, Curtis Caldwell, Katherine Mah, and Daniel Mozeg. Coregistered fdg pet/ct-based textural characterization of head and neck cancer for radiation treatment planning. *IEEE transactions on medical imaging*, 28(3):374–383, 2009.
- [63] Mark H Zweig and Gregory Campbell. Receiver-operating characteristic (roc) plots: a fundamental evaluation tool in clinical medicine. *Clinical chemistry*, 39(4):561–577, 1993.

Acknowledgements

Con questo lavoro si conclude il capitolo più importante del mio percorso non solo formativo, ma anche di crescita personale. Anche se sono io che oggi taglio il traguardo, sono state molte le persone che nel loro piccolo hanno contribuito affinché ciò si realizzasse e per questo le ringrazio.

In primo luogo ci tengo a ringraziare il mio relatore, il Prof. Andrea Lavagno, per la Sua disponibilità e per la preziosa opportunità che mi ha offerto con questa proposta di Tesi.

Un *Grazie* speciale a tutto il meraviglioso team della Fisica Sanitaria dell'Ospedale Mauriaziano di Torino che mi ha accolto in quest'ultimo anno con immensa simpatia facendomi sentire a casa. In primis *Grazie* al Direttore Michele Stasi per avermi dato la possibilità di mettermi in gioco in un contesto così distante dal mio ambiente universitario. Ma fin qui avreste letto solo pagine bianche se non fosse stato *Grazie* a Elisa, la cui esperienza e professionalità mi hanno fatto appassionare di questo mondo che fino all'anno scorso mi era completamente sconosciuto, ma che ha rivoluzionato i miei obiettivi sul futuro, e *Grazie* a Matteo e Claudia, il cui contributo è stato fondamentale per la stesura di questo elaborato; *Grazie* alla loro immensa disponibilità e instancabile attenzione con cui mi hanno seguito durante quest'ultimo anno e in particolar modo in questi ultimi mesi. *Grazie* perché è stata l'esperienza più intensa di tutto il mio percorso accademico che oltre ad avermi permesso di approfondire e arricchire il mio bagaglio scientifico, mi ha fatto conoscere delle persone fantastiche. *Grazie* a Chiara, alla nostra amicizia nata condividendo la tua scrivania e proseguita condividendo ricette di dolci e *Grazie* a Giulia per avermi ascoltata e incoraggiata.

Ma torniamo da dove tutto è cominciato, *Grazie* ai Falabracchi, perché, nonostante le nostre strade si stiano separando, doodle a raffica per aggiornarci sulle nostre vite davanti a una pizza non mancano mai!

Grazie a Miriam, la mia insostituibile compagna nucleare, per aver condiviso insieme i momenti più bui e le ansie progettando oltre a impianti nucleari, accoglienti torterie che

un giorno boh chissà. . .

Grazie a Eleonora, per i consigli, la sua indispensabile presenza e vicinanza e a Edoardo e Giovanni per aver condiviso con me questa giornata. *Grazie* a Giamma, insostituibile compagno...fondamentalmente di mangiate...e risate! *Grazie* a Camilla, amica di sempre, per la reciproca condivisione dei momenti più importati delle nostre vite dal giorno in cui le nostre mamme rassegnate ai nostri pianti ci hanno fatto tenere per mano nell'androne dell'asilo.

Grazie alle mie Comari, in particolar modo Poppy e Stefi per aver sofferto un po' con me l'ansia del fatidico 'ultimo esame' e a 'Quelli del Sabato sera', in particolare Stefano, Albi e Erik, veterani del Poli per i loro incoraggiamenti.

Un *Grazie* speciale va a mia Nonna, fondamentale pilastro della mia vita, perché non ha mai smesso di sostenermi e credere in me, soprattutto nei momenti più difficili, perché ha fatto suoi i miei dispiaceri e condiviso con me tutti i successi; senza di lei non sarei riuscita ad affrontare questi anni con la stessa determinazione e serenità...e *Grazie* a tutti gli altri Nonni che dal cielo vegliano su di me.

Grazie a Pippo e Lina e ai 1700 km attraversati per condividere con me anche questo giorno.

Questo lavoro di Tesi a coronamento di questo importante percorso, è dedicato ai miei genitori. E' *Grazie* a loro se sono arrivata fin qui e se sono diventata la persona che sono. Grazie per avermi insegnato a perseverare con determinazione e costanza in ogni percorso che si decide di intraprendere, Grazie per la silenziosa e costante presenza, per sopportarmi e supportarmi sempre.

Grazie infine a Edoardo, il mio complice, per la sua inesauribile pazienza e il suo indispensabile supporto, per condividere con me ogni successo e per incoraggiarmi nei momenti più bui, tirando sempre fuori la parte migliore di me.

*Se insisti e resisti,
raggiungi e conquisti.
Trilussa*